NTNU

Norwegian University of
Science and Technology

Underwater Robotics

Fluid Parameter Identification for Modelling
of Underwater Snake Robots

Gard Farstad Elgenes
Henrik Kilvær

Master of Science in Cybernetics and Robotics
Submission date: May 2017
Supervisor: Kristin Ytterstad Pettersen, ITK
Co-supervisor: Eleni Kelasidi, ITK

Norwegian University of Science and Technology
Department of Engineering Cybernetics

NTNU
Norges teknisk-naturvitenskapelige universitet

Fakultet for informasjonsteknologi, matematikk og elektroteknikk
Institutt for teknisk kybernetikk

MSc thesis assignment

Name of the candidates: Henrik Kilvær and Gard Elgenes

Subject: Cybernetics and Robotics

Title: Underwater robotics – Fluid Parameter Identification for Modelling of Underwater Snake Robots

Underwater snake (eel-like) robots bring a promising prospective for improving the efficiency and manoeuvrability of modern day underwater vehicles. However, for swimming robots, the dynamic modelling of the contact forces is most complicated compared to the modelling of the overall rigid motion and the dynamics of multi-articulated body. Hence, the hydrodynamic modelling task presents a major challenge. The existing analytical models are based on a simplified propulsive model that only provides a rough prediction of the effects of hydrodynamics on swimming robots. So, in order to obtain an accurate prediction of the hydrodynamic forces acting on the joints of the underwater snake robots, it is necessary to obtain the fluid coefficients experimentally.

In particular, this MSc project will address the hydrodynamics modelling challenges of underwater snake robots using experimental setup for validating the fluid coefficients. This involves the modelling of the hydrodynamic effect of the fluid-body interaction, combined with the overall rigid body motion. Experimental validation of the fluid coefficients for an underwater snake robot consists a useful method of validating an analytical control-oriented model that is mostly adapted by the robotic community.The hydrodynamic related parameters (fluid coefficients for drag forces and added mass effects) should be identified for different modules of the snake based on CFD simulations and/or ideally experiments.

The goal of this project is to plan, and if possible, perform experiments and simulations to validate the analytical model derived for an underwater snake robot, which takes into account added mass effect and the drag effect, by identifying experimentally the fluid coefficients.

The following subtasks are proposed for this master project:

1. Perform a literature study on underwater swimming robots, focusing on underwater snake robots.
2. Get familiar with the robotic system and work closely with the workshop, planning an experimental setup for these specific tasks.
3. Perform simulations for different snake module configurations, in preparation of future experiments.
4. Capture the fluid forces and the fluid coefficients for the link modules of the robot from simulation data and if possible, experiments.

Delivery date: 05.06.2017

Co-supervisor: Post Doc Eleni Kelasidi NTNU ITK/VISTA

Trondheim, 09.01.2017

Kristin Ytterstad Pettersen

Professor, supervisor.

Preface

This thesis is the concluding part in our Master of Technology in Cybernetics and Robotics at the Norwegian University of Science and Technology (NTNU). The project was carried out during the spring of 2017 at the Department of Engineering Cybernetics at NTNU, Trondheim.

We would like to thank our supervisor Professor Kristin Ytterstad Pettersen, and our co-supervisor Post Doc Eleni Kelasidi for valuable and much appreciated help, feedback and support. Thank you for believing in our contributions in the field of underwater snake robotics. A person that deserves a large amount of appreciation is Glenn Angell at the mechanical workshop. The experimental approaches in this thesis would not be realizable without this hard-working man and his colleagues.

Special thanks to Ricky M. and Dr. André for moral support, and to our faithful coffee brewer for never failing to deliver hot and slightly burned coffee.

Last but not least, we would like to thank our families, especially our significant others, Helena and Solfrid, for all their love and support. And to each of them for giving us two beautiful daughters, Nora Olivia and Vilje, in the time past since this project was started!

Trondheim, May 2017

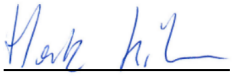

Henrik Kilvær

Gard Farstad Elgenes

Abstract

Unmanned underwater vehicles are being increasingly used for subsea maintenance, inspection and repair. Development of underwater snake robots show promising results towards extending the capabilities of traditional unmanned underwater vehicles. The slender and multi-articulated body of underwater snake robots allow for operation in tight spaces where other traditional underwater vehicles are incapable of operating.

The modelling and the control of underwater snake robots brings extra challenges compared to the traditional underwater vehicles, and thus it is important to develop accurate models to ensure desired behaviour and to precisely investigate the locomotion efficiency. A key component is the hydrodynamic modelling, taking into account complex and non-linear hydrodynamic effects. These hydrodynamic effects are difficult to model and are often based on analytical estimates.

This thesis seeks to determine the drag and added mass coefficients of a general planar model of underwater snake robots. The thesis presents methods for identifying fluid parameters based on CFD simulations and several experimental approaches. Additionally, this thesis investigates variations of the drag force modelling, providing more accurate representations of the hydrodynamic drag forces. The obtained fluid coefficients are compared to the existing estimates of fluid coefficients for a general model of underwater snake robots.

Sammendrag

Ubemannede undervannsfartøy blir i økende grad brukt til vedlikehold og reparasjonsarbeid på havbunnen. Utvikling av undervanns slangeroboter viser gode muligheter for utvidede arbeidsoppgaver og arbeidsområder sammenlignet med tradisjonelle ubemannede undervannsfartøy. Kombinasjonen av mange ledd og en slank kropp gjør det mulig for slangeroboter å arbeide i trange områder hvor mennesker og andre fartøy har vanskeligheter med å utføre arbeidsoppgaver.

Modellering og kontroll av undervanns slangeroboter er mer utfordrende sammenlignet med andre tradisjonelle undervannsfartøy. Nøyaktige modeller er derfor nødvendig for å oppnå ønsket oppførsel og for å undersøke effekten av forskjellige bevegelsesmønstre. En nøkkelegenskap er den hydrodynamiske modelleringen som tar hensyn til kompliserte og svært ulineære hydrodynamiske effekter. Disse effektene er vanskelige å modellere, og er ofte basert på analytiske estimat.

Formålet med denne masteroppgaven er å identifisere koeffisientene til vannmotstand (drag) og virtuell masse (added mass) for en generell modell for undervanns slangeroboter i planet. Masteroppgaven presenterer metoder for å identifisere fluidparameterne basert på CFD simuleringer og eksperimentelle tilnærminger. I tillegg undersøkes varianter av modellen for drag krefter, som kan gi en mer nøyaktig beskrivelse av de hydrodynamiske drag kreftene. De resulterende fluidkoeffisientene er sammenlignet med eksisterende estimater av fluidkoeffisienter for en generell modell av undervanns slangeroboter.

Contents

List of Figures

List of Tables

Nomenclature

$\mathbf{A}^D$	Dimensionless added mass matrix
$\mathbf{A}^{ND}$	Non-dimensionless added mass matrix
μ_n	Added mas parameter in y direction
μ_t	Added mas parameter in x direction
ϕ_i	Joint angle, i.e. angle between link i and link $i+1$
θ	Angle of attack, i.e. angle between snake module configuration and global x axis
θ_i	Link angle, i.e. angle between link i and global x axis
a	Major radius of link module
b	Minor radius of link module
$\hat{\mathbf{C}}_A$	Constant diagonal added mass matrix
$\hat{\mathbf{C}}_D$	Constant diagonal drag matrix
C_A	Added mass coefficient
C_d	Drag coefficient for link module in y direction
C_d^{I}, C_d^{II}	Linear and nonlinear drag coefficient in y direction
C_f	Drag coefficient for link module in x direction
C_f^{I}, C_f^{II}	Linear and nonlinear drag coefficient in x direction
$C_{A_{x,i}}$, $C_{A_{y,i}}$	Added mass coefficients in x and y direction for snake configuration i
$C_{d_{HL}}^{\mathrm{I}}$, $C_{d_{HL}}^{\mathrm{II}}$	Linear and nonlinear drag coefficient in y direction for head and tail
$C_{f_{HL}}^{\mathrm{I}}$, $C_{f_{HL}}^{\mathrm{II}}$	Linear and nonlinear drag coefficient in x direction for head and tail
C_{XY}^{I}, C_{XY}^{II}	Linear and nonlinear drag coefficient in x direction for cross flow
c_n	Drag parameter in y direction
c_t	Drag parameter in x direction
$\mathbf{f}_{D,HT}^{\mathrm{II}}$	Nonlinear drag force on the head and tail expressed in body frame

$\mathbf{f}^{\mathrm{I}}_{D,HT}$	Linear drag force on the head and tail expressed in body frame
$\mathbf{f}^{\mathrm{II}}_{D,L}$	Nonlinear drag force on a link expressed in body frame
$\mathbf{f}^{\mathrm{I}}_{D,L}$	Linear drag force on a link expressed in body frame
$\mathbf{f}^{\mathrm{II}}_{D,XY}$	Nonlinear drag force in x direction caused by flow in y direction, expressed in body frame
$\mathbf{f}^{\mathrm{I}}_{D,XY}$	Linear drag force in x direction caused by flow in y direction, expressed in body frame
f_A	Added mass force, expressed in body frame
f_B	Buoyancy force, expressed in body frame
f_D	Drag force, expressed in body frame
f_m	Measured force, expressed in body frame
F_x, F_y, F_z	Fluid forces in x, y and z direction expressed in body frame
f_{D_x}, f_{D_y}	Drag force in x and y directions, expressed in body frame
$\hat{f}_k$	Estimate of drag force model variation k, for $k = 1, \ldots, 6$
f_k	Drag force model variation k, for $k = 1, \ldots, 6$
l	Half length of a link module
n	Number of links in a snake module configuration
v_x, v_y, v_z	Fluid velocities in x, y and z direction expressed in body frame

List of Abbreviations

.gdf Geometric Data File.

.step Standard for the Exchange of Product Data.

AUV Autonomous Underwater Vehicle.

CAD Computer-Aided Design.

CB Centre of Buoyancy.

CD Computational Domain.

CFD Computational Fluid Dynamics.

CM Centre of Mass.

DAQ Data Acquisition.

DNV Det Norske Veritas.

DOF Degrees of Freedom.

fps Frames per Second.

HnLT Snake module configuration of robot with n links, together with head and tail modules..

HRM Hyper-Redundant Mechanism.

LDV Laser Doppler Velocimetry.

NURBS Non-Uniform Rational B-Splines.

ROV Remotely Operated Vehicles.

WADAM Wave Analysis by Diffraction and Morrison Theory.

WAMIT Wave Analysis Massachusetts Institute of Technology.

Chapter 1

Introduction

Development of underwater swimming robots are of interest, as they are more agile and can be more energy efficient than traditional remotely operated vehicles. However, the multi-articulated body of the robotic snake leads to complex dynamic models which has to take into account highly complex fluid dynamics.

The available models of underwater snake robots currently used in scientific communities, taking into account the hydrodynamic effects from both fluid drag and added mass effects, consider theoretical values for the fluid coefficients. This results in imprecise modelling of fluid effects rather than an ideal approximation of them. It is therefore necessary to obtain and calculate the fluid coefficients experimentally in order to obtain fairly accurate models of the fluid effects when modeling multi-articulated biologically inspired swimming snake robots, which is the topic of this thesis.

1.1 Scope of the Thesis

This thesis seeks to compare existing experimental methods and determining fluid coefficients for the underwater snake robot Mamba in order to obtain an accurate hydrodynamic model for underwater swimming snake robots. The fluid coefficients are determined initially based on extensive computational fluid dynamics (CFD) simulations, and then compared to experimentally obtained results. In particular, this thesis seeks to compare the results obtained from simulations and experiments to the currently used coefficients for Mamba. The underlying mathematical model of the swimming snake is restricted to a two-dimensional plane, thus the objective of the thesis is not to cover the three dimensional case.

1.2 Underwater Snake Robotics

Man has often looked to nature for inspiration when solving engineering problems. There are many different types of robots that imitates biological creatures, so-called biomimetic robots. Hyper-redundant mechanisms (HRMs) [49], better known as snake robots, are characterized firstly by being slender robots with a large body length to cross-sectional ratio. Secondly, they are highly flexible, meaning they are

able to swim by changing their multi-ariticulated body configuration. These two properties make them well-suited for a large variety of tasks [22]. The small cross-section and flexibility means they can fit into and operate in tight spaces, such as in or between pipes, where it is impossible for a human or other types of conventional underwater robotic solutions to operate.

Snake robots have been around for many years, but have mostly been land based. The first was made by Hirose [15]. The propulsion depends on the gait of the snake and friction between the skin and the contact surface. By replacing the land-based friction model with that of an underwater fluid friction variant, snake robots can be easily adapted to operate in water, or even as amphibious snake robots capable of movement both on land and in water [4]. Due to hydrodynamic complexity, there have been proposed fewer models for swimming robots than the land-based variants. But there has been an increase in biomimetic underwater snake robots in recent years [31], [41], [34], [26]

Remotely operated vehicles (ROVs) and other autonomous underwater vehicles (AUVs) are widely used for different subsea operations, as they can operate at larger depths and at more hazardous environments than humans. These systems have been increasingly used for tasks such as maintenance and inspection [12]. Bioinspired snake robots having flexible and slender bodies can further operate at tighter and more obstructed areas than other underwater vehicles. In addition to the agility and small cross-section of underwater snake robots, they are essentially mobile manipulator arms capable of doing a large variety of tasks. In addition, the snakes can be docked at underwater charging stations, resulting in a shorter response time when they are needed to perform a task. Development of snake robots are thus a very interesting area of development.

As mentioned earlier, the hydrodynamic modelling of swimming robotic snakes is more complex than for other underwater vehicles due to their multi-articulated body. Modelling of the fluid contact forces are especially more complicated compared to the dynamics of the overall rigid motion, making them more complex than ground-moving snakes. Hence, the main objective of this thesis is to provide useful inputs regarding the hydrodynamic model of underwater snake robots by experimentally obtaining the fluid coefficients.

1.2.1 Motion Patterns

The robotic snakes moves using a periodic gait pattern, mimicking the natural movement of a biological snake. Due to the different contact frictions on land and in water, the optimal gate pattern on land for a given snake robot, may not be the best suited for swimming robots. There are several swimming motions produced by underwater creatures, some of which are seen in Figure 1.1. The movements ranges from anguilliform- to thunniform swimming, where the first involves movement of almost the complete body length in a swimming pattern that produces thrust. Whereas thunniform swimmers such as the tuna has their motion restricted to the tail section of their body.

The two most common gait pattern for swimming snakes are lateral undulation (serpentine locomotion) and anguilliform swimming (eel-like motion). For lateral undulation, the movement of the head propagates down the body to the tail, re-

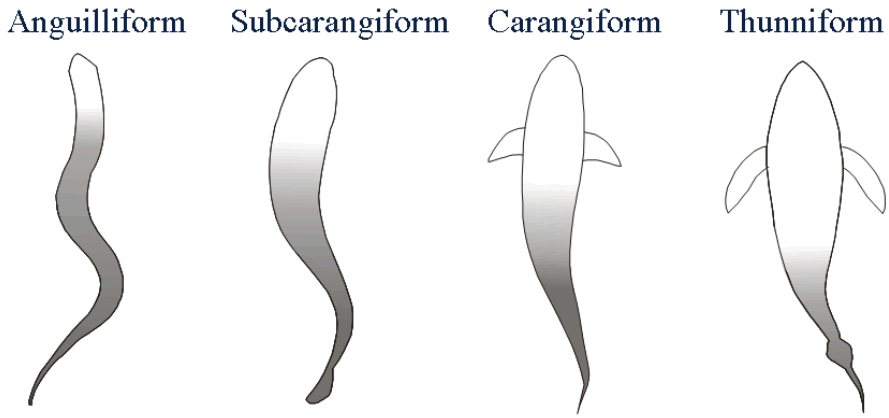

Figure 1.1: Different types of fish locomotion. Shaded areas indicates the parts of the body involved in thrust generation.

sembling a sinusoidal motion with constant amplitude [15]. Anguilliform swimming is an eel-like motion, where the head has less transverse oscillation and the waves increase in amplitude down the body.

1.2.2 Energy Efficiency

A key issue in development and control of underwater snake robots, is to achieve high motion-effectiveness and speed, while minimizing the consumed energy. This results in the snakes being able to undertake longer missions before the need to recharge.

The optimization of gait patterns is still to a large degree an unanswered question in the literature, although some results have been proposed. Optimization on both speed and efficiency are conflicting. Different swimming gaits have different results on the energy consumption and speed. One study has numerically solved the Navier-Stokes equations for simulations of the fluid flow past a anguilliform swimmer [25], for optimization on speed and energy efficiency. The study found differences in both speed and energy consumption, depending on the gait pattern. Lateral undulation was found to have higher efficiency and less velocity than *burst swimming*. Burst swimming resembles the motion of carangiform og thunniform swimming, with large amplitude of the tail motion. Similar results were also found by Wiens and Nahon [49]. The swimmer converges to a clearly anguilliform gait when optimal efficiency is considered, and tends towards carangiform gait for higher speed.

The power required for moving a fish-like body is significantly smaller for propulsion by swimming than what is required to drag the body at the same speed, [13]. It has also been shown that underwater swimming snake robots have a higher energy efficiency for all swimming gaites than the compared ROVs [21].

Existing results [19], [20], provides only qualitative comparisons of the gait

pattern efficiency, as theoretical values for the fluid coefficients are being used. Since fluid friction plays a significant role on the power consumption, a correct fluid model is desired. By identifying the fluid friction parameters, the energy efficiency of underwater snake robots like Mamba can be investigated and provide qualitative as well as quantitative comparison results regarding the power consumption.

1.2.3 Fluid Coefficients

As the energy efficient movement of an underwater robotic snake is closely coupled with the hydrodynamic effects of drag and added mass, there is a need for obtaining the fluid coefficients included in the model. Fluid torques have a direct impact on the power consumption of the system, and including these will improve the model from a hydrodynamic and energy efficiency point of view [18], [22]. Experimental validation of a complex model that takes into account both added-mass effects and drag forces while being expressed in closed form has not yet been investigated in the literature [22]. The existing models for underwater snake robots use theoretical values of the fluid coefficients which results in imprecise modelling. One modelling approach is based on Morison's equation, where each link is approximated as an elliptical cylinder. The authors in [22], encourage the need for further investigation into the method for fluid coefficient identification to obtain more precise values of the drag and added mass coefficients. They suggest installing force and torque sensors inside the modules to obtain more general results and therefore avoid the need for calculating these.

1.3 The Underwater Snake Robot Mamba

A recent underwater swimming robot developed at NTNU is Mamba [31],[32]. This robot is modular with common mechanical and electrical interfaces between the links, making it easy to expand. Different propulsion modules have been developed such as links with fins, passive or motorized wheels, thrusters, or legs, for different applications on land as well as in water. The model considered in this report does not include these propulsion modules. The thrust is produced by a gait pattern. Each link is 0.09 m long and has one degree of freedom (DOF) with a maximum joint travel of ± 90 degrees. The head module contains a micro controller, a wireless camera, LEDs and wireless communication. The tail module only contains an anchoring mechanism for the external power supply and pressurized air for inflating an applied skin.

NOTE: The robot configuration allows for motion in 3D with interconnected vertical and horizontal links. However, in this thesis, we disregard vertical motion, and consider only motion in 2D. And thus the length of each link is assumed to be 0.18 m. In the original terms, Figure 1.3 is made up of 12 links (excluding the head and tail modules), whereas it would be counted as six link modules in this thesis.

Mamba is able to move on both land and in water, see Figure 1.2 and Figure 1.3. The robot is modular with arbitrary interconnection of links, communication and power lines. The robustness and easy reconfiguration of the robot makes it a solid experimental platform for ongoing research on robotic snakes at NTNU. The robot

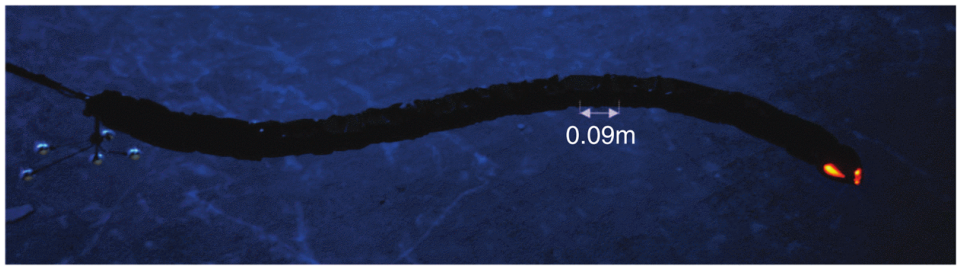

Figure 1.2: NTNU's underwater snake robot Mamba [32], during an experiment at Marine Cybernetic Laboratory at Tyholt.

Figure 1.3: Mamba [32] on land.

is waterproof down to around 5 m, and can also be covered with a skin, providing a smoother exterior surface. Extensive work has been done in the robotic snakes community at NTNU on path-following control [22] using the underwater snake robot Mamba. Mamba is the robot which will be used in this report to identify the fluid coefficients for the hydrodynamic model proposed in [18] for underwater snake robots.

1.4 Methods for Identification of Fluid Coefficients

There are several approaches for identifying fluid coefficients for submerged bodies, both by theoretical estimates and experimental procedures. This section presents some of the many possible methods.

1.4.1 Simulation Software

Drag Coefficients

Simulations for finding the fluid drag coefficients can be found using CFD. Multiple software solutions are available, some of which are ANSYS Fluent [1], OpenFOAM [40] and Solidworks Flow Simulation [45]. Solidworks is chosen as it is fairly straight forward to simulate on existing Computer-Aided Design (CAD) models of the snake modules. Solidworks is a commonly used 3D-CAD software with many capabilities and expansion packages. The Flow Simulation package is powerful, and high mesh settings may provide very accurate results. However, a very refined mesh results in the simulations being extremely computationally demanding. An adaptive meshing function enables the user to select a less refined mesh while automatically creating a finer mesh in important areas.

Added Mass

For obtaining the added mass coefficients, two software candidates have been considered, namely WAMIT (Wave Analysis by Massachusetts Institute of Technology) [48] and WADAM (Wave Analysis by Diffraction and Morison Theory) [7]. They are both using the panel method, which builds on the principle of solving the Green integral equation, dividing the structure into small panels (2D or 3D). Solving the green integral equation for each element gives values of velocity potential over each element. The dynamic pressure is easily found from this and the velocity over the surface is found applying the Bernoulli equation. From there, one finds the potential damping and added mass by integrating the velocity potential over the body, [9]. The panel method is further explained in Chapter 3.2.1 This method is quite accurate and computationally easy as the added mass coefficients are estimated without the use of CFD. WADAM and WAMIT is widely used to obtain the added mass coefficients in marine vehicles or floating structure [33], [29], [27].

WAMIT is considered the industry standard among oil and engineering companies [12], however, it lacks a graphical user interface. Hence, WADAM is considered in this thesis as the 3D potential theory in WADAM is directly based on WAMIT,

and it has a good graphical user interface. WADAM is available as part of the DNV GL software package SESAM [7].

Other approaches for identifying the added mass coefficients are Strip Theory and empirical 3D data. Strip theory evaluates a 3D object as a sum of 2D strips and assumes a slender body where the length is much larger than the width. This will not be the case for a snake robot with few links. Empirical 3D data uses already obtained experimental, analytical or empirical results on bodies such as a cylinder that can resemble the snake body. There have been many studies on cylindrical objects and references such as the Det Norske Veritas (DNV) standard [6], can be used. However, these are often general results which will not apply directly to the underwater swimming robotic snake Mamba.

1.4.2 Experiments for Identification

Different methods for experimentally determining the fluid coefficients are found in the literature. Below, some of the methods are overviewed.

- **Free decay pendulum motion**
  - The free decay pendulum test [10] uses a scaled-down model of the vehicle as a pendulum connected by a rod. It is set to oscillate in water when it is displaced from its equilibrium position, Figure 1.4(a). Due to the hydrodynamic forces that resist the motion, the amplitude of the swinging motion will decay over time. The hydrodynamic parameters can then be extracted from the history of the motion. This is based on the free decay test with spring oscillation [37]. There is a need of accurately measuring the position and the states of the vehicle, which can be challenging. Advantages of this experiment are that the motion of the pendulum is restricted in a single plane and has only one DOF. The position of the pendulum is fully described by the displacement angle, θ. The motion is constrained, and therefore the dynamic equations could represent the motion correctly. Secondly, the variable θ can be measured accurately, either by a camera as done in [10], or by position sensors.
- **Towing test and rotation test**
  - This approach is often used for ship design [16]. An object is towed at different velocities to determine quadratic and linear damping. One can interpolate to obtain quadratic and linear damping functions. In addition, accelerated runs are performed for different accelerations. By measuring forces at different velocities and subtracting the already known damping and rigid body mass forces, added mass forces can be obtained. The procedure can be repeated for rotational experiment. The approach is quite easy to do, but is time consuming.
- **Guided rail**
  - A guided rail experiment acts on the same principle as the towing test, but by instead using a guided rail in an enclosed tank. The module is connected to the rail and moves in the tank. By measuring the forces applied, one can extract the hydrodynamic parameters [39], [28]. See Figure 1.4(b).

- **On-board sensor experiment**
  - Acceleration can be measured for a given thrust input. Inertia and damping terms can be obtained by filtering acceleration data [9].
- **Planar motion mechanism tests**
  - A planar motion mechanism is an electromechanical device used to move a model ship in a pre-programmed series of motions in a test tank facility. The forces and moments on the model and other data relating to performance are measured [35].

Based on available resources and equipment, three experiments are performed. For identification of drag coefficients, two variations of the above concepts are considered. Firstly, a simplified guided rail approach is performed as a proof of concept, Chapter 4.3. The second experiment is based on the towing test and guided rail approaches, where the object is placed in a circulation tank and fluid flow is applied, Chapter 4.4. The experimental approach concerning added mass coefficients is inspired by the decaying pendulum. However, the pendulum oscillations is actuated by a servo motor, Chapter 4.4.

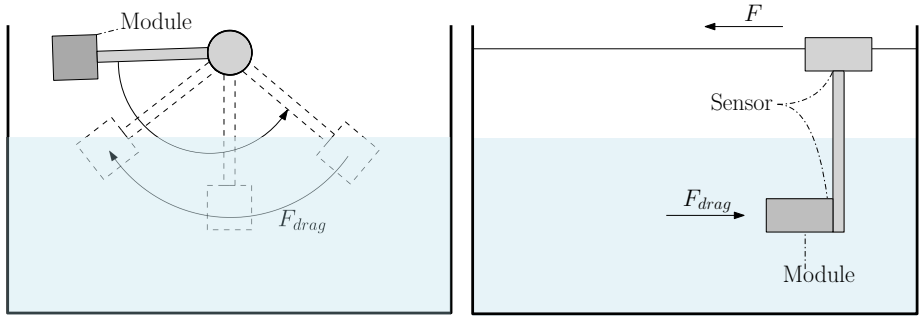

(a) Decaying pendulum (b) Guided rail

Figure 1.4: Experiments for determining hydrodynamic coefficients.

1.5 Outline of the Thesis

The thesis is organized as follows. In Chapter 1, a brief review is given of underwater snake robotics in general and NTNU's underwater snake robot, Mamba, in particular. Additionally, common methods for identifying fluid coefficients are presented. Chapter 2 presents a mathematical model of a general underwater robotic snake together with proposed variations of the drag force model. Next, in Chapter 3 simulation methods for identifying the fluid coefficients are presented, while Chapter 4 details the carried out experimental procedures. The results obtained from both simulations and experiments are presented and discussed in Chapter 5, before the conclusion of the findings together with proposals for future work are presented in Chapter 6.

Chapter 2

Modelling of Underwater Snake Robots

This chapter seeks to give a brief insight to the mathematical model of a general underwater robotic snake, which also can be used to describe the motion of the underwater robotic snake Mamba. In addition, variations to parts of the model considering the fluid coefficients is presented. The model variations considers including fluid forces for the head and tail modules, as the original model incorporates link modules only.

The complete model of the underwater robotic snake presented in Chapters 2.1 and 2.2, is derived in the article *Modeling and Propulsion Methods of Underwater Snake Robots* [23], and a summary is presented in this chapter. The authors presents a two-dimensional continuous model of the snake robot's kinematics and dynamics, as well as a straight-line-path-following controller for the snake. The model is based on previous work done by the same authors [18],

The snake is made up of n rigid links, each of length $2l$, mass m and moment of inertia $J = \frac{1}{3}ml^2$. The center of mass (CM) of each link is located in the center of that link. Figure 2.1 show the different frames and terms used in this section, where θ_i denotes the link angle of link $i \in 1, \ldots, n$, and $\phi_i = \theta_i - \theta_{i+1}$ is the joint angle of link $i \in 1, \ldots, n-1$. The reader is referred to [23] and [18] for a more thorough explanation of the mathematical terms and notation used. The resulting closed-form model is well suited for model-based control.

2.1 Equations of Motion

The equations of motion for the underwater snake robot can be expressed as stated in [22]. The acceleration of the CM is given by

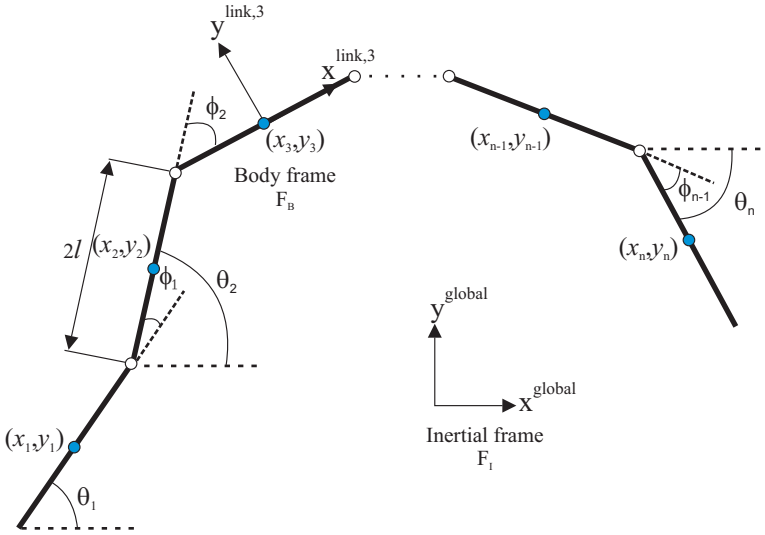

Figure 2.1: Kinematic parameters of underwater snake robot, [22].

$$\begin{bmatrix}\ddot{p}_x\\ \ddot{p}_y\end{bmatrix} = -\mathbf{M}_p\mathbf{N}_p\begin{bmatrix}\text{diag}(\dot{\theta}) & \mathbf{0}\\ \mathbf{0} & \text{diag}(\dot{\theta})\end{bmatrix}\mathbf{E}\begin{bmatrix}\dot{p}_x\\ \dot{p}_y\end{bmatrix}$$
$$-\mathbf{M}_p\mathbf{N}_p\begin{bmatrix}\text{diag}(\dot{\theta}) & \mathbf{0}\\ \mathbf{0} & \text{diag}(\dot{\theta})\end{bmatrix}\begin{bmatrix}\mathbf{K}^T\mathbf{S}_\theta\dot{\theta} - \mathbf{V}_x\\ -\mathbf{K}^T\mathbf{C}_\theta\dot{\theta} - \mathbf{V}_y\end{bmatrix} - \mathbf{M}_p\mathbf{L}_p\begin{bmatrix}\mathbf{K}^T(\mathbf{C}_\theta\dot{\boldsymbol{\theta}}^2 + \mathbf{S}_\theta\ddot{\boldsymbol{\theta}})\\ \mathbf{K}^T(\mathbf{S}_\theta\dot{\boldsymbol{\theta}}^2 - \mathbf{C}_\theta\ddot{\boldsymbol{\theta}})\end{bmatrix}$$
$$+\mathbf{M}_p\mathbf{E}^T\begin{bmatrix}\mathbf{f}_{Dx} + \mathbf{f}_{tx}\\ \mathbf{f}_{Dy} + \mathbf{f}_{ty}\end{bmatrix}, \quad (2.1)$$

where $\mathbf{M}_p$, $\mathbf{N}_p$, $\mathbf{E}$, $\mathbf{K}$, $\mathbf{E}$, $\mathbf{V}_x$ and $\mathbf{V}_y$ are given in [23]. Adding the influence of fluid forces and torques, the equations of motion for the robot is given by Equation 2.1 and

$$\mathbf{M}_\theta\ddot{\boldsymbol{\theta}} + \mathbf{W}_\theta\dot{\boldsymbol{\theta}}^2 + \mathbf{V}_{\theta,\dot{\theta}}\dot{\boldsymbol{\theta}} + \mathbf{N}_{\theta,\dot{\theta}}(\mathbf{e}\dot{p}_x - \mathbf{V_x}) + \mathbf{P}_{\theta,\dot{\theta}}(\mathbf{e}\dot{p}_y - \mathbf{V_y})$$
$$+\mathbf{K_x}(\mathbf{f_{Dx}} + \mathbf{f_{tx}}) + \mathbf{K_y}(\mathbf{f_{Dy}} + \mathbf{f_{ty}}) - \boldsymbol{\tau}_t = \mathbf{D}^T\mathbf{u}, \quad (2.2)$$

where the various matrices are given in [23]. The drag forces $\mathbf{f}_{Dx}$ in x direction and $\mathbf{f}_{Dy}$ in y direction are further discussed in the next section. By defining state variables $\mathbf{x} = \begin{bmatrix}\boldsymbol{\theta}^T & \mathbf{p}_{CM}^T & \dot{\boldsymbol{\theta}}^T & \dot{\mathbf{p}}_{CM}^T\end{bmatrix}$ the model is rewritten in compact state-space form as

$$\dot{\mathbf{x}} = \begin{bmatrix}\dot{\boldsymbol{\theta}}^T & \dot{\mathbf{p}}_{CM}^T & \ddot{\boldsymbol{\theta}}^T & \ddot{\mathbf{p}}_{CM}^T\end{bmatrix} = \mathbf{F}(\mathbf{x},\mathbf{u}), \quad (2.3)$$

where $\mathbf{F}(\mathbf{x},\mathbf{u})$ is found by solving 2.1 and 2.2 for $\ddot{\mathbf{p}}_{CM}$ and $\ddot{\boldsymbol{\theta}}$.

This model is also valid for ground-moving snakes, where the drag forces in x and y direction are replaced with a ground-friction model [31], and added mass effects are disregarded, making it a versatile model for use in both water and on land.

2.2 Hydrodynamic Modelling

The model presented in this thesis includes both linear and nonlinear drag effects, added mass effects, fluid moments and fluid currents. Fluid moments are omitted in most modeling approaches for underwater snake robots as they have little impact on the overall motion of the system. However, including these provides a more accurate model from an energy-efficiency standpoint. The hydrodynamic modelling is the most challenging part compared to the motion dynamics, and made assumptions depends highly on the body shape and properties of the fluid flow [49].

The impact of the fluid forces is dependent on the shape and movement of the submerged object. Generally, if the object moves or swims slowly, the viscous forces are dominant, but for larger objects, the added mass effects will dominate. An underwater robotic snake lies in between these two extrema and is thus effected by both drag forces (resistive forces) and added mass (reactive forces). For low Reynolds numbers, a resistance model like Taylor's model [47] is suitable. For high Reynolds number and slender bodies, Lighthills' model [30], is appropriate [50]. The non-linearity of the fluid forces acting on a submerged moving body are highly complex and an exact model is therefore not possible to obtain. Numerical solution of the Navier Stokes equations using CFD gives accurate fluid forces, but this is approach is not suitable for online control purposes.

The results obtained in [18] are found using the Morison's equations [36], [11]. The underwater snake robot is assumed a slender body made up of cylindrical links with elliptical cross sections, where each link of the snake is considered as isolated segments. The fluid forces are dependent only on the transverse link motion. This modelling approach has some underlying assumptions:

- **Assumption 1** The fluid is incompressible, viscid and incompressible in the inertia frame
- **Assumption 2** The robot is neutrally buoyant
- **Assumption 3** The current in the inertial frame, $v_c = [V_{x,i}, V_{y,i}]^T$ is constant and irrotational

The fluid forces are functions of the current and are expressed as a function of relative velocity. The relative velocity of link i is defined as

$$v_{r,i}^{link,i} = \dot{p}_i^{link,i} - v_{c,i}^{link,i}, \tag{2.4}$$

where $v_{c,i}^{link,i}$ is the current velocity expressed in body frame.

Due to assumption 3, $\dot{v}_c = 0$ and the time derivative of the velocity expressed in body frame (Figure 2.1) is

$$\dot{v}_{c,i}^{link,i} = \frac{d}{dt}\left((\mathbf{R}_{link,i}^{global})^T v_c\right) = \begin{bmatrix} -\sin\theta_i\dot{\theta}_i & \cos\theta_i\dot{\theta}_i \\ -\cos\theta_i\dot{\theta}_i & -\sin\theta_i\dot{\theta}_i \end{bmatrix} \begin{bmatrix} V_{x,i} \\ V_{y,i} \end{bmatrix}. \tag{2.5}$$

Each link is subject to a fluid force and torque acting on the link CM. The fluid force is made up of two components: drag force and added mass effects. The employed drag model takes into account the general case of anisotropic friction, which results in two drag terms, c_t in x direction (tangential to the link) and c_n in the y direction. The fluid forces acting on link i in the body frame can then be written as

$$f_i^{link,i} = -\hat{\mathbf{C}}_A \dot{v}_{r,i}^{link,i} - \hat{\mathbf{C}}_D v_{r,i}^{link,i} - \hat{\mathbf{C}}_D \operatorname{sgn}\left(v_{r,i}^{link,i}\right)\left(v_{r,i}^{link,i}\right)^2, \tag{2.6}$$

where $\hat{\mathbf{C}}_D$ and $\hat{\mathbf{C}}_A$ are the constant diagonal drag- and added mass parameter matrices containing the fluid coefficients to be identified. In addition, the following assumption is made in order to avoid numerically calculating the drag forces.

- **Assumption 4** The relative velocity at each section of the link in body frame is equal to the relative velocity of the respective CM of each link.

This assumption is valid because of the small link length compared to the total length of the snake. Further, with this assumption there is no need for deriving the drag forces in analytical form, due to the nonlinear terms. Thus, for a cylindrical link with length $2l$ and major and minor diameter $2a$ and $2b$, respectively, $\hat{\mathbf{C}}_D$ and $\hat{\mathbf{C}}_A$ can be expressed as

$$\hat{\mathbf{C}}_D = \begin{bmatrix} c_t & 0 \\ 0 & c_n \end{bmatrix} = \begin{bmatrix} \frac{1}{2}\rho\pi C_f \frac{(a+b)}{2} 2l & 0 \\ 0 & \frac{1}{2}\rho C_d 2a 2l \end{bmatrix}, \tag{2.7}$$

$$\hat{\mathbf{C}}_A = \begin{bmatrix} \mu_t & 0 \\ 0 & \mu_n \end{bmatrix} = \begin{bmatrix} 0 & 0 \\ 0 & \rho\pi C_A a^2 2l \end{bmatrix}, \tag{2.8}$$

where ρ is the density of the fluid, and C_f and C_d are the drag coefficients in x and y direction of motion, whereas C_A is the added mass coefficient. Note that the added mass parameter in x direction is set to zero, $\mu_t = 0$, as this is insignificant compared to the total body mass of this slender body.
The fluid torques are included in this model as they pose a significant contribution to the actuation torques at each link-joint. Thus they have a direct effect on the power consumption of the system. The fluid torque is caused by the link rotation only. Assuming each link of the robot is oscillating similarly to a flat plate oscillating in a rotational motion, the torque applied by the fluid on link i is modeled as

$$\tau_i = -\lambda_1 \ddot{\theta}_i - \lambda_2 \dot{\theta}_i - \lambda_3 \dot{\theta}_i |\dot{\theta}_i|, \tag{2.9}$$

where λ_1, λ_2 and λ_3 are dependent on the fluid characteristics and the shape of the links. The added mass torque for a cylinder can be written

$$\lambda_1 = \frac{1}{12}\rho\pi C_M (a^2 - b^2)^2 l^3, \tag{2.10}$$

where C_M is the added mass inertia constant, and λ_2 and λ_3 are found by integrating the drag torque around the link CM over the link length, giving

$$\tau_{drag} = -\int_{-l}^{l} \left(sC_{Ld_x} s\dot{\theta}_i ds + sC_{Ld_x} \operatorname{sgn}(s\dot{\theta}_i)(s\dot{\theta}_i)^2 \right) ds = -\lambda_2 \dot{\theta}_i - \lambda_3 \dot{\theta}_i |\dot{\theta}_i|, \tag{2.11}$$

where λ_2 and λ_3 are given by

$$\lambda_2 = \frac{1}{6}\rho\pi C_f(a+b)l^3, \tag{2.12}$$

$$\lambda_3 = \frac{1}{8}\rho\pi C_f(a+b)l^4. \tag{2.13}$$

The expression for the fluid forces on link i given in the inertial frame is expressed as

$$f_i^{global} = \mathbf{R}_{link,i}^{global} f_i^{link,i} = \begin{bmatrix} \cos\theta_i & -\sin\theta_i \\ \sin\theta_i & \cos\theta_i \end{bmatrix} \begin{bmatrix} f_{x,i}^{link,i} \\ f_{y,i}^{link,i} \end{bmatrix}. \tag{2.14}$$

Performing the matrix multiplications, the global frame fluid forces on the links can be written on vector form as

$$\mathbf{f} = \begin{bmatrix} \mathbf{f}_x \\ \mathbf{f}_y \end{bmatrix} = \begin{bmatrix} \mathbf{f}_{A_x} \\ \mathbf{f}_{A_y} \end{bmatrix} + \begin{bmatrix} \mathbf{f}_{D_x}^I \\ \mathbf{f}_{D_y}^I \end{bmatrix} + \begin{bmatrix} \mathbf{f}_{D_x}^{II} \\ \mathbf{f}_{D_y}^{II} \end{bmatrix}, \tag{2.15}$$

where $\mathbf{f}_{A_x}$ and $\mathbf{f}_{A_y}$ are the forces from added mass effects:

$$\begin{bmatrix} \mathbf{f}_{A_x} \\ \mathbf{f}_{A_y} \end{bmatrix} = -\begin{bmatrix} \mathbf{C}_\theta & -\mathbf{S}_\theta \\ \mathbf{S}_\theta & \mathbf{C}_\theta \end{bmatrix} \begin{bmatrix} \mathbf{0} & \mathbf{0} \\ \mathbf{0} & \mu \end{bmatrix} \begin{bmatrix} \dot{\mathbf{V}}_{\mathbf{r_x}} \\ \dot{\mathbf{V}}_{\mathbf{r_y}} \end{bmatrix}, \tag{2.16}$$

where the relative link velocities $\mathbf{V}_{r_x}$ and $\mathbf{V}_{r_y}$ and the relative accelerations in the body frame are given by

$$\begin{bmatrix} \mathbf{V}_{\mathbf{r_x}} \\ \mathbf{V}_{\mathbf{r_y}} \end{bmatrix} = \begin{bmatrix} \mathbf{C}_\theta & \mathbf{S}_\theta \\ -\mathbf{S}_\theta & \mathbf{C}_\theta \end{bmatrix} \begin{bmatrix} \dot{\mathbf{X}} - \mathbf{V}_x \\ \dot{\mathbf{Y}} - \mathbf{V}_y \end{bmatrix}, \tag{2.17}$$

$$\begin{bmatrix} \dot{\mathbf{V}}_{\mathbf{r_x}} \\ \dot{\mathbf{V}}_{\mathbf{r_y}} \end{bmatrix} = \begin{bmatrix} \mathbf{C}_\theta & \mathbf{S}_\theta \\ -\mathbf{S}_\theta & \mathbf{C}_\theta \end{bmatrix} \begin{bmatrix} \ddot{\mathbf{X}} \\ \ddot{\mathbf{Y}} \end{bmatrix} + \begin{bmatrix} -\mathbf{S}_\theta & \mathbf{C}_\theta \\ -\mathbf{C}_\theta & -\mathbf{S}_\theta \end{bmatrix} \begin{bmatrix} \mathrm{diag}(\dot{\theta}) & \mathbf{0} \\ \mathbf{0} & \mathrm{diag}(\dot{\theta}) \end{bmatrix} \begin{bmatrix} \dot{\mathbf{X}} - \mathbf{V}_x \\ \dot{\mathbf{Y}} - \mathbf{V}_y \end{bmatrix}. \tag{2.18}$$

The linear drag forces $\mathbf{f}_{Dx}^I$ and $\mathbf{f}_{Dy}^I$ are given as

$$\begin{bmatrix} \mathbf{f}_{D_x}^I \\ \mathbf{f}_{D_y}^I \end{bmatrix} = -\begin{bmatrix} c_t\mathbf{C}_\theta & -c_n\mathbf{S}_\theta \\ c_t\mathbf{S}_\theta & c_n\mathbf{C}_\theta \end{bmatrix} \begin{bmatrix} \mathbf{V}_{r_x} \\ \mathbf{V}_{r_y} \end{bmatrix}. \tag{2.19}$$

Whereas the nonlinear drag forces $\mathbf{f}_{D_x}^{II}$ and $\mathbf{f}_{D_y}^{II}$ are

$$\begin{bmatrix} \mathbf{f}_{D_x}^{II} \\ \mathbf{f}_{D_y}^{II} \end{bmatrix} = -\begin{bmatrix} c_t\mathbf{C}_\theta & -c_n\mathbf{S}_\theta \\ c_t\mathbf{S}_\theta & c_n\mathbf{C}_\theta \end{bmatrix} \mathrm{sgn}\left(\begin{bmatrix} \mathbf{V}_{r_x} \\ \mathbf{V}_{r_y} \end{bmatrix} \right) \begin{bmatrix} \mathbf{V}_{r_x}^2 \\ \mathbf{V}_{r_y}^2 \end{bmatrix}. \tag{2.20}$$

The torque applied by the water on all links are

$$\tau = -\lambda_1\mathbf{I}_n\ddot{\boldsymbol{\theta}}_i - \lambda_2\mathbf{I}_n\dot{\boldsymbol{\theta}} - \lambda_3\mathbf{I}_n\dot{\boldsymbol{\theta}}|\dot{\boldsymbol{\theta}}|. \tag{2.21}$$

By defining

$$\mathbf{f_D} = \begin{bmatrix} \mathbf{f}_{Dx} \\ \mathbf{f}_{Dy} \end{bmatrix} = \begin{bmatrix} \mathbf{f}_{Dx}^I + \mathbf{f}_{Dx}^{II} \\ \mathbf{f}_{Dy}^I + \mathbf{f}_{Dy}^{II} \end{bmatrix}, \tag{2.22}$$

the model (Equations 2.1 and 2.2) is complete. Still, one needs to find the values for the drag-force parameters c_t, c_n, λ_2, λ_3, and the added mass parameters μ_n and λ_1.

2.3 Drag Force Model Variations

The existing model assumes the underwater robotic snake being made up of n identical links. Further assuming each link is approximated as an elliptical cylinder, the first and last links will have flat circular shapes perpendicular to the angle of attack, with sharp edge transitions to the remaining links. This is not the case in most practical applications, such as for Mamba, where more aerodynamically shaped head and tail modules are attached. Adding head and tail modules improves the hydrodynamic properties by reducing the amount of vortexes around the snake, making the flow more laminar, and thus less drag is experienced.

The proposed mathematical model presented in the previous section can be expanded in different forms. A number of variations are explored in this thesis that will include the head and tail in addition to the existing link modules. The model is further extended to include individual drag coefficients for linear and quadratic drag. In addition, a coupling between the velocity in body y direction and the force in body x direction is introduced. All models assume the simple case of the relative joint angles being equal to zero, $\phi_i = 0$, $i \in 1, \ldots, n-1$. Resulting in all the links in the robot being configured as a straight line.

From the fluid forces acting on one link, Equation 2.6, the total drag force for a snake configuration with n links can be written, with simplified velocity notation

$$\mathbf{f}_1 = n\left(-\hat{\mathbf{C}}_D v - \hat{\mathbf{C}}_D \operatorname{sgn}(v)\, v^2\right), \tag{2.23}$$

where $\mathbf{f}_1$ is the original drag force model and $\hat{\mathbf{C}}_D$ is the same as in Equation 2.7. The first variation, $\mathbf{f}_2$, distinguishes between the drag coefficients for linear and quadratic drag, while still assuming the snake module configuration only being made up of link modules.

$$\mathbf{f}_2 = n\left(\mathbf{f}^{\mathrm{I}}_{D,L} + \mathbf{f}^{\mathrm{II}}_{D,L}\right), \tag{2.24}$$

where the linear and nonlinear drag forces of a link module, $\mathbf{f}^{\mathrm{I}}_{D,L}$ and $\mathbf{f}^{\mathrm{I}}_{D,L}$ are written as

$$\mathbf{f}^{\mathrm{I}}_{D,L} = \begin{bmatrix} -\frac{1}{2}\pi\rho(\frac{(a+b)}{2})2lC^{\mathrm{I}}_f & 0 \\ 0 & -\frac{1}{2}\rho 2a2lC^{\mathrm{I}}_d \end{bmatrix} \begin{bmatrix} v_x \\ v_y \end{bmatrix},$$

$$\mathbf{f}^{\mathrm{II}}_{D,L} = \begin{bmatrix} -sgn(v_x)\frac{1}{2}\pi\rho(\frac{(a+b)}{2})2lC^{\mathrm{II}}_f & 0 \\ 0 & -sgn(v_y)\frac{1}{2}\rho 2a2lC^{\mathrm{II}}_d \end{bmatrix} \begin{bmatrix} v_x^2 \\ v_y^2 \end{bmatrix},$$

where C^{I}_f, C^{II}_f, C^{I}_d and C^{II}_d are the linear and nonlinear drag coefficients for a link module, v_x and v_y are the fluid velocities in x and y direction expressed in body frame. Extending to this, the next model variation also includes linear and quadratic drag terms for the head and tail modules

$$\mathbf{f}_3 = \mathbf{f}^{\mathrm{I}}_{D,HT} + \mathbf{f}^{\mathrm{II}}_{D,HT} + n(\mathbf{f}^{\mathrm{I}}_{D,L} + \mathbf{f}^{\mathrm{II}}_{D,L}), \tag{2.25}$$

where

$$\mathbf{f}^{\mathrm{I}}_{D,HT} = \begin{bmatrix} -\frac{1}{2}\pi\rho abC^{\mathrm{I}}_{f_{HT}} & 0 \\ 0 & -\frac{1}{2}\rho A_{HT}C^{\mathrm{I}}_{d_{HT}} \end{bmatrix} \begin{bmatrix} v_x \\ v_y \end{bmatrix}, \tag{2.26}$$

$$\mathbf{f}_{D,HT}^{\mathrm{II}} = \begin{bmatrix} -sgn(v_x)\frac{1}{2}\pi\rho a^2 C_{f_{HT}}^{\mathrm{II}} & 0 \\ 0 & -sgn(v_y)\frac{1}{2}\rho A_{HT} C_{d_{HT}}^{\mathrm{II}} \end{bmatrix} \begin{bmatrix} v_x^2 \\ v_y^2 \end{bmatrix}, \tag{2.27}$$

are the linear and nonlinear drag force contributions for the head and tail modules, where A_{HT} is the characteristic area of the head and tail modules in y direction, $C_{f_{HT}}^{\mathrm{I}}$, $C_{f_{HT}}^{\mathrm{II}}$, $C_{d_{HT}}^{\mathrm{I}}$ and $C_{d_{HT}}^{\mathrm{II}}$ are the linear and nonlinear drag coefficients for the combined head and tail modules. The next model variation additionally includes effects on x forces from v_y

$$\mathbf{f}_4 = \mathbf{f}_{D,HT}^{\mathrm{I}} + \mathbf{f}_{D,HT}^{\mathrm{II}} + n(\mathbf{f}_{D,L}^{\mathrm{I}} + \mathbf{f}_{D,L}^{\mathrm{II}}) + \mathbf{f}_{D,XY}^{\mathrm{I}} + \mathbf{f}_{D,XY}^{\mathrm{II}}, \tag{2.28}$$

where the fluid forces in body x induced by v_y are

$$\mathbf{f}_{D,XY}^{\mathrm{I}} = \begin{bmatrix} 0 & -sgn(v_y)\rho a l C_{XY}^{\mathrm{I}} \\ 0 & 0 \end{bmatrix} \begin{bmatrix} v_x \\ v_y \end{bmatrix},$$

$$\mathbf{f}_{D,XY}^{\mathrm{II}} = \begin{bmatrix} 0 & \rho a l C_{XY}^{\mathrm{II}} \\ 0 & 0 \end{bmatrix} \begin{bmatrix} v_x^2 \\ v_y^2 \end{bmatrix},$$

where C_{XY}^{I}, C_{XY}^{II} are the linear and nonlinear drag coefficients. The next variation omits linear drag for the head and tail as well as for the cross term

$$\mathbf{f}_5 = \mathbf{f}_{D,HT}^{\mathrm{II}} + n(\mathbf{f}_{D,L}^{\mathrm{I}} + \mathbf{f}_{D,L}^{\mathrm{II}}) + \mathbf{f}_{D,XY}^{\mathrm{II}}. \tag{2.29}$$

The last model variation is built on the general fluid drag force model $f = \frac{1}{2}\rho v^2 C_d A$, considering only the nonlinear drag effects. Here, A is the area of the body projected in 2D towards the angle of the flow, denoted the reference area.

$$\mathbf{f}_6 = \begin{bmatrix} \frac{1}{2}\rho A_x C_{d,x} v_x^2 & 0 \\ 0 & \frac{1}{2}\rho A_y(n) C_{d,y} v_y^2 \end{bmatrix}, \tag{2.30}$$

where A_x and A_y are the reference areas in x and y direction.

$$A_x = \pi a b, \tag{2.31a}$$

$$A_y = A_{y,H} + n2l2a + A_{y,T}, \tag{2.31b}$$

where $A_{y,H} = 5.919 \times 10^{-3}$ m^2 and $A_{y,T} = 4.757 \times 10^{-3}$ m^2 are the reference areas for the head and tail.

The different model variations of the drag model will be investigated later based on the obtained forces from the simulations and experiments, in order to conclude on a more precise model of the hydrodynamic effects. Note that in [23], only the drag forces $\mathbf{f}_1$ are considered in the hydrodynamic model. However, in this thesis the hydrodynamic model is extended by variations including different combinations of linear and quadratic drag, contributions in x forces from flow in y direction, and effects caused by the head and tail modules. This thesis will later identify the fluid parameters for the different model variations in order to obtain the most precise one.

2.4 Fluid Parameters

2.4.1 Original Model

From the original model, there are six expressions dependent on the unknown fluid coefficients:

$$c_t = \frac{1}{2}\rho\pi C_f \frac{(a+b)}{2} 2l, \tag{2.32}$$

$$c_n = \frac{1}{2}\rho C_d 2a 2l, \tag{2.33}$$

$$\mu_n = \rho\pi C_A a^2 2l, \tag{2.34}$$

$$\lambda_1 = \frac{1}{12}\rho\pi C_M (a^2 - b^2)^2 l^3, \tag{2.35}$$

$$\lambda_2 = \frac{1}{6}\rho\pi C_f (a+b) l^3, \tag{2.36}$$

$$\lambda_3 = \frac{1}{8}\rho\pi C_f (a+b) l^4. \tag{2.37}$$

As mentioned previously, c_t, c_n, λ_2, λ_3 are the drag-force parameters, while μ_n and λ_1 are for the added mass effects. These parameters are further dependent on the fluid coefficients given in Table 2.1, which this thesis aims to identify.

Coefficients	
C_f	Drag coefficient in x direction
C_d	Drag coefficient in y direction
C_A	Addded mass coefficient

Table 2.1: Fluid coefficients to be identified.

In this thesis does not consider identifying the added mass inertia coefficient C_M. Neither is added mass in x direction as this can be assumed zero compared to the mass of a long slender body.

Existing Estimates

The simulations done in *Innovation in Underwater Robots - Biologically Inspired Swimming Snake Robots* [22] are based on the estimates given in Table 2.2, with different values depending on the motion of the robot, as mentioned in Chapter 1.

The underwater snake robot is made up of $n = 9$ links. The links are approximated as elliptical cylinders of length $2l = 2 \times 0.18$m, major diameter $2a = 2 \times 0.055$m and minor diameter $2b = 2 \times 0.05$m.

The values are chosen under the assumption of a steady-state flow [26], [17], which results in setting the added mass inertia coefficient to its theoretical value, $C_M = 1$, as the overall motion of the system is not significantly affected by this coefficient. As expected, C_f is chosen smaller for the eel-like motion than for lateral undulation, as the oscillations of the head of the snake are smaller in this case and thus having less fluid drag in x direction.

	Lateral undulation	Eel-like motion	Steady-state theoretical coeff.
C_f	0.3	0.17	$0.01 - 0.03$
C_d	1.75	1.75	1.0
C_A	1.5	1.5	1.0
C_M	1.0	1.0	1.0

Table 2.2: Fluid coefficients used in [22] and [18].

2.4.2 Model Variations

The numerous possible drag coefficients for the model variations presented in the last section are overviewed in Table 2.3.

Model	Corresponding fluid coefficients
$\mathbf{f_1}$	C_f, C_d
$\mathbf{f_2}$	C_f^{I}, C_d^{I}, C_f^{II}, C_d^{II}
$\mathbf{f_3}$	C_f^{I}, C_d^{I}, C_f^{II}, C_d^{II}, $C_{f_{HL}}^{\mathrm{I}}$, $C_{d_{HL}}^{\mathrm{I}}$, $C_{f_{HL}}^{\mathrm{II}}$, $C_{d_{HL}}^{\mathrm{II}}$
$\mathbf{f_4}$	C_f^{I}, C_d^{I}, C_f^{II}, C_d^{II}, $C_{f_{HL}}^{\mathrm{I}}$, $C_{d_{HL}}^{\mathrm{I}}$, $C_{f_{HL}}^{\mathrm{II}}$, $C_{d_{HL}}^{\mathrm{II}}$, C_{XY}^{I}, C_{XY}^{II}
$\mathbf{f_5}$	C_f^{I}, C_d^{I}, C_f^{II}, C_d^{II}, $C_{f_{HL}}^{\mathrm{II}}$, $C_{d_{HL}}^{\mathrm{II}}$, C_{XY}^{II}
$\mathbf{f_6}$	C_f, C_d

Table 2.3: Fluid coefficients for model variations.

2.5 Least Squares Estimation

To estimate the drag coefficients in the hydrodynamic force models, a least-square estimation scheme is used, [8]. When the velocities are known, the force model can be written linearly, as shown in Equation 2.44. This makes the problem suitable for a least squares solver. As the inputs to the system, v_x and v_y are known, and the output forces are obtained from experiments or simulations, the force models from Chapter 2.3 can be rewritten the following form, using $\mathbf{f_2}$ as an example:

$$\mathbf{f_2} = \begin{bmatrix} U_{x_1} & 0 \\ 0 & U_{y_1} \end{bmatrix} \begin{bmatrix} C_{f_L}^I \\ C_{d_L}^I \end{bmatrix} + \begin{bmatrix} U_{x_2} & 0 \\ 0 & U_{y_2} \end{bmatrix} \begin{bmatrix} C_{f_L}^{II} \\ C_{d_L}^{II} \end{bmatrix}, \tag{2.38}$$

where

$$U_{x_1} = -\frac{1}{2}\pi\rho a^2 v_x, \tag{2.39}$$

$$U_{x_2} = -\mathrm{sgn}(v_x)\frac{1}{2}\pi\rho a^2 v_x^2, \tag{2.40}$$

$$U_{y_1} = -\frac{1}{2}\rho A_{HT} v_y, \tag{2.41}$$

$$U_{y_2} = -\mathrm{sgn}(v_y)\frac{1}{2}\rho A_{HT} v_x^2 \tag{2.42}$$

$$, \tag{2.43}$$

are known variables. The estimation can now be written as

$$\hat{\mathbf{f}}_2 = \begin{bmatrix} U_{x_1}\alpha_{11} + U_{x_2}\alpha_{12} & 0 \\ 0 & U_{y_1}\alpha_{21} + U_{y_2}\alpha_{22} \end{bmatrix} \tag{2.44}$$

where

$$\alpha_{11} = \hat{C}^I_{f_L}, \tag{2.45}$$
$$\alpha_{12} = \hat{C}^{II}_{f_L}, \tag{2.46}$$
$$\alpha_{21} = \hat{C}^I_{d_L}, \tag{2.47}$$
$$\alpha_{22} = \hat{C}^{II}_{d_L}, \tag{2.48}$$
$$\tag{2.49}$$

are the unknown coefficients. The estimated coefficients which gives the minimum of the sum of squared errors,

$$\min(SSE) = \min(\sum(\mathbf{f} - \hat{\mathbf{f}}_2))^2, \tag{2.50}$$

can be found by using a least square estimation, where $\mathbf{f}$ is the forces obtained from simulations or experiments and $\hat{\mathbf{f}}_2$ is the estimated forces. The estimation returns the drag force coefficients from Table 2.3. The least squares algorithm is implemented in MATLAB using the `lsqnonneg`, which impose an additional requirement of non-negative outputs.

Chapter 3

Simulations

This chapter covers the theoretical identification of the fluid coefficients based on the simulation schemes done with SolidWorks and WADAM. The geometry of the underwater robotic snake robot Mamba has been considered in the simulations with module configurations ranging from head and tail with one link (H1LT) up to nine links (H9LT). By varying the number of links, it is possible to investigate how the identified fluid coefficients are dependent on the length of the robot.

3.1 Flow Simulation

Theoretical values for the drag coefficients C_d and C_f are calculated with Solidworks, using the Flow Simulation extension. Solidworks has a large user base and offers a fairly easy user interface. As the models for Mamba are designed in Solidworks, there is no need for translating the models to different formats prior to running the flow simulations. The flow simulation package simulates fluid flow, heat transfer and fluid forces using CFD. The CFD calculations builds on solving the Navier-Stokes equations, which for 3D incompressible flow, are:

$$\frac{\partial v_x}{\partial t} + v_x\frac{\partial v_x}{\partial x} + v_y\frac{\partial v_x}{\partial y} + v_z\frac{\partial v_x}{\partial z} = \frac{F_x}{\rho} - \frac{1}{\rho}\frac{\partial P}{\partial x} + \nu(\frac{\partial^2 v_x}{\partial x^2} + \frac{\partial^2 v_x}{\partial y^2} + \frac{\partial^2 v_x}{\partial z^2}), \quad (3.1)$$

$$\frac{\partial v_y}{\partial t} + v_x\frac{\partial v_y}{\partial x} + v_y\frac{\partial v_y}{\partial y} + v_z\frac{\partial v_y}{\partial z} = \frac{F_y}{\rho} - \frac{1}{\rho}\frac{\partial P}{\partial y} + \nu(\frac{\partial^2 v_y}{\partial x^2} + \frac{\partial^2 v_y}{\partial y^2} + \frac{\partial^2 v_y}{\partial z^2}), \quad (3.2)$$

$$\frac{\partial v_z}{\partial t} + v_x\frac{\partial v_z}{\partial x} + v_y\frac{\partial v_z}{\partial y} + v_z\frac{\partial v_z}{\partial z} = \frac{F_z}{\rho} - \frac{1}{\rho}\frac{\partial P}{\partial z} + \nu(\frac{\partial^2 v_z}{\partial x^2} + \frac{\partial^2 v_z}{\partial y^2} + \frac{\partial^2 v_z}{\partial z^2}), \quad (3.3)$$

where the parameters are stated in Table 3.1. The solver can return a wide range of values, where for this thesis, forces in x and y directions, and torques in z direction, expressed in body axis, are measured as these are the necessary quantities for obtaining the drag coefficients and are also available for measurement in the experimental approaches. In addition, the parameters can be adapted to a complete three-dimensional model of the snake in the future. The mathematics behind Solidworks Flow Simulation solver is well documented in their technical reference [46].

Parameter	Definition
P	Fluid static pressure
t	Time
ρ	Fluid density
ν	Kinematic viscosity
x, y, z	coordinate axes
v_x, v_y, v_z	Fluid velocity in x, y, and z direction
F_x, F_y, F_z	Body force on fluid in x, y, and z direction

Table 3.1: Parameters in the 3D incompressible Navier-Stokes equations.

A downside to Solidworks Flow Simulation is that the simulations are stationary. This means, for a given fluid flow input, the object can not easily be rotated during the simulation to record the forces and moments at different angles of attack. A solution is to do a so-called *parametric study* where several simulations are run with different inputs. In the initial case the flow is in the x direction and zero in the y direction. Using simple trigonometry, the input fluid flow velocities in x and y direction is altered for each case from 0 degrees ($v_y = 0$) to 90 degrees ($v_x = 0$). Having the x and y fluid flow inputs as a function of an angle, θ, a virtual rotation of the object is achieved. Figure 3.1 illustrates the concept where the body is virtually rotated θ degrees about the global coordinate axes.

NOTE: For the model in Chapter 2, θ_i is defined as the angle between link i and the global x axis. As the 3D geometry models are connected with the joint angles $\phi_i = 0$ degrees, θ_i is equal for all links i. Hence θ is used to denote the angle of attack for the snake module configuration.

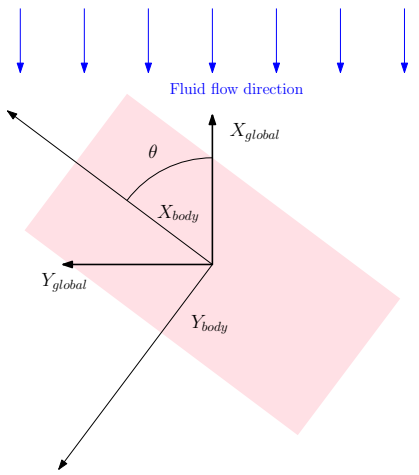

Figure 3.1: Virtual rotation of body in Solidworks flow simulations.

3.1.1 Geometry

The 3D geometry models for the snake modules are made in Solidworks. The three modules that fully defines the snake configurations are: Head, Link and Tail (Figure 3.2). All modules are designed to be interconnected with the other modules, resulting in a straight-forward mounting process of the 3D printed modules. No physical material is defined for the modules, resulting in a smooth outer surface. Figure 3.3 show the H2LT configuration.

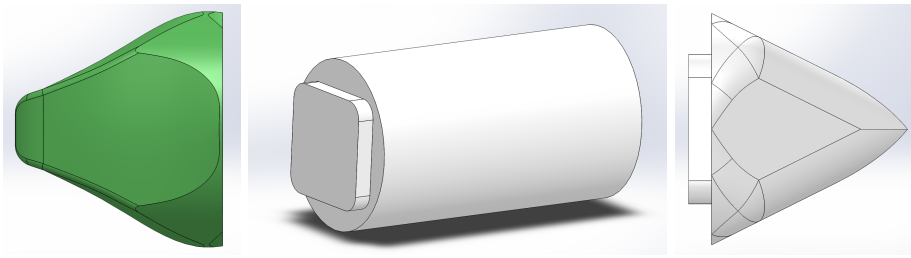

(a) Head module. (b) Link module. Extrusion in front for mounting with other modules. (c) Tail module.

Figure 3.2: The three snake geometry models.

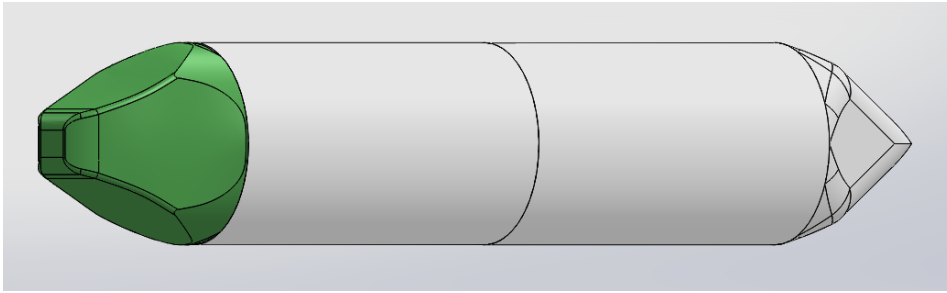

Figure 3.3: H2LT configuration: Head module (green) connected with two links and tail.

3.1.2 SolidWorks Simulation Parameters

The simulation parameters for the flow simulations are stated in Table 3.2. A brief guide for setting up SolidWorks Flow Simulation is found in Appendix A.2.2.

Meshing

Solidworks Flow Simulation has a built in automatic meshing tool. The user can input the refinement of the mesh on a scale from 1 to 7, where 7 is the most refined mesh. The mesh setting directly affects the simulation time needed as a finer mesh

Parameter	Setting
Analysis type	External
Liquid	Water
Flow type	Laminar and Turbulent
Default wall thermal condition	Adiabatic wall
Roughness	0 μm
Pressure	101325 Pa
Temperature	293.15 K

Table 3.2: Flow simulation settings.

can create million of cells that will be computed individually, and thus exponentially increasing the computational time. It might therefore be necessary with a trade-off between accuracy and simulation time. A wide range of preliminary simulations has been performed with different mesh settings. The results showed that the default mesh setting (refinement level 3) was to coarse, yielding inaccurate results. Whereas the highest mesh setting for the largest objects (H9LT) created an amount of mesh cells that drained the resources (CPU, RAM) of the computers and the simulation crashed. As the optimal mesh is hard to find, the final simulations where done with mesh setting 6. This secures relatively accurate results, but demands long computing time. Figure 3.4 illustrates the mesh cells.

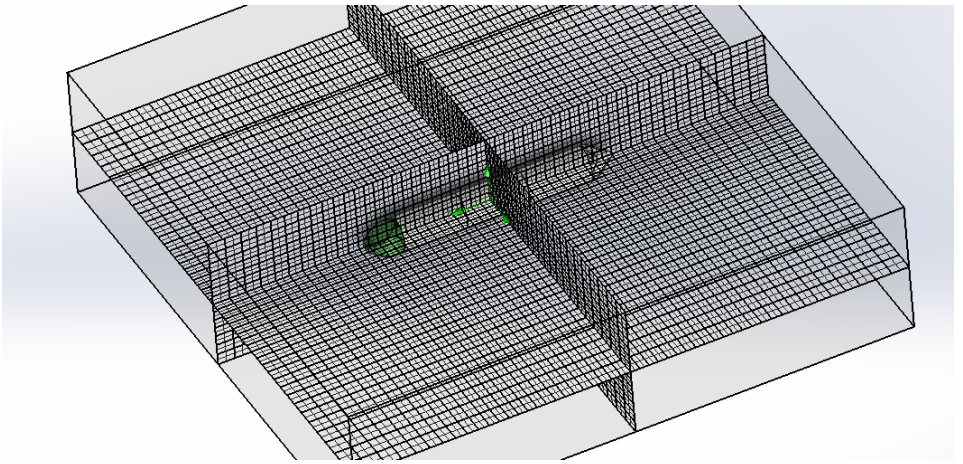

Figure 3.4: Illustration of meshing the H3LT snake configuration.

Computational Domain

The Computational Domain (CD) is the 3D space (a box) around the object where the mesh cells are calculated. Reducing the CD results in fewer mesh cells and thus significantly reduces the computational time needed. However, by constraining CD too much, valuable information for the convergence tests done in the simulation

are lost. In the latter case, the results may be incorrect, even with a highly refined mesh. Several test were done analysing the pressure and velocity profiles around the geometry to determine the smallest possible CD without the loss of information. The test concluded in the CD settings for a snake geometry with n links presented in Table 3.3.

Axis direction	**Size**
x +	1×Geometry length
x -	1.5×Geometry length
y +	1×Geometry length + 0.34 m
y -	0.5×Geometry length + 0.34 m
z +/-	3×Major Diameters
Geometry length $= l_{\text{Head}} + nl_{\text{link}} + l_{\text{tail}}$	

Table 3.3: CD settings for n links. The distances are the location of the CD border from the center of the snake along the coordinate axes.

The CD must be configured to best suit a parametric simulation run for angles $\theta \in [0 \dots 90]$ degrees and velocities $v \in [0.1, 0.2, \dots, 0.4]$ m/s. Figure 3.5 illustrates the CD and velocity cut plots for the H9LT configuration for a velocity of 0.5 m/s at an angle $\theta = 45$ degrees. CD is reduced in positive x axis and negative y axis as the majority of this area has no impact on the results as the incoming flow is uniform and of a constant velocity.

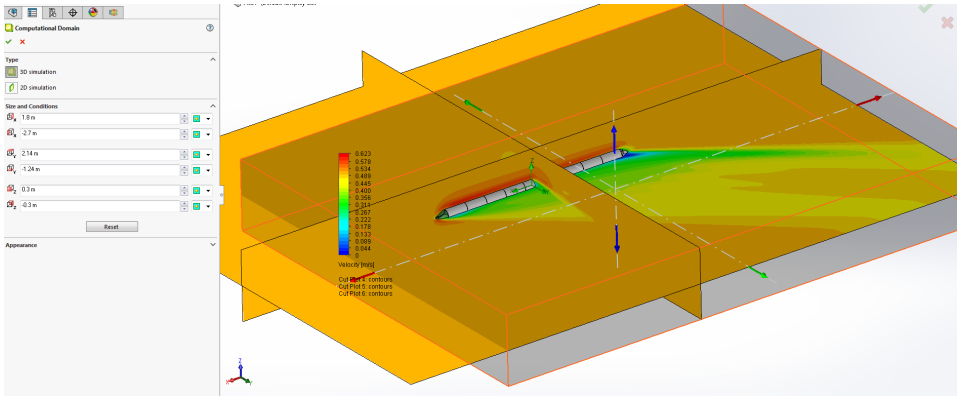

Figure 3.5: The resulting CD (Grey box with orange edges) for the H9LT configuration.

A comparison of two mesh settings and the size of the CD in seen in Figure 3.6. The figure show preliminary test simulations for a cylinder for a varying θ at velocity $v = 0.3$ m/s. The most accurate result is obtained for the highest mesh refinement, mesh = 7, and with the default CD. Lowering the mesh to its default value of 3, the returned forces are less. This is a result of the coarser mesh causing a lack of information about the true geometry of the cylinder. For the most refined

mesh level, a conservatively constrained CD yields almost identical results as for a default CD. Further decreasing the CD size leads to a less consistent result.

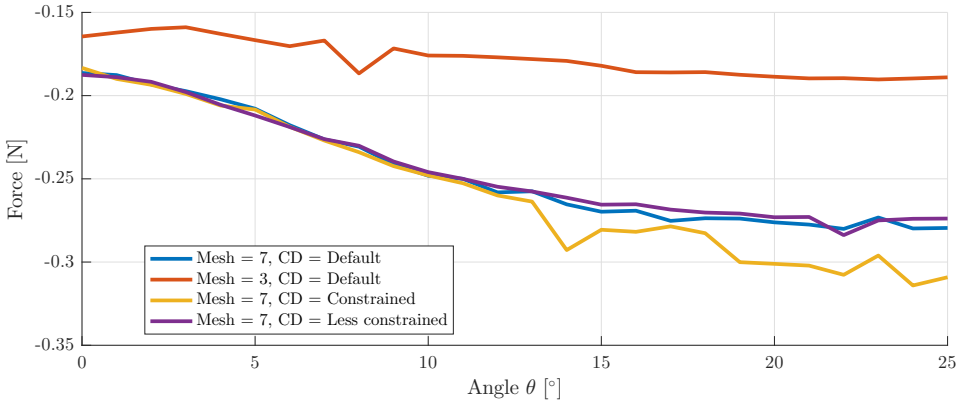

Figure 3.6: Comparison of mesh refinement and CD size.

3.1.3 Solidworks Simulation Cases

Simulations are done on the CAD-files for the actual 3D printed modules that will be used in the experimental approach. The 3D printed snake links have the same dimensions as the real snake link modules. Simulations are done for several cases with different snake module configurations.

	Velocity [m/s]		**Angle** θ [deg]		No. of
	Range	Step size	Range	Step size	simulations
Case 1	[0.02 to 1]	0.02	0	—	50
Case 2	0.1	—	[0 to 90]	3	31
Case 3	0.2	—	[0 to 90]	3	31
Case 4	0.3	—	[0 to 90]	3	31
Case 5	0.4	—	[0 to 90]	3	31
Simulation scenarios per configuration: 174					
Total number of simulations: 1566					

Table 3.4: Simulation cases for drag coefficients for each body configuration H1LT through H9LT.

Table 3.4 overviews the performed simulation cases done on each body configuration H1LT through H9LT. Case 1 considers $\theta = 0$ degrees, for a set of 50 velocities from 0.02 to 1 m/s. Case 2 considers a fixed-velocity fluid flow where for each simulation scenario the angle of the flow, θ, with respect to the z-axis, increases with 3 degrees from 0 in the first scenario up to 90 degrees for the final scenario. Case 3 to 5 are identical to case 2, but for different velocities. Each body configuration results in 174 different simulation scenarios, resulting in a total of 1566 simulations for all body configurations. For each body configuration, the

complete set of simulation cases are loaded and run as a *parametric study* where the user only needs to manually start the first simulation case and the rest is run consecutively.

Computational Resources and Simulation Durations

The simulations are run on four physical computers and two NTNU servers, all with Solidworks 2016 x64 SP02 installed. The specifications for the computers are listed in Table 3.5. The two servers are powerful, but are available to multiple users simultaneously, resulting in shared resources and the potential of not fully exploiting the full resources of the servers. Each computer/server runs all 174 simulations for one configuration, which means six configurations can be simulated in parallel.

Computer	CPU	Cores	RAM
Computers 1-3	Intel Core i7-4770 3.4 GHz	8	16 GB
Computer 4	Intel Core i5-3470 3.2 GHz	4	16 GB
Server 1	Intel Xeon CPU E5-2690 v4 2.60 GHz ×2	56	192 GB
Server 2	Intel Xeon CPU E5-2690 2.90 GHz × 2	32	192 GB

Table 3.5: Specifications for the computers used for the simulations

The CFD calculations are significantly computationally demanding, even for simple objects like a cylinder and simulations running on modern powerful computers. As each body configuration requires an unique CD, the running time for each simulation increases with the number of links in the body configuration. For the H2LT configuration, the CD size results in $\sim 8 \times 10^5$ cells, whereas the number of cells are 2.8×10^6 for the H9LT configuration. As a result, the simulation times for each simulation scenario varies from 45 minutes per case for H1LT on computer 4, and one hour per scenario for H2LT on computer 1, up to about five hours for H9LT. It should be noted that these are estimated average computing times and will vary with the different scenarios within each simulation case. In addition, variations in the computing time is present due to available resources on the computers and the load on the two servers the simulations are run on. The resulting total simulation time is thus approximately 3800 hours, approximately 5.2 months, if each simulation were to be run consecutively on a single computer. Running the simulations on multiple computers reduces the total simulation time. Still, the amount of simulation time required is substantial.

3.1.4 Solidworks Simulations Output

Solidworks outputs an Excel sheet containing the calculated forces and torques for each of the runs. The output files are found in Appendix A.2.1. In addition, Solidworks can save the full simulation results. The full results can be utilized by the user to further analyse the obtained results by studying flow patterns, pressure distribution and more. However, the full results accumulates to hundreds of gigabytes of data and the option to save the full results have been disabled.

3.1.5 Verification

The CFD calculations from Solidworks should be verified. In [9], verification simulations are run for simple geometric objects where reference values for the drag coefficients are available. A test is performed on a square rod with a fluid flow at $v = 0.085$ m/s parallel to the rod. The reference value [6], is $C_{d_{ref}} = 0.87$, while the value obtained from the simulation is $C_d = 0.8552$. A similar test is performed for a sphere. The reference in this case is $C_{d_{ref}} = 0.12$ and from the simulation $C_d = 0.1130$. The test show that the simulations are fairly accurate for simple geometries. As the geometric objects in this thesis is fairly simple, the verification test results suggests Solidworks to be a reasonable choice of software for obtaining drag coefficients for this thesis.

3.2 Added Mass

This section overviews the process of finding the added mass coefficients using the software extension WADAM from DNV GL's software package Sesam [7].

3.2.1 Panel Method (WADAM/WAMIT)

As mentioned in Chapter 1.4.1, WADAM builds directly on WAMIT for solving for the added mass coefficients, but offers a better user interface. WAMIT uses the panel method to solve for the hydrodynamic coefficients. This method builds on dividing the body into N small panels and solving the Green integral equation for each panel to find the velocity potential, Φ over each element.

$$\frac{1}{2}\Phi_i + \sum_{j=1}^{N} \Phi_j \int_{S_j} dS_X \frac{dG(\vec{X};\vec{\varepsilon_i})}{dn_j} = \sum_{j=1}^{N} \int_{j=1} dS_X G(\vec{X};\vec{\varepsilon_i}) \quad i = 1:N, \tag{3.4}$$

where Φ_i is the unknown velocity potential value, i is the facet number, S_j is the surface of each panel, and $G(\vec{X};\vec{\varepsilon_i})$ is the Green function. By solving for all panels, the total velocity potential over the body, Φ is obtained. Further, the dynamic pressure, p_{dyn} is found by using the linearized Bernoulli equation

$$p_{dyn} = -\rho \frac{\partial \Phi}{\partial t}. \tag{3.5}$$

The velocity over the surface is found by applying the Bernoulli equation

$$\frac{\partial \Phi}{\partial t} + \frac{1}{2}\left|\nabla \Phi\right|^2 + \frac{p}{\rho} + gz = C, \tag{3.6}$$

where z is the water depth. By integrating the velocity potential over the body, potential damping and added mass can be found

$$A_{kj}(\omega) = \Re\left[\rho \int_{S_{OB}} \Phi_j n_k \, dS\right] \tag{3.7}$$

$$B_{kj}(\omega) = -\omega \Im\left(\rho \int_{S_{OB}} \Phi_j n_k \, dS\right) \tag{3.8}$$

3.2.2 Meshing

The geometric shapes to be used with WADAM has to be a mesh object in the WAMIT file format *Geometric Data File* (.gdf). Solidworks is not capable of exporting 3D objects in this format and thus another software tool, such as Rhinoceros 5 [42] can be used for translating the geometric models. For each snake configuration, H1LT through H9LT, the assembled geometry is exported from Solidworks as a *Standard for the Exchange of Product Data* (.step) formatted file, a common file format for sharing geometry between different CAD software. The .step file is loaded into Rhinoceros 5 and the object is converted to a Non-Uniform Rational B-splines (NURBS) meshed object using the function *From NURBS object*. The resulting meshed object is exported as a .gdf file and is ready for WADAM or WAMIT. The process is illustrated in Figure 3.7

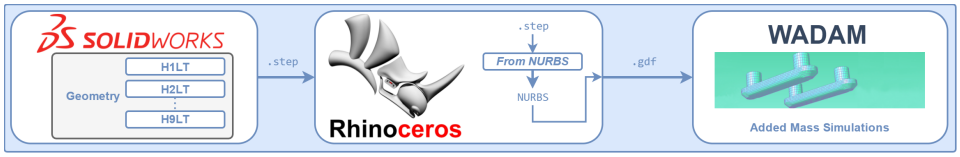

Figure 3.7: Process for translating Solidworks geometry files to be compatible with WADAM.

WADAM has an upper limit of 2000 elements in the meshed geometry file [5], and thus complex 3D objects may violate this limit. It is possible to adjust the parameters in Rhinoceros when converting the .step file to a NURBS object to limit the amount of mesh elements. However, this may lead to disfigured and inaccurate meshed objects. As an example, a circular shape may be broken down into triangular panels or other polygons. The further the amount of panels is limited, the more the circular object is disfigured. A second option for limiting the complexity of the object is by simplifying the 3D model in Solidworks. The four rounded edges leading from the back of the head towards the very front results in a number of mesh panels exceeding what WADAM is capable of handling. The head model was simplified by making the edge sharper. The simplification does not alter the geometry significantly, while drasticly reducing the number of elements in the meshed model. A comparison of the head module before and after the simplification is seen in Figure 3.8. All geometry files from Solidworks and Rhinoceros are found in Appendix A.1.3.

3.2.3 Simulation Parameters

Launching Sesam, the WADAM-wizard is opened to configure the simulation parameters. The frequency-independent added mass matrix is of interest, hence using a water depth of 300 meters, the snake is placed 100 meters below the water surface. It can thus be assumed that the added mass coefficients are not influenced by the wave frequency and are constant, making the added mass purely dependent on the acceleration of the body. A uniform mass distribution is assumed, and that the

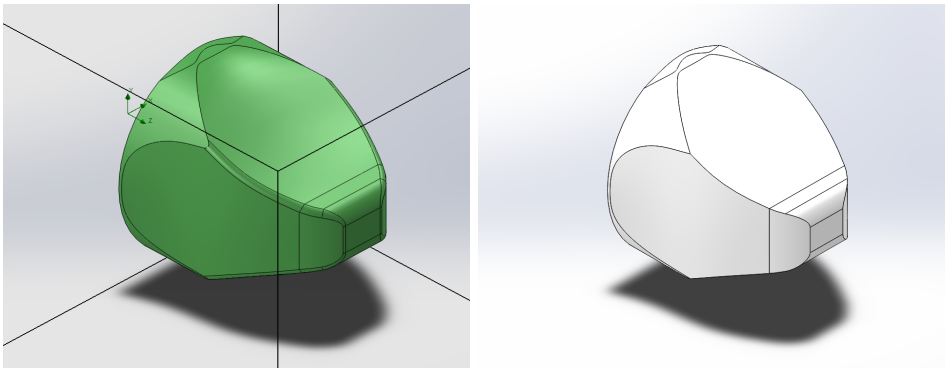

(a) Original. (b) Simplified.

Figure 3.8: Original (left) and simplified head module.

center of buoyancy (CB) is located at the CM of the body. A complete user guide for recreating the simulation runs can be found in Appendix A.1.2.

3.2.4 WADAM Simulations Output

The WADAM analysis is completed quickly compared to the CFD simulations for finding the drag coefficients in Solidworks. For each simulation of the different snake configurations, H1LT through H9LT, WADAM stores the results in a text file named `WADAM1.LIS` where the 6×6 dimensionless added mass matrix, $\mathbf{A}^D$ is found. The first two entries on the diagonal are the elements of interest as these represent the added mass coefficients in x and y directions. The non-dimensionless elements are found by multiplying with the water density and the volume of the object

$$\mathbf{A}_i^{ND} = \mathbf{A}_i^D \rho V_i, \tag{3.9}$$

where the superscript denotes non-dimensionless(ND) and dimensionless (D), V_i is the volume of body i, and the subscript $i \in \{H, T, HLT, H2LT, H3LT, ..., H9LT\}$ denotes the module or the configuration of modules. Both the volume of the body and the water density is found in the .LIS file.

The first two diagonal elements of $\mathbf{A}^{ND}$ equals μ_t and μ_n in Equation 2.8, whereas the second diagonal elements of $\mathbf{C}^D$ corresponds to C_A on the right side of Equation 2.8. The added mass coefficient in x direction, μ_t, is assumed zero in the original model, as is a valid assumption for a slender body. However, the following notation is introduced to allow for any non-zero results, which can confirm the assumption.

$$\hat{\mathbf{C}}_A^i = \begin{bmatrix} \mu_t & 0 \\ 0 & \mu_n \end{bmatrix} = \begin{bmatrix} \rho\pi C_{A_i,x}^D ab2l & 0 \\ 0 & \rho\pi C_{A_i,y}^D ab2l \end{bmatrix}, \tag{3.10}$$

where the superscripts and subscripts are similar to that of Equation 3.9.

It should be noted that not all elements in the complete 6×6 added mass matrices are correct. WADAM uses a radius of gyration in pitch and roll equal the

depth of the submerged body. The roll and pitch added mass will become incorrect. A solution is to do two additional simulation runs with different coordinate axes, and combining the three results. The added mass in surge and sway (x and y direction) are the two quantities of interest in this thesis and the additional simulation cases are disregarded. This would however be of interest for future expansion of the model to 3D.

Chapter 4

Experimental Procedure

This chapter presents the planned and executed experimental setups for identification of the fluid coefficients, including the choice for a force/torque sensor for the measurements. The final experimental procedures and utilized equipment are based on the procedures described in Chapter 1.4.2 and available resources. The two chosen experiments incorporates a passive guided rail towing tank and a circulation tank. For large objects, experiments are often conducted with scaled down models. As the snake module configurations are small, experiments are conducted on full-scale snake module configurations. Thus, scaling errors are avoided.

4.1 Force/Torque Sensor

An important aspect of the experimental approach for identifying the fluid coefficients is the ability to measure forces and torques. A suitable measurement device or devices must be chosen for the experiments. The criteria taken into account for the selection of the sensor device are presented in the following section, together with the chosen sensor.

4.1.1 Sensor Placement and Measurement Range

The physical placement of the sensor is a major factor to consider when selecting the sensor. The ideal case is to mount the sensor in direct proximity to the CM of the snake modules as this point is the center of all calculations and the need for transforming the measurements are eliminated. However, this approach requires a water proof sensor which further increase the complexity and cost of the sensor. An alternative is to mount the sensor above the water surface with a rod extending down to the submerged snake configuration. If the sensor is mounted in this manner, the majority of the forces on the snake from the water will be experienced as torques from the point of view of the sensor. The amount of torque is directly linked to the length of the rod between the sensor and snake. In addition, the length of the rod introduces inaccuracies in the measurements as small disturbances at the end of the rod will spread to the sensor with a higher magnitude. As the snake is required to be submerged at a minimum depth below the water to avoid the surface effects, the

rod will have to be of a certain length. Further, the torque measurements will have to be converted to the appropriate forces and further combined with the other force measurements. The measurement range in torque is usually much less than that of the forces (see Appendix C), resulting in a sensor with too low accuracy in force measurements due to the large range. Although water proof sensors are generally more expensive, the ability to mount the sensor at the snake CM, and thus directly read the correct forces and torques is sought after. Therefore, a waterproof sensor is chosen for the experiments in this thesis.

4.1.2 Sensor Selection Criteria

The following criteria are emphasized on when selecting the appropriate sensor. Some might be conflicting criteria.

Measurement Range

The measurement range of the sensor needs to be within a reasonable area. The accuracy and resolution is directly affected by the full-scale range and should thus be within the estimated needed range.

Accuracy

The accuracy of the sensor is highly important for repeatability, documentation and guaranteeing accurate measurements. Qualities such as low hysteresis, low measurement drift, and linearity are appreciated.

Measurement Resolution

As the expected measurement ranges are quite low, the sensor resolution will have to be of a such magnitude that small changes in force and torque is captured.

Versatility

Although the sensor is chosen specifically for the experiments proposed in this thesis, the possibility to use the sensor for similar experiments is a plus. Other experiments might include experiments on different robotic modules or robotic platforms for future research, as well as other applications.

Decoding

The raw data from the sensor must be easy to decode, and so solutions for analog to digital signal processing and software user interface will be considered. The possibility for incorporating the sensor readings into already existing software solution is important. Many of the systems for controlling the underwater snake robot Mamba are employed using National Instrument's LabView, it follows that support for LabView is of great advantage.

Construction

The sensor should be of high-end build quality and be able to withstand being submerged in at least two meters depth over a longer period of time. Its physical size must be small enough to fit inside a snake module. The experiments might require multiple accounts of mounting and dismantling of the sensor to the snake and the experimental rig, and it follows that the unit is built so this is viable and will not result in the sensor housing being worn out from this process.

Delivery and Customer Service

A last criteria is good communication with the manufacturer and customer service if problems with the sensor should arise. Additionally, the delivery time will be considered for the sensor to arrive in ample time before conducting the experiments.

4.1.3 Estimated Sensor Requirements

Based on calculations and estimates the following criteria is provided to the various suppliers, along with a preliminary description of the planned experiments:

- Resolution $F_x/F_y \leq 0.2N$
- Measuring range $F_x/F_y \geq \pm 25N$
- Measuring range $F_z \geq \pm 50N$

A copy of the email to the suppliers is found in Appendix C together with their proposed sensor solutions.

4.1.4 Embedded Unit

Three individual measurements are needed for fully identifying the fluid coefficients of interest in this thesis: Forces in x and y direction, and torque around the z axis, see Figure 4.1. The three quantities of interest can be measured using a wide range

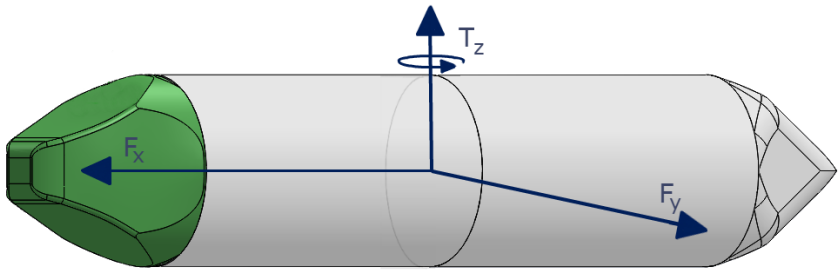

Figure 4.1: The three measurements needed for identifying the fluid coefficients.

of sensor equipment. Two possible approaches are using an individual sensor for each measurement, and one sensor for capturing all quantities. The first approach would require three individual sensor that each could be ordered according to the needed criteria needed for the experiments. This approach could provide measurement ranges perfectly suitable for the experiments, but it introduces uncertainty

in the form of having three sensors of possibly different quality, both in accuracy and build quality. In addition, different decoding requirements might result in synchronization problems when recording the measurements. Finally, three units will require more resources in form of required mounting space, manual assembly work, as well as the possibility of added cost.

A more elegant solution is to utilize a single unit providing all needed measurements, such as a six-axis force/torque sensor. A vast variety of these kind of sensors are commercially available for all kinds of applications. A single sensor eliminates the drawbacks in the previous paragraph, but might lead to the need of trade-offs in the sensor ranges as fewer options might be available. A general six-axis force/torque sensor has great potential for re-usability as forces and torques in all three axis direction are measured, making the more specialized approach in the previous paragraph possibly futile in other experiments. Using a single six-axis force/torque sensor seems reasonable for the experiments considered in this thesis.

4.1.5 ATI Mini40 IP68 6-axis Force/Torque Sensor

Based on the requirements of the sensor and discussions with the suppliers, the sensor Mini40 with IP68 rating from ATI Industrial Automation is chosen. It has a low-profile design ideal for several mounting scenarios, including mounting inside a snake module. The sensor is depicted in Figure 4.2. It is IP68 rated, for submersion in fresh water to a depth of 4m. The sensor is ordered with two calibration profiles, SI-40-2 and SI-80-2. Key properties for the two calibration profiles are listed in Table 4.1. The sensor has a very low noise distortion due to the use of silicon strain gauges that provides a stronger signal than conventional strain gauges, [3]. The sensor is delivered with a signal amplifier and a USB Data Acquisition (DAQ) interface for signal decoding. A stand-alone demo software is provided together with drivers for LabView.

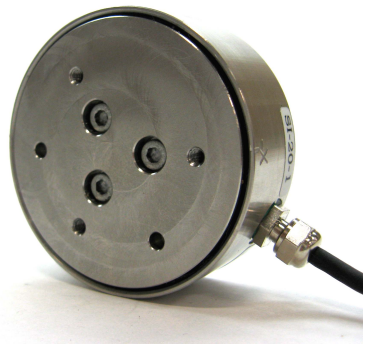

Figure 4.2: Mini40 IP68 six axis force and torque sensor.

Calibr.	F_x	F_y	F_z	T_x	T_y	T_z
SI-40-2	±40 N	±40 N	±120 N	±2 Nm	±2 Nm	±2 Nm
SI-80-2	±80 N	±80 N	±240 N	±4 Nm	±4 Nm	±4 Nm

Table 4.1: Measurement ranges of the ATI Mini40 sensor for two calibration profiles.

Connection and Signal Chain

The sensor is connected to a external power supply and signal amplifier (Figure 4.3(a)) by a 12-pin connector. A National Instruments USB DAQ card (Figure 4.3(b)) is connected to the power supply box by a 26-pin connector. The DAQ card converts the sensor signal from analog voltages to digital signals. It is connected to a computer via USB. The signal chain is illustrated in Figure 4.4.

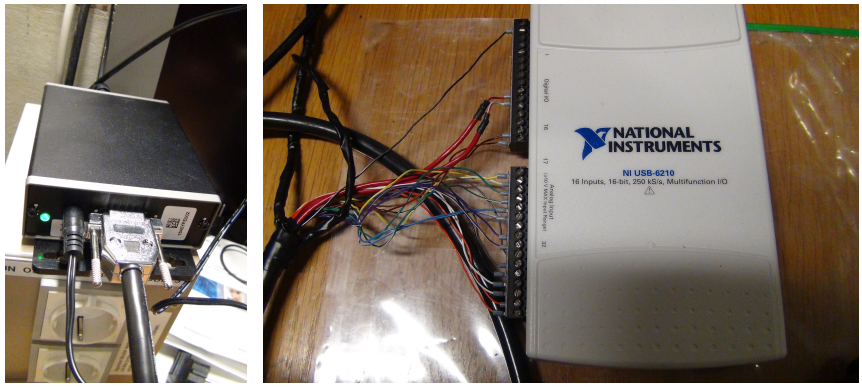

(a) Power supply (b) DAQ card

Figure 4.3: Power supply and computer interface for the sensor.

Software

A demo program from ATI Industrial Automation is used for monitoring, logging and changing the measurement settings. Relevant settings are calibration profile (see Table 4.1), measurement sampling frequency, averaging and biasing.

4.2 Module and Sensor Mounting

The total snake configurations are produced by mounting several 3D printed modules together. As there are limitations on the physical size of the printed objects, the link modules consists of two individual pieces that are put together. For an n-link snake configuration, the needed parts are listed in Table 4.2 and the assembly of the H2LT configuration is illustrated in Figure 4.5.

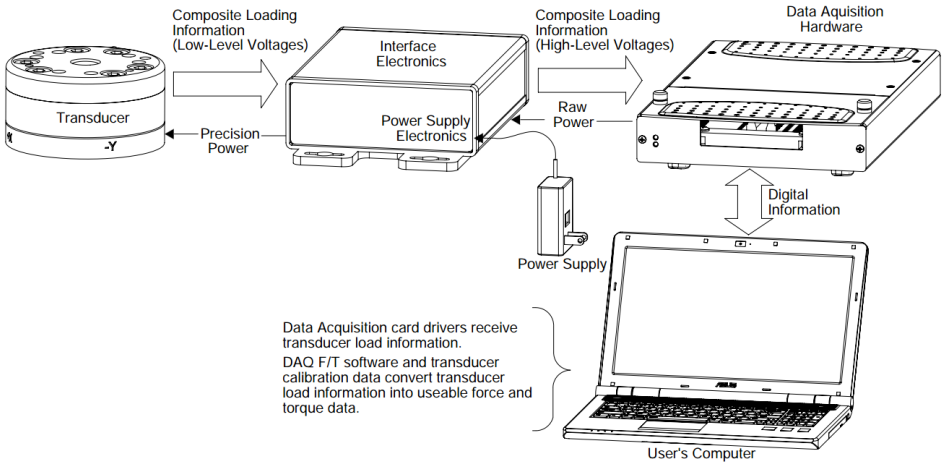

Figure 4.4: Signal chain for ATI mini40 sensor using a DAQ card, [2].

Module	Needed quantity
Head module	1
Tail module	1
Sensor module	1
Extension module	2
Link module	$2\times n$

Table 4.2: The parts needed for an n-link snake configuration

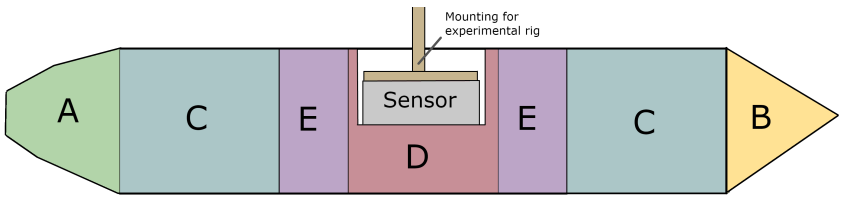

Figure 4.5: Assembled H2LT configuration. A: Head module, B: Tail module, C: Link modules, D: Sensor module, E: Extension modules.

4.2.1 Mounting of Sensor

The sensor is connected to the experimental rig by a stiff rod. A connector plate is mounted between the rod and the sensor to securely fasten the sensor. Figure 4.6 show the rod, connection plate and the sensor.

The measurement origin is located center at the bottom of the sensor. To avoid transforming the measured forces and torques, the sensor is mounted with the sensing origin at the snake module configuration CM. Using two link modules will

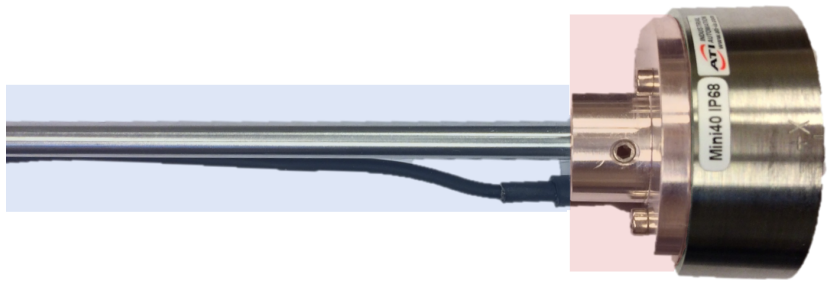

Figure 4.6: ATI Mini40 IP68 sensor mounted to the rod (blue) via the connector plate(red).

result in the sensor being mounted in the extension between the two modules. To avoid this a dedicated sensor module is printed, together with two extension modules that mounted together represents one link. A circular intrusion in the module allows the sensor to be mounted in the center without coming in contact with the surrounding walls, as this would lead to inaccurate measurement readings. When mounted correctly, the positive x and z axes points to the nose of the snake and downwards, respectively. Finally, a lid covers the opening while allowing the sensor cable and the mounting rod to exit without touching the lid. Figure 4.7 show the sensor mounted inside the module together with the head and tail modules.

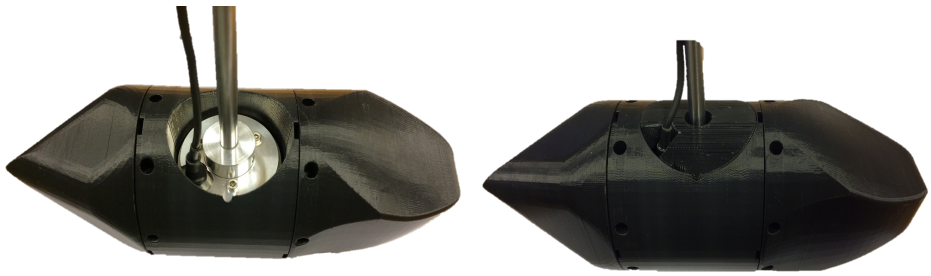

(a) Sensor mounted.

(b) Opening covered.

Figure 4.7: The sensor mounted in the middle module together with the tail and head modules.

4.2.2 Coating

The different modules of the snake are 3D printed, and as a result, they do not completely match the hydrodynamic properties of the 3D geometries used in the

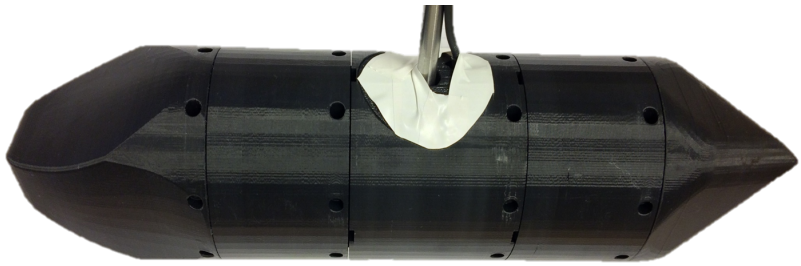

Figure 4.8: The H1LT configuration prior to coating. Not seen in this picture is the tape covering the numerous screw holes.

simulations. There are several factors causing these dissimilarities which each will directly effect the measurement results.

- The 3D printed surfaces are relatively coarse and porous compared to the ideal surfaces in the simulations. This is due to the 3D printing patterns and resolution, as well as the properties of the plastic material used. The coarse surface has a direct impact on the skin friction and thus increases drag forces.
- Because of the upper limit on the physical size of the objects that are to be 3D printed, each link module is produced by joining together two independently printed pieces by securing them together with bolts. The printed parts all have eight to sixteen holes for fully fastening the interconnected link modules together. Each of these holes contributes to increased drag.
- A small discrepancy in form of a small gap is observed at the interconnections of the modules.
- The lid covering the sensor in the sensor module has openings for the rod and cable. A second lid is located at the bottom of the same module covering the bolts mounting the sensor to the module. The openings and the extensions between the lids and the modules all contributes to hydrodynamic effects.

Figure 4.8 clearly show the coarse surface of the skin as well as the small air gaps between the different modules.

It is desirable to make the surface as smooth as possible to match the simulation parameters. The coarse surfaces can be sanded down, but the process might be time consuming and the results will not necessarily be sufficient. A solution is to cover the assembled snake modules in a latex skin. First, the holes for bolting the modules together are covered with tape, then the entire body is painted with Dragon Skin 10 Medium [44]. Dragon Skin is made by the company Smooth-on and is a silicone compound used for a variety of industrial applications as well as for movie special

effects. It has a service temperature from -21°C to +205°C. The compound is made out of two liquid parts A and B that are mixed together at a ratio of 1:1 by volume. Black pigment is added purely for aesthetic reasons.

The snake module is fastened securely with clamps to provide a stable working environment. When the two silicone parts are thoroughly mixed, a thin layer of the silicone compound is painted on the snake body with a brush. The silicone compound should be applied thick enough to cover the wanted surfaces, while still being thin enough to avoid the excess silicone to form droplet formations on the underside of the surface. The minimum cure time is five hours and the resulting surface is smooth when the compound has cured, see Figure 4.9. The skin sits tightly around the snake configuration while being easy to remove without it sticking to the surface of the snake.

Figure 4.9: Two different module configurations with Dragon Skin applied. From left to right: H1LT with cured skin, H2LT freshly painted.

Coating the snake in Dragon Skin highly improves the smoothness of the snake module. However, the opening where the rod and cable exits the snake are still open and will cause some additional drag effects. While the silicone compound is highly elastic, covering the openings requires contact with the rod which would lead to inaccurate measurement readings. In addition, the compound could drip down onto the sensor, possibly causing damage.

4.3 Passive Guided Rail Towing Tank for Drag Estimation

The first experimental approach is a passive guided rail towing rig. This setup utilizes a relatively small pool and a towing rig driven by simple weights. Based on available tools and resources, this setup is easily realizable. As the system has a passive input in the form of an applied weight, there is no need for developing electromechanical control systems. This does however produce a challenge in estimating velocities as there is no direct control or measurement of this. The validity of the experiments depends on the system reaching a steady-state velocity when measuring the forces acting on the snake. However, this setup is adapted to perform preliminary experiments as it is relatively simple and sufficient to obtain initial results for the drag coefficients. Figure 4.10 overviews this experimental approach.

4.3.1 Theory

Given a submerged body moving through water, if the force acting on the body can be measured, the relations in Equation 4.1 provides sufficient information to

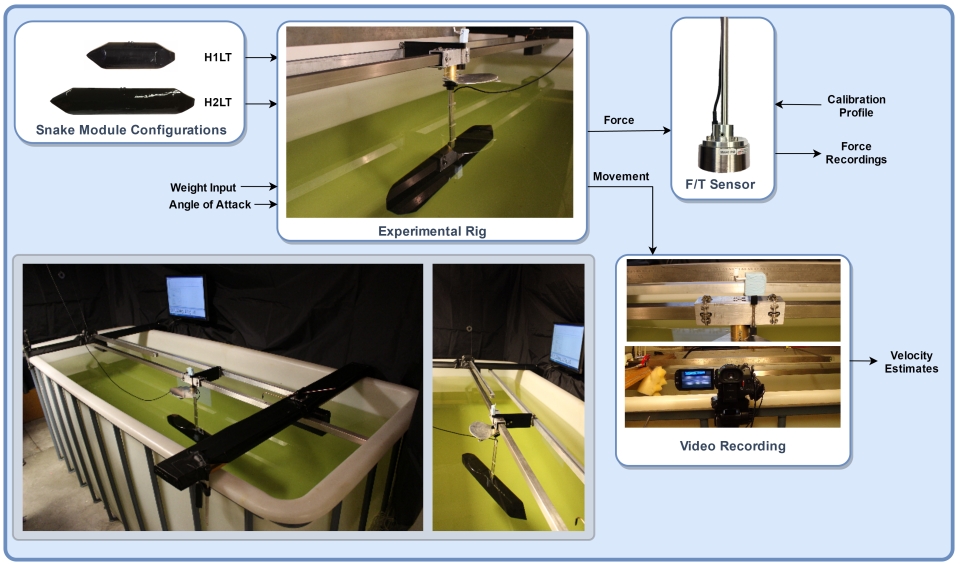

Figure 4.10: Overview of the passive guided Rail towing tank experimental approach.

identify the fluid coefficients:

$$f_m = f_D + f_A + ma, \tag{4.1}$$

where f_m are the measured forces, f_D drag forces, f_A added mass forces, m is the mass of the submerged object, and a is the acceleration. Assuming a constant velocity, the acceleration and added mass terms are zero and the above equation results in a direct measurement of the total drag forces. The drag term is equal to Equation 2.22 which contains both linear and nonlinear drag forces. Further, if the velocity and angle of attack of the submerged body can be controlled, and in addition, the force acting on the body can be measured in body x and y directions, then both drag coefficients, C_f and C_d can be determined experimentally.

4.3.2 Setup

The rig consists of a small pool with a rail mounted above the water. On the rail, a wagon is mounted which in turn is connected to weights that will drag the wagon across the pool when released. A rod extends from the wagon into the water where the snake module configuration is mounted. The wagon and snake configuration is constricted to movement along the global x axis, while the angle of attack can be adjusted by a mechanism on the wagon. Lastly, the force/torque sensor presented in Chapter 4.1, is mounted between the rod and the snake, at the snake module configuration CM. A sketch of the proposed rig is seen in Figure 4.11.

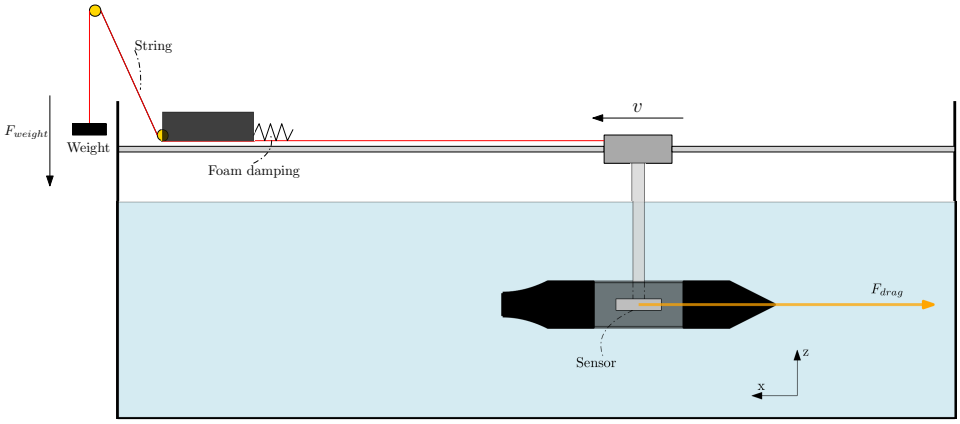

Figure 4.11: Overview over experimental setup for passive towing rig experiment.

Pool

The experimental rig is built around a plastic pool of dimensions 1.5 m × 0.9 m × 1 m (Length × Width × Height). A steel frame surrounding the pool reinforces the walls and bottom. The water height is 0.7 m before submerging the snake. The entire experimental setup centered around the pool is seen in Figure 4.12.

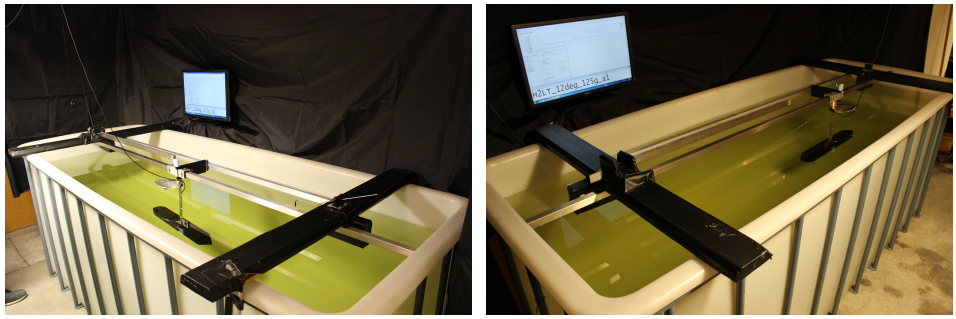

Figure 4.12: The pool for the passive guided rail towing tank experimental setup.

Rail and Towing Wagon

The main rail is a stainless steel square pipe running the entire inside length of the pool, parallel to the long walls. The rail acts as a guide for the movement of the towing wagon and snake and the global x axis runs parallel to this rail. It is mounted on each end of the pool on the underside of two solid wooden boards perpendicular to the rail, both which are securely fastened to the pool frame. The

two wooden boards are placed a small distance from the ends of the pool and acts as physical start and end-point barriers for the path of the wagon.

Preliminary tests showed the need of an additional rail in parallel with the main rail. Small disturbances in the water led to a tendency of swaying motion of the snake which again led to small rotational vibrations about the wagon x axis. The wagon is extended in y direction and mounted onto the second rail. This greatly reduces the unwanted transverse motion and makes the overall system stiffer and more robust. The preliminary test additionally revealed the stiffness of the rod to be insufficient. As the wagon is released, the length of the rod and the weight of the snake configuration combined with the abrupt motion of the wagon induces a spring behaviour in the rod which is observed as a sinusoidal motion in x direction in the sensor readings. Attaching a solid aluminum rectangular rod tightly to the main rod led to a noticeable decrease in the undesirable effect. These modifications does not affect the drag force measurements as the force sensor is attached inside the module.

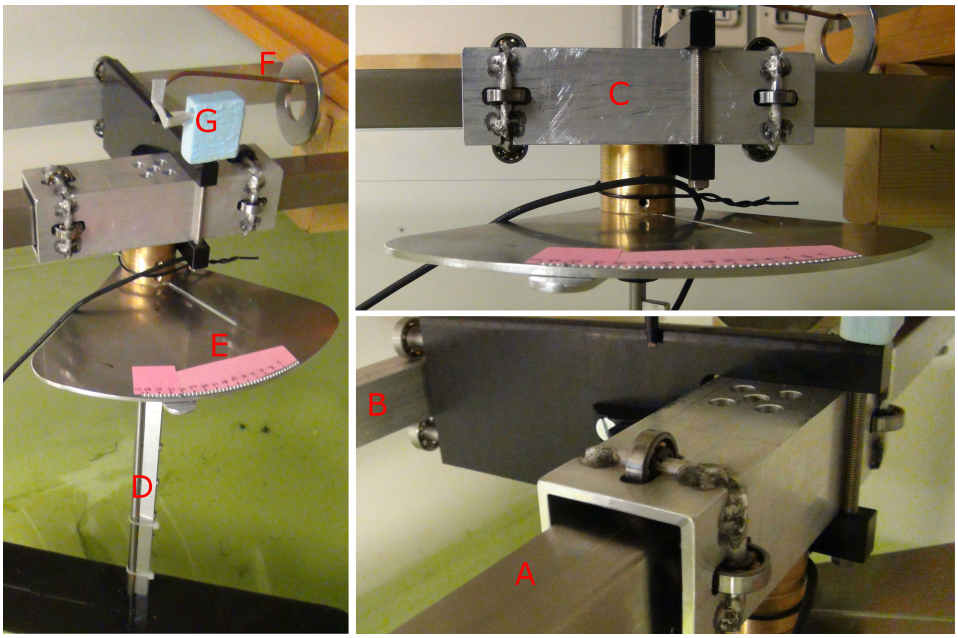

Figure 4.13: A: Main rail, B: Supporting rail, C: Wagon, D: Rod, E: Angle control, F: Release mechanism, G: Indicator for velocity estimations.

The wagon and rail is seen in Figure 4.13. The wagon is made up of a stainless steel square pipe surrounding the main rail. A total of 10 low-friction wheel bearings are allowing the wagon to move back and forth on the rails, where two of the wheels are on the upper and bottom faces of the supporting rail. The surfaces of the rail and the wheel bearings are lubricated to minimize friction and allowing for a smooth travel. The snake configuration is mounted to the wagon via a stainless steel rod extending from the bottom of the wagon down into the water. The rod is

securely fastened to the wagon with three hex screws to eliminate any wobbling or vibrations. The rod is 0.4 m long where of 0.25 m is located above the waterline.

The part of the wagon where the rod is mounted can be rotated by loosening two hex screws. This enables the snake configuration together with the rod to be rotated between the different runs. CNC drilled holes allow rotation at one-degree steps from 0 to 45 degrees. The rod has an arm extending perpendicular from the rod, with a small extrusion that fits into the holes to ensure the selected angle is maintained.

Snake Location

The snake configuration is placed in the middle of the pool with respect to the water depth and the long walls. As the size of the pool is relatively small, wakes, currents and waves will bounce off from the walls. Keeping the snake in the center can lead to some cancellation of these effects, compared to an off-center approach. The starting and stopping points for the snake travel is also placed at a certain distance from the end walls. This both for avoiding hydrodynamic wall effects as well as allowing for different snake configurations with different body lengths to start and stop at the same points. Figure 4.14 show the snake location.

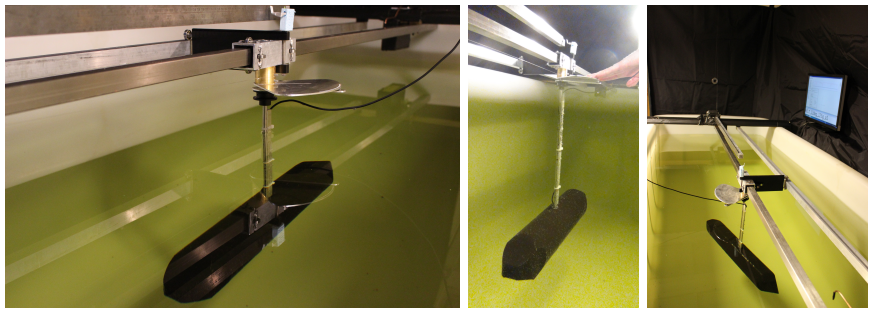

Figure 4.14: Snake configuration location in the pool.

Actuation

A weight pulling a string fastened to the wagon is the actuator input to the system. A plastic container holds the chosen weights applied to the system. The weight is suspended from the roof and is extended to the wagon via a string through two pulleys, allowing the weight to pull vertically while the motion of the wagon is horizontal. The string is a light-weight fishing line. The two wooden boards holding the guide rail acts as physical points for starting and stopping the wagon. When the wagon is pulled all the way back to its end position the wagon is held still by a simple release mechanism while the string is extended by the applied weight. The release mechanism ensures a consistent starting point for the wagon. When released, the string pulls the wagon and snake configuration along the rail towards

the end-point. At the end-point a piece of foam is installed to limit the impact when the run comes to an end. When at rest at the end position, the weight is still suspended, not touching the ground. The sensor cable is suspended from the roof above the experimental rig in such a way that the system is unaffected.

Different weights are used for producing the different scenarios discussed shortly. For each snake configuration, a lower limit is found by trial and error. Doing multiple test runs with different weights identifies the lowest possible weight producing a consistent and smooth ride. That is, the wagon should ride continuously without slowing down or show any signs of a stuttering movement. Finding the maximum weight is, again, done by adding weights to the setup and record the six measurement outputs from the sensor. The forces experienced by the sensor have the largest magnitude when the wagon impacts at the end of the rail. The upper weight limit is found when at least one of the recorded measurements is approaching the limit of the sensing range of the sensor, see Table 4.1. All weights between the lower and upper limit are thus applicable as inputs for the given snake configuration.

While being a simple and low-cost solution, a major drawback is the inability to precisely control the velocity of the system. Changing the amount of weight that is applied to the system is the only option for varying the velocity. In addition, different snake configurations and angles of attack leads to different velocities for the same applied weight force.

4.3.3 Experimental Scenarios

Two types of scenarios are run for each snake configuration. In the first scenario, the snake is traveling through the water tank with an angle of attack equal to zero, $\theta = 0$ degrees. This is done for a set of different weights as inputs. The possible selection of weights is limited as was discussed in the previous section. For the H1LT configuration, the applicable range of weights starts at 0.025 kg, with 0.025 kg increment up to the a maximum 0.2 kg. For the H1LT snake configuration, this results in eight different obtained velocities together with force measurements. In the second scenario, the angle of attack is increased by 3 degrees for each run. This is done for three different weights, totaling in 39 data points. The performed experimental scenarios are listed in Table 4.3. For the H2LT configuration, the possible weights are further limited due to the mass of the snake configuration. It requires a larger weight to achieve smooth movement, and releases more energy when stopping.

After each run, the wagon and snake configuration is pulled back to the start position and the weight and/or angle of attack is adjusted. As the pool is small, waves and currents are present after a run has been completed. It is necessary to wait for the water to calm down before conducting the next experimental run. For low weights and the angle of attack at zero, at least five minutes are required before conducting the next experiment. As larger weights and large angles leads to a more substantial amount of water being moved around, a longer waiting period is required. The waiting period was determined visually and by monitoring the sensor readings.

	H1LT		H2LT	
	Scenario 1	Scenario 2	Scenario 1	Scenario 2
Weight [kg]	**Angle** [deg]	**Angle** [deg]	**Angle** [deg]	**Angle** [deg]
0.025	0	–	–	–
0.050	0	3,6, . . . , 39	0	–
0.075	0	3,6, . . . , 39	0	3,6, . . . , 39
0.100	0	3,6, . . . , 39	0	3,6, . . . , 39
0.125	0	–	0	3,6, . . . , 39
0.150	0	–	0	–
0.175	0	–	–	–
0.200	0	–	–	–

Table 4.3: Experimental scenarios for passive guided rail towing tank.

4.3.4 Measurements

During each run, force measurements are logged continuously on a computer and saved as individual .csv files. The hardware and software, together with the signal chain is described in Chapter 4.1.5. For this experimental setup, the SI-40-2 calibration profile (Table 4.1) is used at a sampling frequency of 1000 Hz and averaging level of 50. Resulting in 20 measurement samples per second. A screenshot of the software is seen in Figure 4.15.

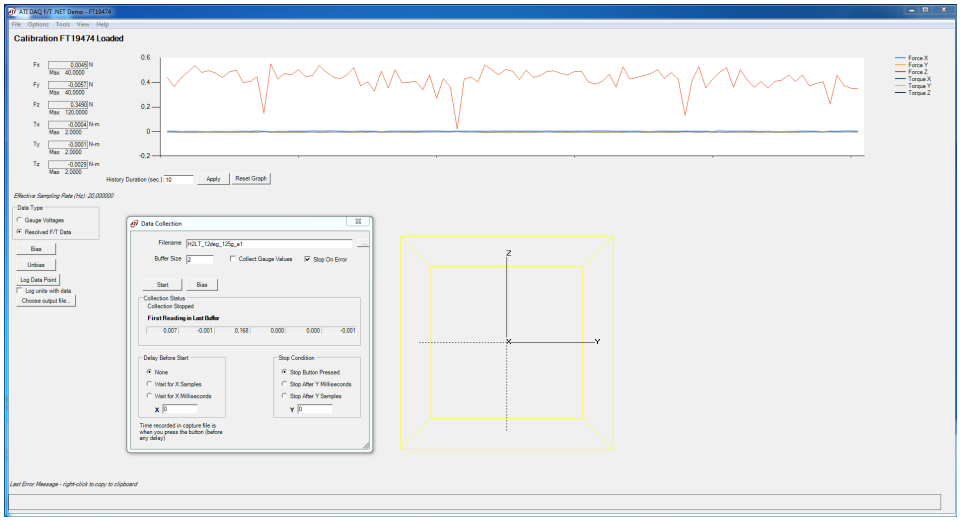

Figure 4.15: Screenshot from software used for sensor settings and measurement recordings.

4.3.5 Velocity Estimation

An important element of this experimental approach is estimation of snake velocities. Firstly, the estimated drag forces are dependent on the measured force and the velocity alone. Secondly, being able to eliminate added mass terms from the force measurements requires a constant velocity. In total, a precise velocity estimation is vital for producing correct results.

A video camera is mounted on a tripod overlooking the end of the rail as seen in Figure 4.16(a). The video camera is a Canon Legria HFG30. A 1 m long ruler is mounted parallel to the rail directly above the wagon, Figure 4.16(b). The camera frame captures 0.3-0.4 m of the wagon travel a few centimeters before the wagon reaches the stopping foam and is decelerated. A marker attached to the wagon clearly displays the position of the wagon relative to the ruler. From the recorded video of the runs, the velocities can be estimated as the amount of frames recorded by the camera each second, frame rate, is known. A monitor in the background displays an identification text for each run. As a result, each velocity estimate is matched to the appropriate force measurements.

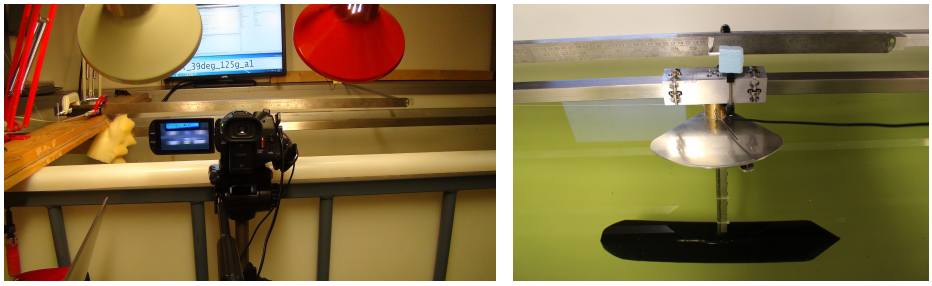

(a) Camera captures the movement of the wagon. (b) Ruler used for determining travel length.

Figure 4.16: Setup for velocity estimation.

Each run is recorded at a frame rate of 50 frames per second (fps), which is the maximum frame rate for this camera. Using the standard 24 fps frame rate would result in a higher uncertainty. This is due to the fact that a higher frame rate captures more information on the wagon position per second. Further, the shutter speed of the camera is set fairly fast at 1/2000 s to avoid blurry frames when the movement speed is high. The focal ratio is set to f/3.4. This enables the entire ruler section to be completely in focus, while still being able to read the run identification on the monitor in the background. The chosen shutter speed and focal ratio results in rather dark images where it is hard to read the ruler markings. This is solved by setting the camera light sensitivity to its maximum and mounting two lamps to further illuminate the needed areas. The combined camera settings above produces sharp and clear video frames for estimating the velocities.

For each recorded run, the recorded video is post-processed manually in order to obtain the velocity estimates. When the marker on the wagon has entered the video frame, the first position, p_1 is noted. Stepping through the video frame by

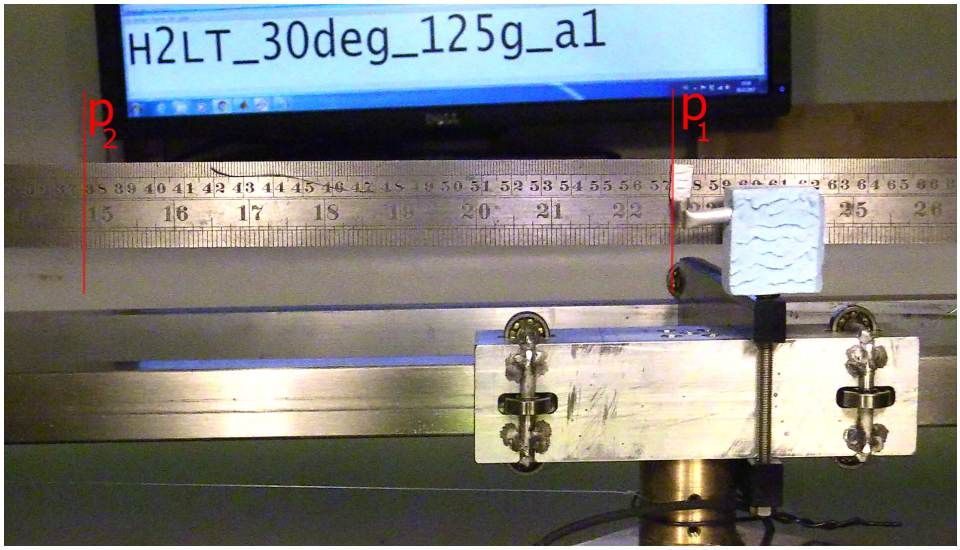

Figure 4.17: Still frame from velocity estimation video with examples of the start and finish points.

frame, the second position near the end of the frame, p_2 is noted together with the number of frames stepped through. Knowing the two positions and the number of frames in between, the following equation identifies the average velocity

$$v_{\text{mean}} = |p_1 - p_2| \frac{N_{\text{fps}}}{N_{\text{frames}}}. \tag{4.2}$$

, where v_{mean} is the average velocity, N_{fps} is the number of frames per second, and N_{frames} is the number of recorded frames.

A still frame from one of the recorded runs is seen in Figure 4.17. Note that there are some sources of error in this approach. Firstly, the experiments assumes a steady-state velocity is reached during the velocity estimations. However, the wagon might still be accelerating during the period of velocity estimation, and the calculation will be wrong. Secondly, the establishment of point p_1 and p_2 might be prone to error due to the camera perspective. The ruler has markings every 1 mm which is a fairly high resolution. However, when p_1 is to be determined at the right most part of the video frame, the apparent position from the camera is perceived as further to the right than its true position. The same applies for p_2. This effect is dependent on the distance from the wagon marker to the ruler. Therefore, the marker is position as close as possible to the ruler while still not coming in contact and possibly influencing the speed of the wagon. An additional solution is to position the two lamps in such a way that the shadow of the marker is the true position in the center of the two lit areas. Figure 4.18 illustrates the above concepts. Where p_1' is the apparent correct position, whereas p_1 is the actual position. The distance between the markers and the ruler is highly exaggerated to illustrate the concept.

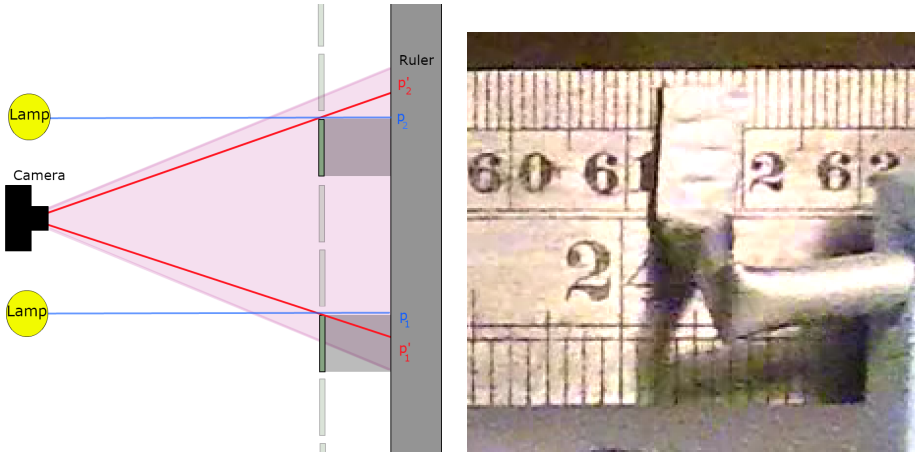

(a) Illustration of concept.

(b) The visible shadow indicating the true location.

Figure 4.18: Camera perspective error, where p_1 and p_2 in red are the position perceived by the camera, and p_1 and p_2 in blue are actual positions, seen as the small shadow in (b).

4.3.6 Measurement Recording and Post Processing

When a run is started, the force measurements are biased to remove any possible hysteresis and static measurements. The measurement recordings are started $t_n = 5$ seconds prior to the wagon being released from its starting point. In each trial, the initial measurements are averaged to identify the average steady-state noise experienced by the sensor, and is extracted from the final measurements. It is assumed this noise is constant throughout the run. When the wagon is released, the measurement recordings continue until the wagon has come to a full stop at the end.

Synchronization

As the velocity estimates and measurement recordings are not synchronized, a method is developed to match the correct measurement section with a given velocity. A constant velocity is assumed in the travel range of the velocity estimation. The distance from the point of deceleration to the final position of the velocity estimation, p_2, is known. As a result, the duration of which the velocity is averaged is known together with the duration of travel before impact. When analysing the recorded measurements, the point of deceleration is easily identified through peaks in the force measurements when the wagon abruptly stops. The time of the impact is denoted t_i. Using this information together with the sampling rate of the sensor measurements, one can extract the correct section of the measurements to match with the average velocity. As a result, the amount of measurement points for this period varies with the speed of the wagon.

For K number of runs at a given configuration of weight and angle, the average force measurement, $\bar{f}_{avg}$, is given as

$$\bar{f}_{avg} = \frac{1}{K}\sum_{k=1}^{K} \bar{f}_{meas,k} - \bar{f}_{noise,k}, \tag{4.3}$$

where

$$\bar{f}_{meas,k} = \frac{1}{N_{m,k}} \sum_{m=N_{k,1}}^{N_{k,2}} f_k(m), \tag{4.4}$$

$$\bar{f}_{noise,k} = \frac{1}{N_n} \sum_{m=1}^{N_n} f_k(m), \tag{4.5}$$

where k is the run number and $\bar{f}_{meas,k}$ is the average of the measurement period corresponding to the section of the averaged velocity in run k. Whereas $\bar{f}_{noise,k}$ is the average of the measurements prior to the start of run k, and

$$N_{k,2} = t_{k,2}\frac{f_s}{avg}, \tag{4.6a}$$

$$N_{k,1} = t_{k,1}\frac{f_s}{avg}, \tag{4.6b}$$

$$N_{m,k} = N_{k,2} - N_{k,1}, \tag{4.6c}$$

$$N_n = t_n\frac{f_s}{avg}, \tag{4.6d}$$

are the number of measurement samples for run 1, run 2, prior to release of run k and noise, respectively. Further, f_s is the sample rate, avg is the averaging number for the measurements, $t_{k,1}$ and $t_{k,2}$ are the measurement start and stop times. The noise sampling time is constant, $t_n = 5$s. Whereas the sampling periods for the measurements are dependent on the average velocity of the system.

$$t_{k,2} = t_i - \frac{p_2 - 0.275\text{ m}}{\bar{v}_k}, \tag{4.7a}$$

$$t_{k,1} = t_{k,2} - \frac{p_1 - p_2}{\bar{v}_k}, \tag{4.7b}$$

where t_i is the time of impact. An example of the recorded force in x direction for a run is seen in Figure 4.19, where $\bar{f}_{noise,k}$ is recorded in the period up to t_n. Shortly after, the wagon is released and the period of velocity averaging and valid measurements is from $t_{k,1}$ to $t_{k,2}$. For the same example, the resulting measurements and averages are shown in Figure 4.20.

4.3.7 Validation of Measurements and Velocity Estimations

All experimental runs for the H1LT configuration at zero degree angle of attack are conducted six times at different orders. First, each weight configuration is run three times in a row before incrementing the weight. Then the runs are conducted again

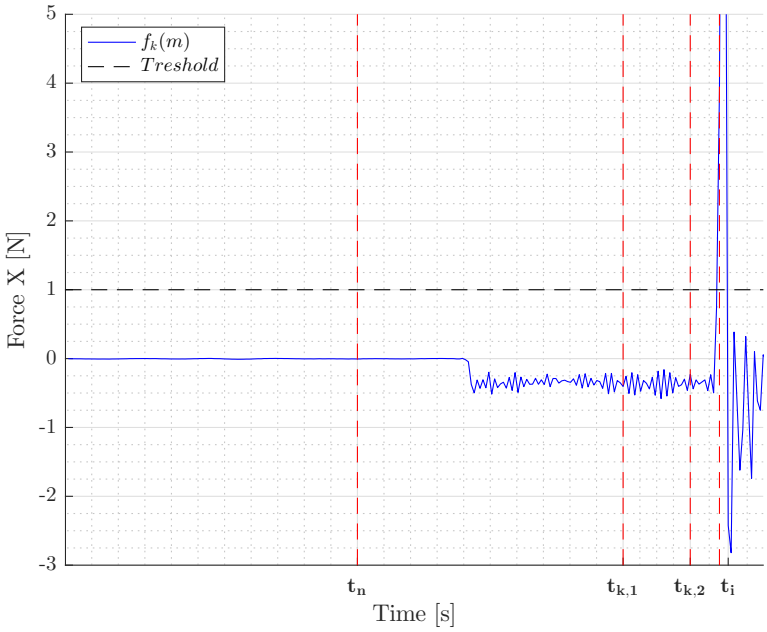

Figure 4.19: Time definitions for synchronization of measurements to velocity.

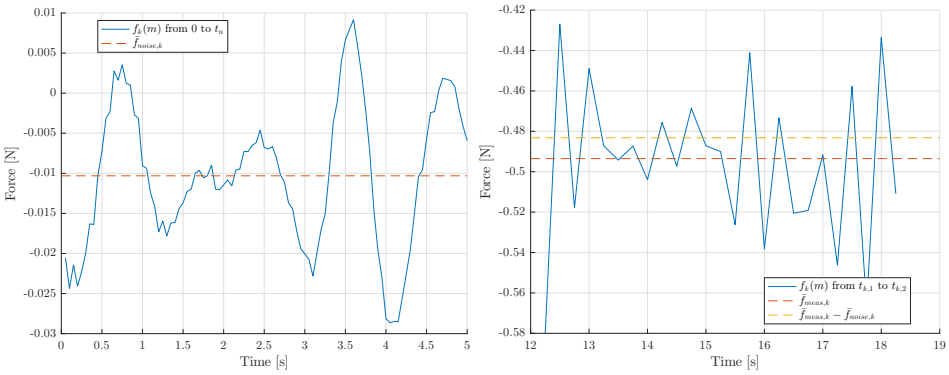

(a) Noise and averaged noise.

(b) Force, averaged force, and average force with noise accounted for.

Figure 4.20: Recorded and averaged measurements.

for each weight once, before incrementing to the maximum weight. This is done three times as well, resulting in six individual runs for each weight configuration. This is done to validate the force measurements and velocity estimations, and investigate the repeatability of the experimental trials.

Both the force measurements and the velocity estimations were found to coincide sufficiently for each separate run. Table 4.3.7 overviews the calculated variances for the velocity estimations and force measurements in x direction.

Weight [kg]	**Velocity**	**Force**
0.025	0.0103%	0.1075%
0.050	0.0027%	0.0402%
0.075	0.0004%	0.0236%
0.100	0.0005%	0.0165%
0.125	0.0014%	0.0124%
0.150	0.0011%	0.0100%
0.175	0.0038%	0.0084%
0.200	0.0031%	0.0073%

Table 4.4: Variance [%] of velocity estimations and force measurements for different weight inputs.

Figure 4.21 show the force measurements in x direction for all weight inputs on the H1LT snake configuration compared to the average.

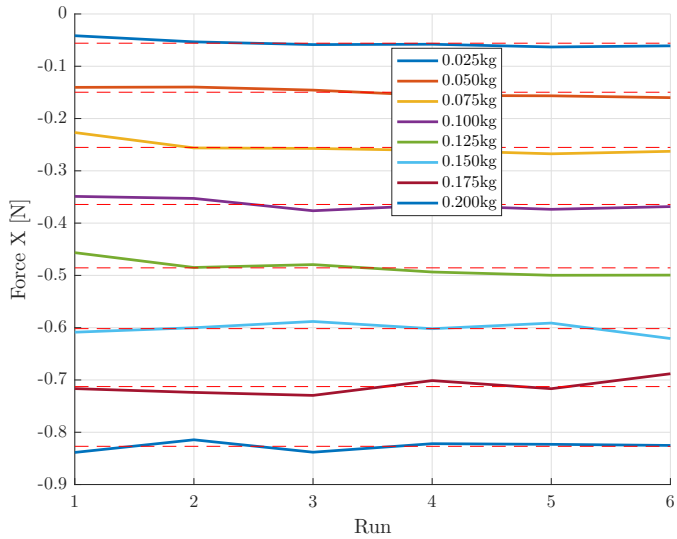

Figure 4.21: Force measurement validation for H1LT configuration. The dashed lines are the average for each weight.

As the variance in both velocity and force is small, it is concluded that the velocity estimations and force measurements are sufficiently accurate. As a result, the remaining experiments are run once for each case.

4.3.8 Limitations

Due to the size of the pool, the experiments are limited to the H1LT and H2LT configurations. Extending the snake configuration with additional links results in the snake coming too close to the edges of the pool. The amount of data points for the first scenario are substantially fewer than for the simulation approach in Chapter 3.1.3, where 50 data points are gathered for each configuration when the angle of attack is zero. Whereas for the angled simulation scenario, 124 data points are obtained, compared to 39 experimentally. Still, sufficient data points are gathered for comparison to the simulations. A weight incrementation lower than 0.025 kg is possible and will result in more data. However, due to the waiting period between each run the required time for the experiments is large. As a limited time is available for the experiments, limitations has to be made. Still, a total of 141 recorded runs are conducted.

4.4 Circulation Tank for Drag and Added Mass Estimations

The circulation tank experiments are an extension to the experiment in Chapter 4.3. The snake configurations are submerged in a circulation tank with an user defined laminar fluid flow. Similar to the passive towing tank experiment, force measurements are recorded. However, now the fluid velocity is constant and known. Further, by moving the submerged snake configuration in a sinusoidal motion like a pendulum perpendicular to the water flow, the added mass coefficient in y direction can be identified.

4.4.1 Theory

Fluid Drag

Equation 4.1 and the assumptions in Chapter 4.3.1 are still valid.

Added Mass

Given that the drag coefficients are identified, Equation 4.1 can be exploited to extract the added mass coefficients. The method requires the acceleration of the snake configuration to be known. An assumption made for the mathematical model in Chapter 2 is that the underwater snake robot is neutrally buoyant. This is not the case for the conducted experiments. While this is of no importance for the drag related experiments, this can have a huge impact on the added mass experiments. Assuming the fully submerged snake module configuration has positive buoyancy, the following equation can be used to extract the added mass forces of the configuration.

$$f_m = ma + f_D + f_A + f_B, \tag{4.8}$$

where f_B is the buoyancy force.

4.4.2 Overview of Experiments

Figure 4.22 overviews the circulation tank experiments for drag and added mass. The snake module configuration is mounted submerged in a test section of a circulation tank. For identification of fluid drag, the angle of attack of the snake configuration can be chosen between 0 and 90 degrees. For added mass identification, the angle of attack is set at $\theta = 0$ degrees, while a servo motor moves the snake in a sinusoidal motion, like a pendulum, perpendicular to the flow. The body velocity and acceleration is extracted from the given input and measured servo motor angle. A laminar fluid flow enters the test section at a user-defined velocity. The six axis Force/Torque sensor presented in Chapter 4.1 outputs the forces acting on the snake by the fluid flow. The velocity of the fluid is measured accurately using a Laser Doppler Velocimetry (LDV) setup. Drag experiments are conducted with a variety of flow velocities, while the flow is limited for the added mass experiments.

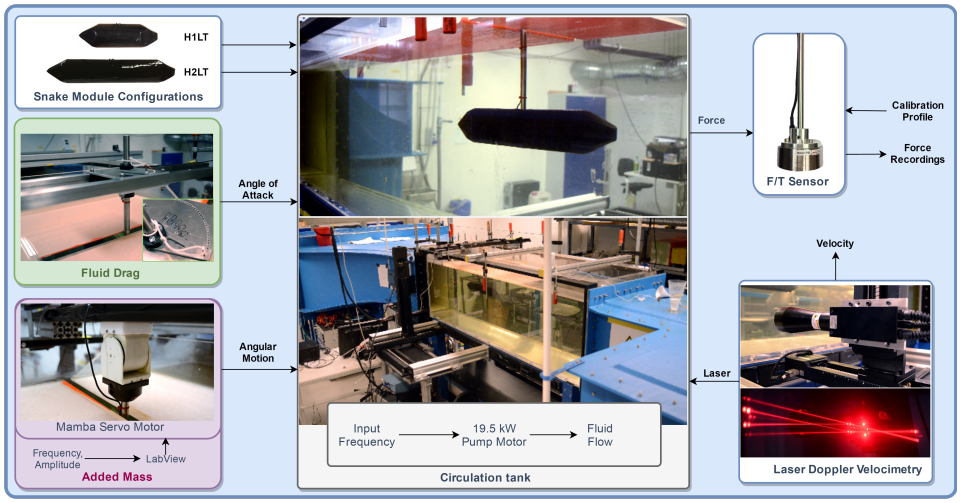

Figure 4.22: Overview of the circulation tank experimental approaches.

4.4.3 Setup

Circulation Tank

A circulation tank is the main component of the experimental approach. A typical application for a circulation tank is tests on static models in moving water. These can include scaled ship models, marine structures, turbines and more. The circulation tank at the Department of Marine Technology (NTNU) at Tyholt [43], has a laminar fluid flow (Turbulence level of 1% of free stream velocity), and the flow can be controlled exactly, with speeds ranging from 0.03 to 1 m/s. An option for varying flow speeds are also present. The circulation tank is powered by a 18.5 kW pump motor. The dimensions of the circulation tank is 9.1 m $\times$ 3 m $\times$ 2.11

m (Length × Width × Height), while the test section is 2.5 m × 0.61 m × 0.61 m (Length × Width × Height). The test section is encapsulated in 0.026 m thick plexiglass walls. The top plexiglass consists of two individual parts which can be removed for access to the test section. When mounted, a 0.028 m wide gap allows the test object to be placed inside the test section by a rod extending to the outside.

Snake Location

The snake configuration is placed centered in the y-z plane. In x direction, the snake CM is placed 0.69 m from the flow inlet. Figure 4.23 show the H2LT configuration mounted in the test section. Note that the first top plexiglass is not present in this photo.

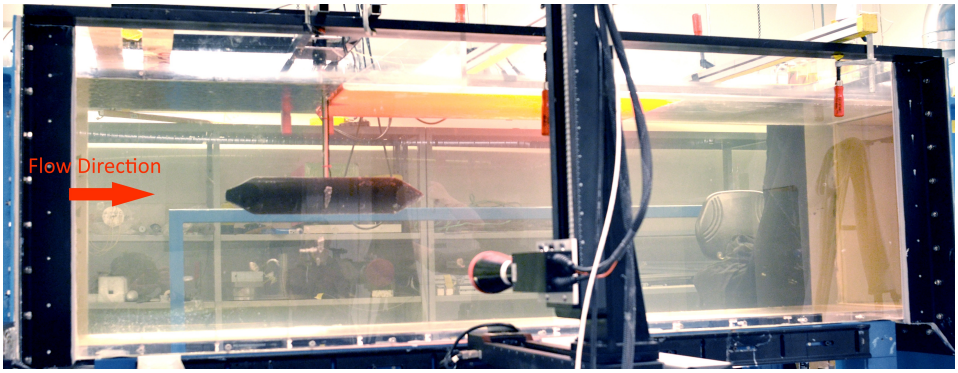

Figure 4.23: Snake configuration placement in circulation tank.

Setup for Drag Coefficients

The setup used in the circulation tank for estimating the drag coefficients is an improved version of the setup for the passive guided rail towing tank. The setup is more rigid as the only moving part in this setup is the angle of attack control. Two stainless steel square pipes mounted across the test section of the tank secures a solid platform for mounting the snake module. Two stainless steel plates are mounted on each side of the square pipes. A stainless steel pipe extending down to the sensor and snake module configuration goes through the plates and does not allow for movement in z direction. The diameter of the pipe is 0.02 m, further stiffening the system compared to the previous experimental setup. The top steel plate is perforated at 3 degree intervals, allowing an angle of attack from 0 to 90 degrees. The chosen angle of attack is locked with a pin. In addition the rod and connections on the plate and the sensor have extrusions fitted, such that the angle between them is constant. An illustration of the setup is seen in Figure 4.24.

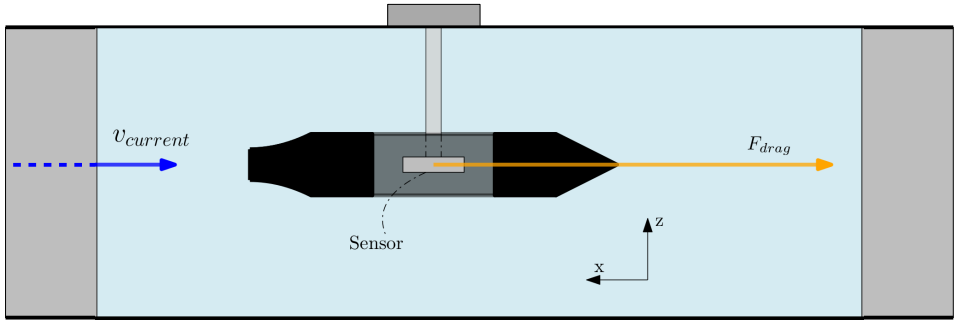

Figure 4.24: Illustration of experimental setup in the circulation tank for drag forces.

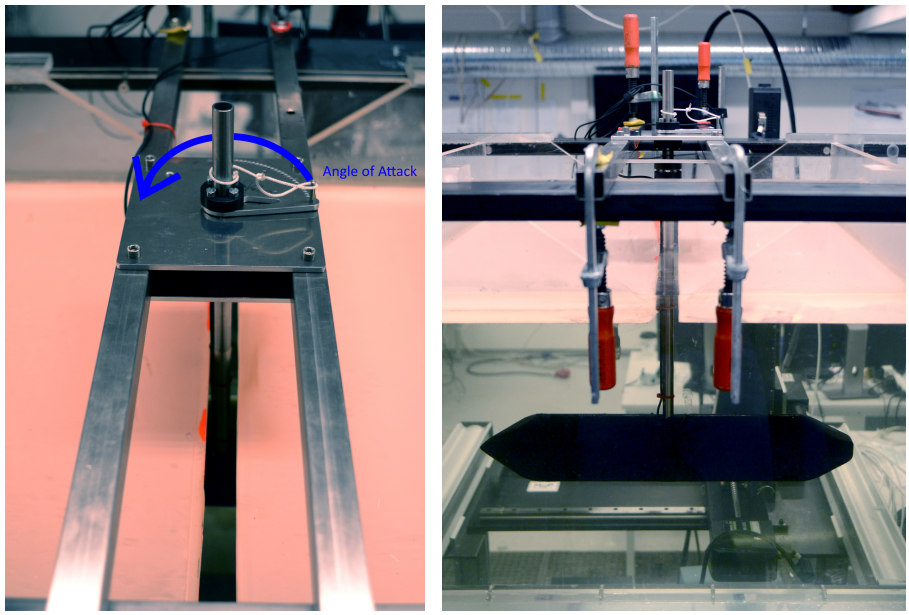

(a) Top view. (b) Side view.

Figure 4.25: Overview of the final experimental setup in the circulation tank for identification of drag coefficients.

Setup for Added Mass Coefficients

For the added mass experiments, the modules requires an acceleration. This is achieved by utilizing a servo motor from the snake robot Mamba. An actual functioning joint module from Mamba containing the servo motor, electronics and an angular positioning sensor is used for this purpose. The link is mounted on a beam across the test section of the circulation tank. An adapter plate is used to mount the steel pipe to the joint. The snake configuration is fixed at an angle of attack

equal to zero, $\theta = 0$ degrees. When moving the joint, the snake modules moves angular in the global y-z plane, which translates to a movement in body y direction only. Figure 4.26(a) illustrates the concept. The servo motor is controlled from a national Instruments LabView program. The commanded angular position is ϕ and the amplitude of the motion is α. The radius of the angular motion of the snake configuration CM is $r = 0.476$ m. The final setup is seen in Figure 4.26(b).

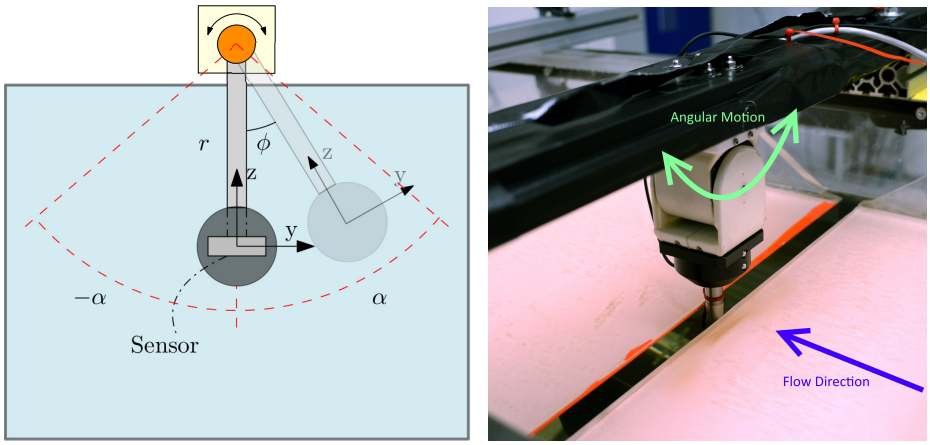

(a) (b)

Figure 4.26: Overview of experimental setup in the circulation tank for identification of added mass coefficients.

4.4.4 Servo Motor Control and Acceleration Estimation

The servo motor is controlled by a LabView program used in controlling the underwater snake robot Mamba. The LabView program is modified to record measurements from the 6-axis Force/Torque sensor mounted inside the snake module configuration. Appendix B.1.2 contains the LabView program, and a brief user guide can be found in Appendix B.1.3. The angular motion is given by the control signal

$$\phi_{ref} = \alpha \sin(\omega t), \tag{4.9}$$

where ω is the frequency and α is the amplitude. The maximum value of α is dependent on the minimum distance the snake configuration should have from the walls to avoid hydrodynamic wall-effects.

4.4.5 Velocity Measurements and Acceleration Estimations

The flow velocity in the test section of the circulation tank is measured by a magnetic flow meter, located near the start of the test section. Small modifications to the test section of the flow tank have been made since the original installation.

Figure 4.27: Power box and LabView program used for controlling the servo motor.

As a result, the flow speed measurements from the flow meter may not be accurate. To sufficiently determine the flow speed, a LDV rig has been utilized. In summary, the LDV concept works in the following way. A laser beam is split in two polarized, coherent beams which are focused at a single point inside the test section. The focal point is located in the beginning of the test section, in front of the snake module configuration. In addition to naturally occurring particles, reflective particles are added to the fluid. When a particle passes the focal point of the laser beams, the scattered light is collected by receiving optics and focused on a photo detector. The resulting light intensity frequency is related to the velocity of the particles, and the flow velocity can be found. The LDV approach is highly accurate, non-intrusive and needs no calibration. A limitation is that the velocity is measured at a single point. However, the inlet flow at the test section is highly laminar, and knowing the velocity at the focal point should be sufficient.

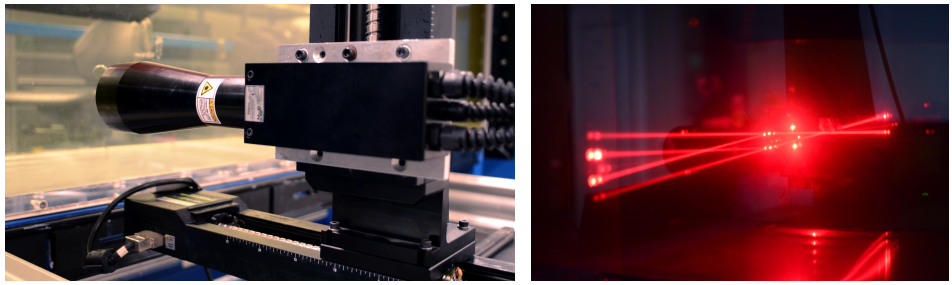

(a) Laser transmitter/receiver. (b) Laser beams.

Figure 4.28: Laser Doppler Velocimetry setup.

When comparing the velocities obtained from the LDV system to the magnetic flow meter, the difference is small. The differences in measured velocity can be seen in Table 5.3. For each velocity, the LDV system is set to measure the velocity continuously until around 100 particle velocities are accepted and the average velocity

is returned. The error between the measurements are very low.

Acceleration Estimations for Added Mass

As this setup does not contain an accelerometer, the acceleration and velocity of the snake configuration has to be determined in a different way. By differentiating the command signal, angular velocity and angular acceleration is obtained. The lag between the measured position ϕ and the command signal ϕ_{ref} is used to determine the phase shift, Φ. Additionally, the measured amplitude is larger than the commanded due to overshooting. The difference is adjusted for by adding a term to the amplitude. The corrected signal, ϕ_{ref}, can be differentiated to find the angular velocity and acceleration coinciding with the measured angle. Figure 4.29(a) show the command signal together with the measured angle and corrected signal. Figure 4.29(b) show the resulting estimated angular acceleration compared to the numerically differentiated angular acceleration based on the measured angle. The angular acceleration estimate clearly follows the numerically differentiated angular acceleration, completely removed of noise.

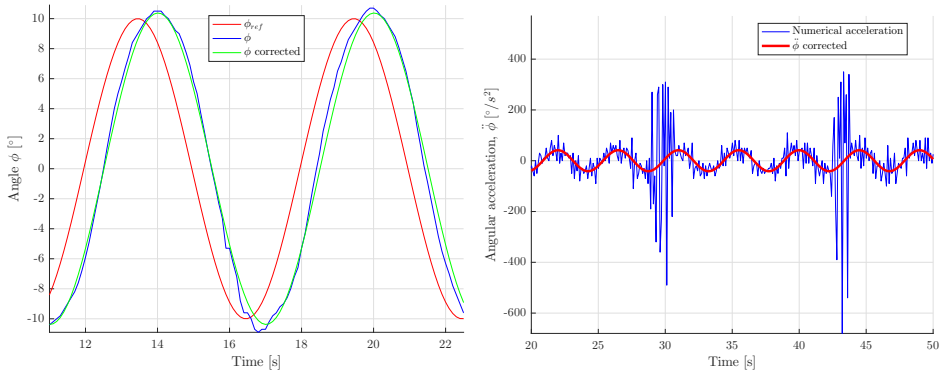

(a) Comparison of reference angle, measured angle and corrected signal.

(b) Numerically differentiated angular acceleration compared to corrected angular acceleration.

Figure 4.29: Correction of angular position and accelleration.

Body y velocity and acceleration is found by multiplying with the radius, r. The resulting velocity and acceleration estimates of the snake module configuration is given by

$$\hat{v}_y = r\left(\alpha + \delta\right)\omega \sin\left(\omega t + \Phi\right), \tag{4.10}$$

$$\hat{a}_y = -r\left(\alpha + \delta\right)\omega^2 \cos\left(\omega t + \Phi\right), \tag{4.11}$$

where δ and Φ are the amplitude and phase shift correction terms, respectively, and $\hat{v}_y$,
$hata_y$ are the estimated velocities and accelerations.

4.4.6 Experimental Scenarios

The experimental scenarios conducted in the circulation tank are run for two snake module configurations, H1LT and H2LT.

Drag Coefficients

The experimental scenarios for identification of drag coefficients are chosen to match the simulation scenarios. The accurate control and measurement of the fluid flow velocity makes this possible. Table 4.5 overviews the conducted experiments. Each of the experimental cases are conducted twice. Case 1 considers an angle of attack equal to zero, $\theta = 0$ degrees, at 10 different velocities. The experiments are run once with increasing flow velocity, and a second time with decreasing velocity. Case 2-5 are run at four velocities with a varying angle of attack, ranging from 0 to 90 degrees at 3 degree intervals. Again, each case is run once with increasing θ and again with decreasing θ. For all cases, measurements capturing any static noise are captured prior and subsequent to each of the twin case runs. After the flow velocity or angle of attack is changed, the force recordings are started when the any possible force fluctuations have settled and the flow has reach its steady state. The force measurements for each run is then recorded for 10 seconds.

For body configurations H1LT and H2LT					
	Velocity [m/s]		**Angle,** θ [deg]		No. of
	Range	step size	Range	Step size	runs
Case 1	[0.1 to 1]	0.1	0	—	10 × 2
Case 2	0.1	—	[0 to 90]	3	31× 2
Case 3	0.2	—	[0 to 90]	3	31× 2
Case 4	0.3	—	[0 to 90]	3	31× 2
Case 5	0.4	—	[0 to 90]	3	31× 2
Simulation scenarios per configuration: 134× 2					
Total number of experimental runs: 536					

Table 4.5: Scenarios for obtaining drag coefficients in the circulation tank experiments. For H1LT and H2LT snake module configurations.

Added Mass

Added mass experiments are conducted with body x axis parallel to the fluid flow in the circulation tank, $\theta = 0$ degrees. The body configurations are moved in a sinusoidal motion perpendicular to the flow, illustrated in Figure 4.26(a). The experiments are run for a set of different amplitudes, α, and frequencies, ω.

The largest value of α is dependent on the width of the test section, movement radius, and the radius of the snake module. Additionally, requiring that the snake configuration is not too close to the walls, the maximum amplitude is found to be $\alpha \approx 20$ degrees. As the snake configuration is moved towards the walls, displaced fluid will push back onto the snake, causing inaccurate force measurements. Ideally, the experiments should be conducted in a larger pool where there is no possible

issues with such wall effects. A solution is to remove the displaced fluid by applying a fluid flow in the circulation tank. The width of the tank limits the experiments to identifying added mass in y direction only. For long slender bodies, this can safely be assumed zero. The presence of a fluid flow in x direction should therefore have little impact on the behaviour of the snake configuration.

The lowest possible frequency, ω is found by visual inspection. For $\omega < 60$ deg/s, a jerky and inconsistent motion is clearly observed, resulting in the actual motion differing in a large degree from the commanded motion. The largest frequency is found by monitoring the temperature of the servo motor for a large amplitude at increasing frequencies. Too high temperatures indicates that the servo motor might be overloaded and the commanded motion will not be possible to follow. Additionally, the high load can cause the servo motor to malfunction.

The experimental cases are presented in Table 4.6. For each combination of amplitude and frequency, the experiments are run for 60 seconds. Additionally, 5 seconds of noise measurements are recorded prior and subsequent to the sinusoidal motion.

For body configurations H1LT and H2LT				
	α [deg]	ω [deg/s]	Fluid flow [m/s]	No. of runs
Case 1	10	60, 70, 80	0.2	3
Case 2	15	60, 70, 80	0.2	3
Case 3	20	60, 70, 80	0.2	3
Simulation scenarios per configuration: 9				
Total number of experimental runs: 18				

Table 4.6: Scenarios for obtaining added mass coefficient in the circulation tank experiments. For H1LT and H2LT snake module configurations.

4.4.7 Measurement Post Processing

Drag

For each of the two twin runs, the average of the noise recordings prior and subsequent to the experiments are subtracted. This gives four force recordings that have been compensated for any static noise that might be present. The average of the four compensated force measurements are the final obtained force. For two twin runs, 1 and 2, the final force is found by

$$\bar{f}_m = \frac{1}{4}\sum_{i=1}^{2} f_{m,i} - f_{\text{noise},i}^{\text{pre}} + f_{m,i} - f_{\text{noise},i}^{\text{post}}, \tag{4.12}$$

where $\bar{f}_m$ is the resulting force, $f_{m,i}$ is the measured noise for run i, while $f_{\text{noise},i}^{\text{pre}}$ and $f_{\text{noise},i}^{\text{post}}$ are the noise measurements prior and subsequent to run i. Figure 4.30 show examples of noise measurements, compensated force measurements and the final force.

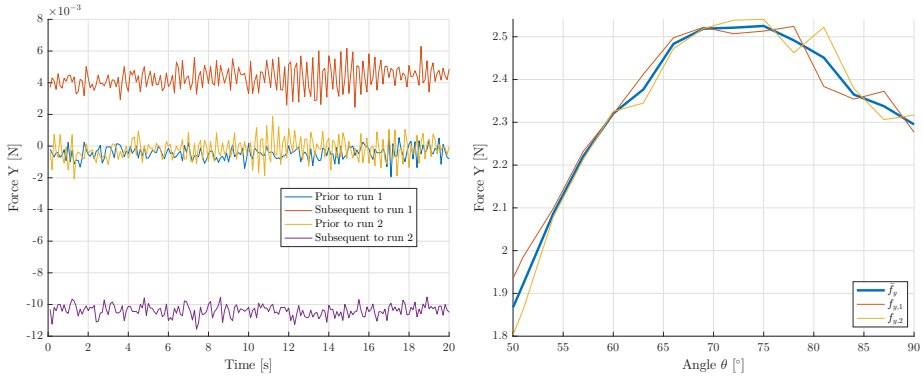

(a) Noise measurements.

(b) The two force measurements and the final force.

Figure 4.30: Example of resulting force measurement based on two runs and compensated for noise.

Added Mass

The measured forces can be decomposed to several terms which has to be determined individually. The added mass forces can be extracted from this.

$$f_A = f_m - ma - f_D - f_B. \tag{4.13}$$

The measured force is filtered to remove some unwanted noise. This is seen in Figure 4.31.

Acceleration estimations are explained previously. The mass of the snake is found by measuring the complete setup with the snake module configurations, sensor, motor and cables. As water enters the configuration, this becomes part of the mass of the system. By subtracting the weight of the setup without the snake module configuration, the mass of the two snake module configurations are obtained: $m_{\text{H1LT}} = 1.43$ kg, $m_{\text{H2LT}} = 2.395$ kg. The drag forces are based directly on the coefficients obtained from the drag experiment. The buoyancy force is found by biasing the sensor data at $\phi = 0$ degrees, where the buoyancy component of the measured force in y direction, f_{m_y}, is zero. For four different values of ϕ, f_{m_y} is measured and the buoyancy force, B, is found from the relation

$$B = \frac{f_{m_y}}{\sin(\phi)}. \tag{4.14}$$

The measurements are done twice for each combination of snake module configuration and ϕ. Table 4.7 summarizes the obtained buoyancy forces. From Equation 4.14, the buoyancy force in y direction as a function of the angle ϕ is

$$f_B = B\sin(\phi). \tag{4.15}$$

Removing all of the above terms from Equation 4.13 the forces caused by the added mass is found. Figure 4.32 show the different force components obtained from the added mass experiments.

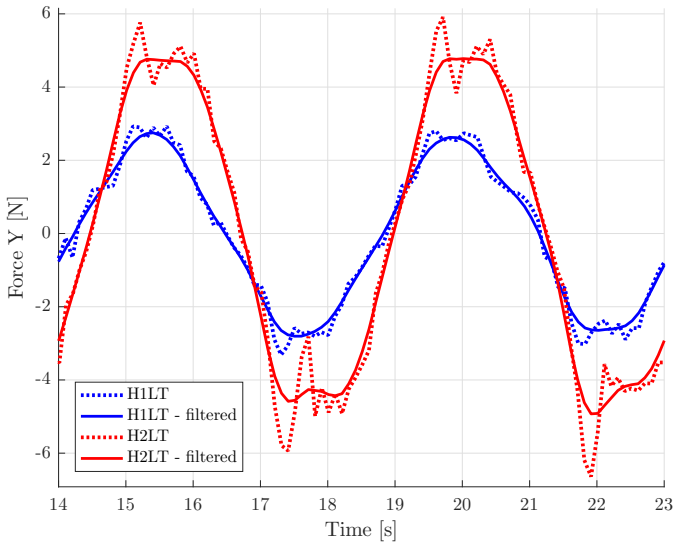

Figure 4.31: Filtered and unfiltered force measurements for added mass experiments. With $\alpha = 20$ and $\omega = 80$.

	H1LT		**H2LT**	
	Buoyancy force, B [N]			
ϕ	Run 1	Run2	Run 1	Run 2
5	3.8210	3.8158	8.2147	8.7697
10	3.8100	3.9062	8.3242	8.6104
15	3.8379	3.8569	8.2700	8.4756
20	3.8483	3.8699	8.2674	8.3954
Mean force	$B = 3.8457$		$B = 8.4159$	

Table 4.7: Obtained buoyancy force for H1LT and H2LT body configurations.

4.4.8 Limitations

The size of the test section of the circulation tank limits the conducted experiments to the H1LT and H2LT snake configurations only. The width of the test section is less than the length of the H3LT configuration, highly limiting the number of possible experiments with a varying θ. For small θ, the test section can accommodate the H3LT configuration. However, this could lead to inaccurate LDV velocity measurements. There are limitations in the placement of the LDV system which for the H3LT configuration will lead to the laser focal point being placed at a location where the flow has been altered due to the presence of the snake module configuration.

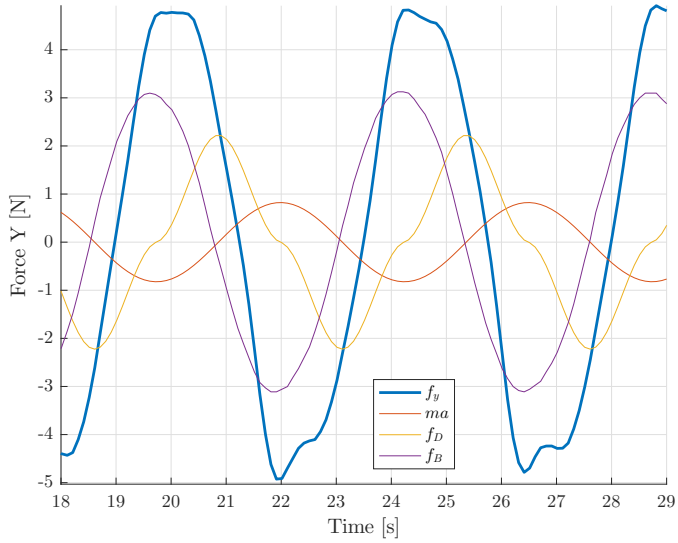

Figure 4.32: The various force components obtained from added mass experiments. Excerpt from experiment with H2LT configuration with $\alpha = 20$ and $\omega = 80$.

Chapter 5

Results

This chapter presents and discusses the results for drag coefficients and added mass coefficients based on performed simulations and experiments. The results regarding the drag coefficients are obtained from flow simulations in Solidworks, a passive towing tank experimental approach, and circulation tank experiments. The results related to the added mass coefficients are obtained from simulations in WADAM and circulation tank experiments. The results for drag coefficients are presented first, followed by results for added mass coefficients. For both cases, simulation and experimental results are compared. Simulations are performed on nine different snake configurations, named H1LT, H2LT, ..., H9LT. Each consisting of head and tail modules and from one to nine middle links. Due to limitations in size, the experimental approaches are performed on the H1LT and H2LT snake configuration only.

All result files are found in Appendix A and Appendix B

5.1 Drag Coefficients

Drag coefficients are found from forces and velocities obtained from simulations and experiments as discussed in Chapters 3 and 4. The simplified work flow for obtaining the drag coefficients from the forces is illustrated in Figure 5.1

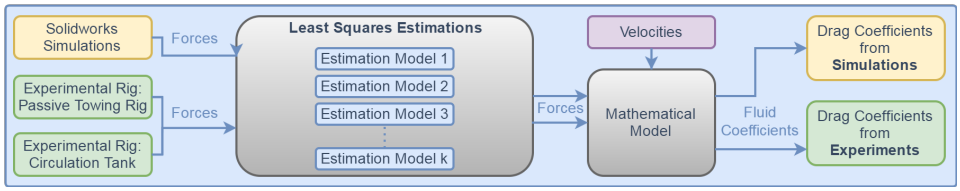

Figure 5.1: Illustration of the work flow for estimation of drag coefficients.

This section is organized as follows: Simulation results are presented together with a system identification based on a least squares approach. It is followed by results and system identification for the experimental procedures. The section is concluded with a summary of the findings.

5.1.1 Solidworks Simulations

Solidworks returns forces in body x and y directions for each case of combined input velocity and angle of attack. For each of the nine body configurations, five simulation scenarios are run, Table 3.4. The first being at 50 flow velocities ranging from 0.02 to 1 m/s with an angle of attack set to zero, $\theta = 0$ degrees. The last four cases are run at four different flow velocities, each for varying angle of attack, θ.

Case 1: Zero Angle of Attack at Increasing Velocities

In the case of zero angle of attack, the resulting forces obtained from the Solidworks flow simulation are presented in Figure 5.2. The forces returned by the simulation software is the fluid forces acting on the snake as a result of the fluid flow past the snake configurations. As the fluid flows are stationary, no added mass effects are present. The graph show the fluid forces acting on the nine different snake configurations, H1LT throguh H9LT, as a result of the fluid flow velocity. Following previous notation, the positive x axis is in the direction of travel, and thus the fluid forces acting on the snake have negative sign. As a result of the snake geometry

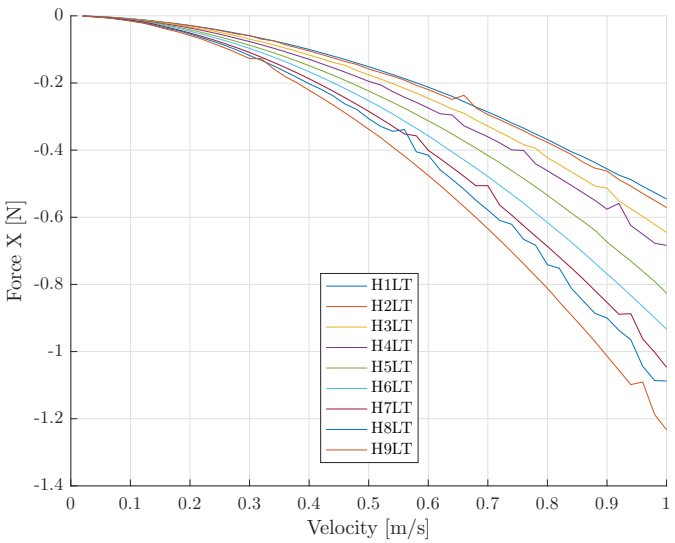

Figure 5.2: Simulation results for all snake configuration exposed to a fluid flow at θ=0 degrees for increasing velocities.

being symmetrical about the xy and xz plane, body y forces are omitted as these are minuscule and produce no viable results. In general, Figure 5.2 reveals expected behaviours, meaning that the fluid forces are zero for $v = 0$ and increases with increasing velocity. Additionally, the forces are further amplified for larger snake configurations. It is clear that the main trends are consistent, and the force curve for each configuration follows a predictable curve.

Spikes and noise is observed for most of the snake configurations. The major effects are observed at velocities greater than $v = 0.5$ m/s. The spikes are of

various amplitude and do not appear at the same velocities for the different snake configurations. The observation of spikes and noise effects is a recurring tendency in all performed simulation schemes. Possible explanations for the noise effects and why the H5LT and H6LT configurations are exposed to less noise is discussed later.

Cases 2-5: Varying Angle of Attack for Given Velocities

The comprehensive results from the simulation cases concerning various angles of attack is presented graphically in Figures 5.3 and 5.4. The graphs show forces in body x and y direction for four different velocities, with an angle of attack between 0 to 90 degrees. By exposing the snake configuration to fluid flows from different angles, forces in both body x and y direction are obtained. This makes it possible to identify drag coefficients in x and y direction, C_f and C_d for the original model, and the various variations of the model.

Considering first the y forces seen in Figures 5.3(b), 5.3(d), 5.4(b) and 5.4(d), all forces start at zero as previously mentioned. The overall behaviour is similar for all four velocities, varying mainly in amplitude. As the angle of attack is increased, the force increases in a sinusoidal manner as the body forces are directly correlated to the body velocity. As the angle of attack is increased beyond approximately 40-50 degrees spikes are starting to appear frequently. This might be due to the fluid flow direction being more perpendicular to the cylindrical form of the bodies. For small angles, the head and tail module heavily limits turbulent fluid behaviour around the snake modules configuration. For a cylinder, turbulent behaviours may appear for fluid flow perpendicular to the cylinder axis. As the snake configurations largely resembles a cylindrical body, such behaviour should be expected.

Forces in body x direction are of far less magnitude. This is expected as the characteristic area in x direction is inferior to that in y direction. The forces are increasing with the size of the snake configuration and decreasing as the angle increases. At approximately 40 to 60 degrees angle of attack, the body x forces are giving a positive force against the fluid flow. This is possibly due to the dissimilar geometry of the head and tail modules. If the geometry of the head and tail modules were identical, the forces would converge to zero as θ approaches 90 degrees. This is because the velocity in x direction is zero for θ=90 degrees. The head module is quite bulky with a wide front to accommodate a camera and LED lights and other devices. Whereas the tail has sharper edges. The difference between the two modules is clear in Figure 4.7. When the snake configuration is exposed from fluid flow in y directions, positive force contributions in body x direction appears, pushing the body forwards. The effect is small, but superior to the general drag forces in x direction, resulting in the total forces being positive for flow angles greater than 40-50 degrees. From this, one would expect the positive x force having its largest value at $\theta = 90$ degrees. Despite this intuitive explanation, the peak is located at roughly 78 degrees, after which it is decreasing and returning to the drag forces being the dominant player. A possible explanation is that, especially for the head, the surfaces are not straight lines, but a combination of lines and curves of different length and bend radius. The result being that the y velocity components leads to equal force in x direction.

The noise is more prominent in the x force plots than for y forces. One aspect is the general amplitude of the measured forces in x direction being small. The results may therefore be more easily influenced by simulation errors. In addition, the fluid is generally more turbulent in the x direction for the angled cases as the geometry resembles a cylinder. The noise and spike aspects are discussed in general the next subsection.

For all cases presented in Figures 5.3 and 5.4, although troubled with noise, the general behaviour of the obtained forces are consistent and can provide a good basis for the identification of the fluid coefficients. Especially if the angle of attack is limited to a maximum of 40 degrees, which is a common chosen amplitude range for the motion of the link angles for swimming snake robots [18], [22].

Noise and Spikes in Simulation Results

The reason for the observed noise and spikes are unknown. One hypothesis is the available computational resources available for a given simulation scenario. Simulation mesh refinement and the size of the Computational Domain are the

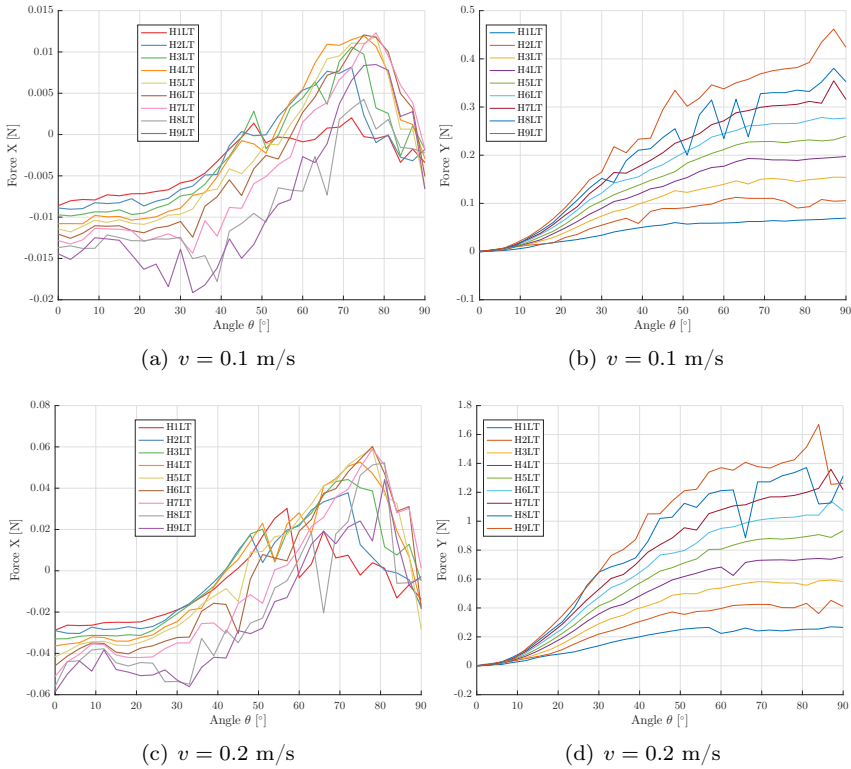

(a) $v = 0.1$ m/s (b) $v = 0.1$ m/s

(c) $v = 0.2$ m/s (d) $v = 0.2$ m/s

Figure 5.3: Simulation results for all snake configurations exposed to fluid flow for different angles at velocities $v = 0.1$ and $v = 0.2$ m/s.

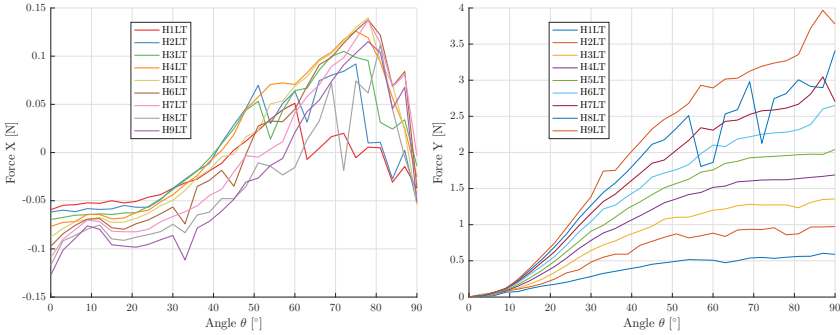

(a) $v = 0.3$ m/s

(b) $v = 0.3$ m/s

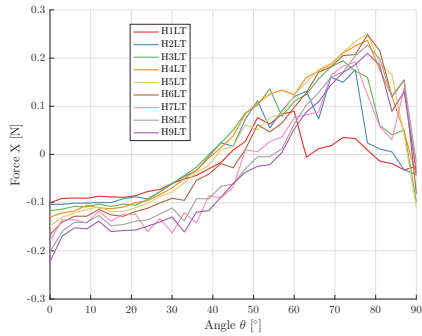

(c) $v = 0.4$ m/s

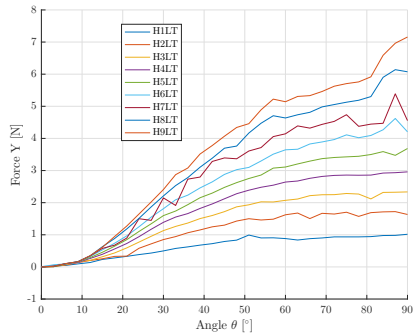

(d) $v = 0.4$ m/s

Figure 5.4: Simulation results for all snake configurations exposed to fluid flow for different angles at velocities $v = 0.3$ and $v = 0.4$ m/s.

two components that determines the complexity of the simulations. The size of the CD is defined based on the snake module configuration size as discussed in Chapter 3.1.2. Simulations are run at the second most refined mesh setting, as preliminary simulation tests on the highest mesh setting resulted in the simulations crashing. It is possible that the chosen mesh setting results in the simulations approaching a resource limit, and thus is struggling to reach some of the various convergence criteria. As a result one would expect the spikes to increase with the size of the snake configuration. From Figure 5.2 this is seen to be generally correct, with the exception of the H5LT and H6LT configurations. However, these two simulation cases are run on the far more powerful server farms than the other configurations. This is in support of the hypothesis. On the other hand, larger snake configurations should lead to less turbulent fluid behaviour in the case presented in Figure 5.2.

Noise and spikes are clearly more present in the angled cases in Figures 5.3 and 5.4. The noise is still increasing with the snake configuration size as previously proposed. The disturbances are especially noticeable for the H8LT configuration, but is somewhat less apparent for the H9LT configuration. However, as seen in

Figures 5.4(c) and 5.4(d), for $v = 0.4$m/s forces acting on the H8LT configuration are less troubled with spikes than the less computationally demanding H7LT configuration. As the simulations for the H8LT configuration were run on one of the server farms, this further supports the claimed hypothesis.

It is interesting to directly compare the outcome of the same simulation scenario run on two different computers. Figure 5.5 show the results for the H9LT configuration for a varying angle of attack at $v = 0.3$ m/s. The simulations are run on Computer 1 and Server farm 1 (Table 3.5). The simulation case in question is one of the most demanding cases, and a difference in the results is expected. The plotted results highly supports the proposed hypothesis. While spikes do indeed occur for the server calculations, the amount is clearly less than for the simulations done on a regular computer.

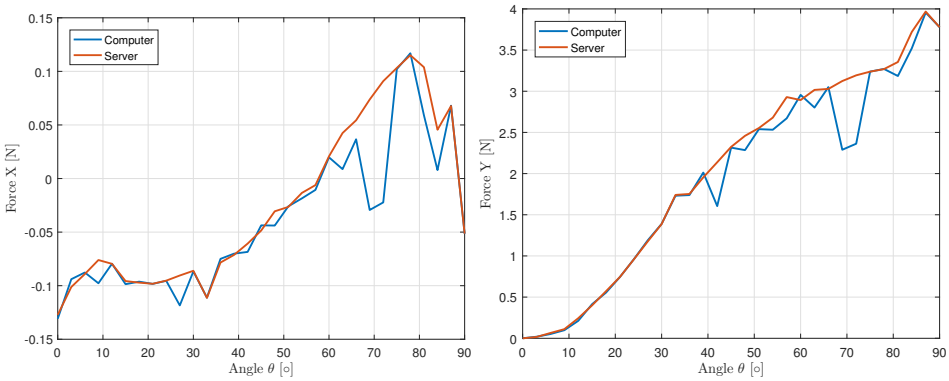

(a) (b)

Figure 5.5: Comparison of an identical simulation scenario run on computer and server farm. For H9LT at $v = 0.3$ m/s and varying θ.

A reasonable suggestion is to perform the simulations on a less refined mesh setting to reduce the noise generated by the highly computationally demanding simulations. Prior to the simulations performed for this thesis, a large set of similar simulation cases was performed to investigate the simulation behaviour. In these preliminary simulations, the mesh refinement was set at the default value of 3 and the CD was at its default size, resulting in far larger CDs than for this thesis. The simulations were performed only on two snake configurations: H1LT and H2LT. While the overall results were similar, the results from the simulation tests showed far more tendencies of noise and spikes than what has been presented in this thesis. The conclusion at that point was to increase the mesh refinement to obtain more accurate results, which the results in this thesis have shown to be.

Ideally, all simulations should be run on the powerful server farms or on equally powerful computers. Thus reaching a limit in computational performance would be avoided. For the sake of this thesis, it is not possible. The available server farms are shared between multiple users and are generally slow as a result of this, even though the actual available computational resources are beyond what is needed.

For the used composition of six computers working in parallel on the simulations, the time needed for completion was six weeks. Running all simulations on one computer would demand approximately nine months of computing time. Further, considering expanding the CD would require additional computing time. This is not feasible for the scope of this thesis. Note that with the available resources, the obtained simulation results with the mesh refinement level of 6 gave sufficient results which are compared with the experimentally obtained data.

System Identification

The force data generated from the simulation cases is utilized in a least squares estimation scheme to determine the fluid coefficients for drag. The estimation scheme is applied to both the original model for the drag forces, Equation 2.22, and for the various adaptions made to this model, Chapter 2.3. Based on all simulation data, each estimation model returns the corresponding fluid coefficients. Further, the estimated fluid coefficients are included in the different force models and compared to the simulation results. Figure 5.6 show this for snake module configurations H1LT, H2LT, H5LT and H8LT at zero angle of attack $\theta = 0$ degrees. The original model $\hat{\mathbf{f}}_1$ together with $\hat{\mathbf{f}}_2$ and $\hat{\mathbf{f}}_6$ are the least successful estimates, but have less error as the snake configuration is extended. The remaining models, $\hat{\mathbf{f}}_3$, $\hat{\mathbf{f}}_4$ and $\hat{\mathbf{f}}_5$ are far more fitting and returns almost the exact same forces. The latter three estimation models all includes drag coefficients for the head and tail module as is not the case for the other model variations. As the geometry of the head and tail modules are vastly different to the link modules, it is perhaps no surprise that the models including these tends to be more precise.

For the angled cases, Figure 5.7 show comparisons of simulated and estimated forces on configurations H1LT, H2LT and H5LT at a velocity $v = 0.3$ m/s. Focusing firstly on the forces in x direction, none of the model variations are truly fitting. The closest matches are found for H5LT and larger configurations where the most estimation models are reasonably close to the simulations up to $\theta = 30$ degrees. For larger angles, $\hat{\mathbf{f}}_4$ stands out as most fitting. Being the sole candidate providing positive forces for large angles of attack. Referring to Chapter 2.3, $\hat{\mathbf{f}}_4$ is the most complex model, containing 10 drag coefficients, indicating this should be the most fitting model.

In contrast to the x forces obtained from the simulations, the y forces are more consistent and should result in better estimations. For larger snake module configurations, the various model variations are quite similar in behaviour. However, none of the model variations are truly close to the simulation results. Although there are some strange behaviour being observed for $\theta > 50$ degrees, this is not really of great importance for real life applications. As have been mentioned earlier, common gait patterns for underwater snake robots generally considers link amplitude motions $\theta \leq 40 - 50$ degrees.

Figures 5.6 and 5.7 concerns only a few simulation cases for a selection of snake module configurations, although the estimations are based on all simulation data. A statistical analysis for how well each model variation fits to the simulation cases is presented in Figure 5.8. Pearson, Spearman and Kendall's correlation coefficients,[14], [24], indicates how well the estimated data set correlates to the

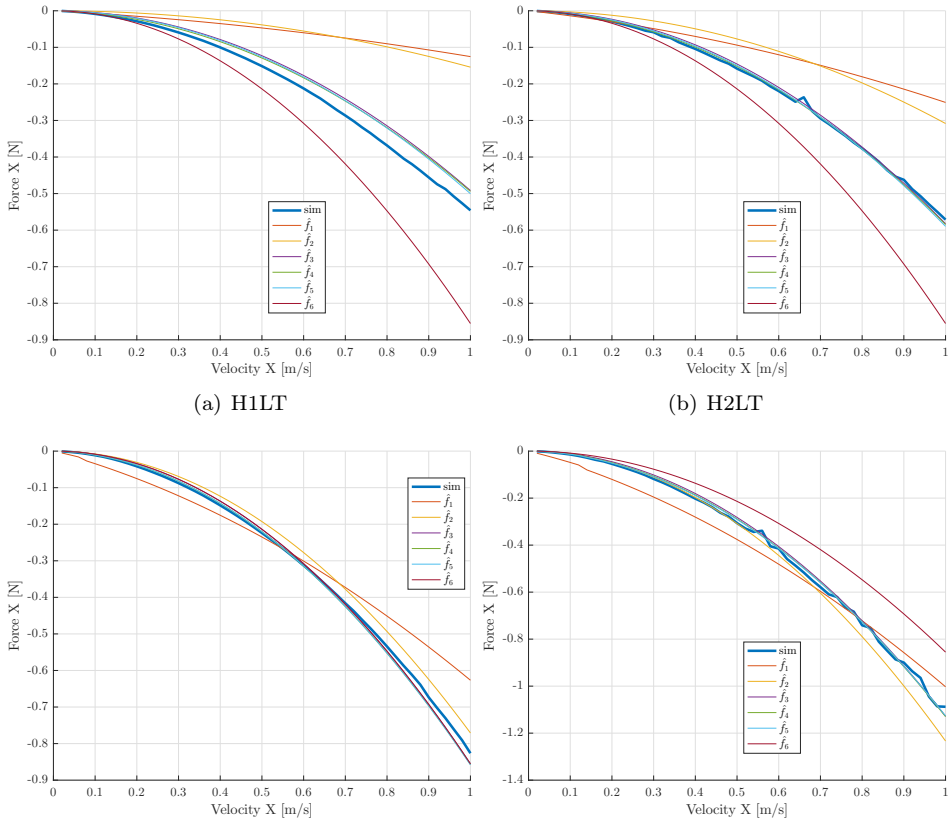

(a) H1LT (b) H2LT

(c) H5LT (d) H8LT

Figure 5.6: Estimation results compared to simulation results for four different snake module configurations, for $\theta = 0$ degrees.

simulation results. A value of 1 indicates perfect positive correlation. The resulting coefficients indicates that the force model $\hat{\mathbf{f}}_4$ have the highest correlation in x and in y.

Drag Coefficients from simulations

The resulting fluid coefficients obtained for the different estimated force models based on the simulation data is seen in Table 5.1.

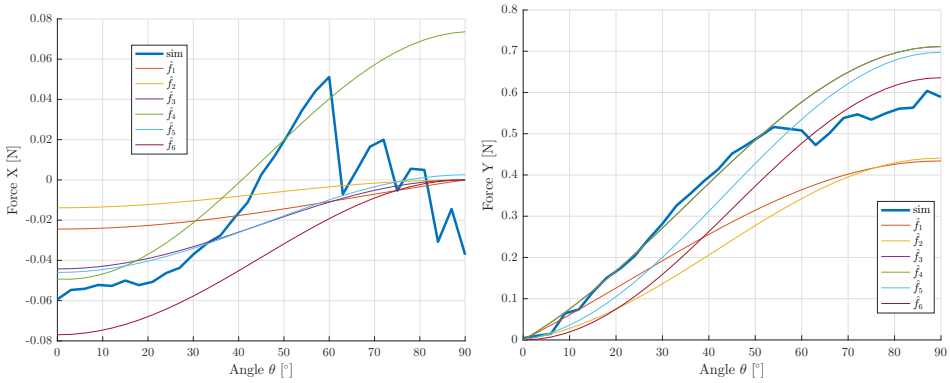

(a) H1LT - X

(b) H1LT - Y

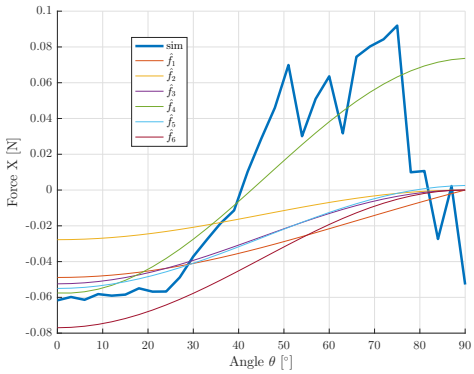

(c) H2LT - X

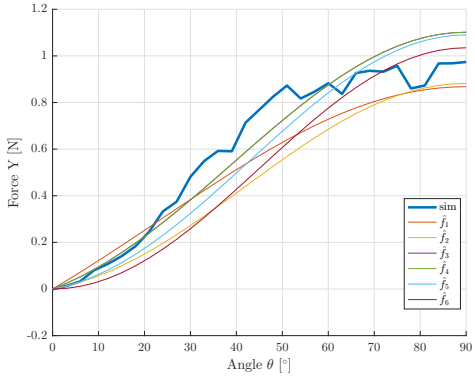

(d) H2LT - Y

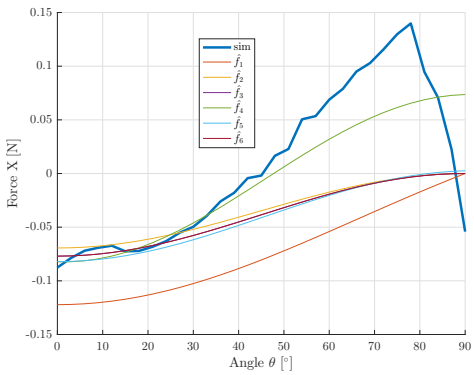

(e) H5LT - X

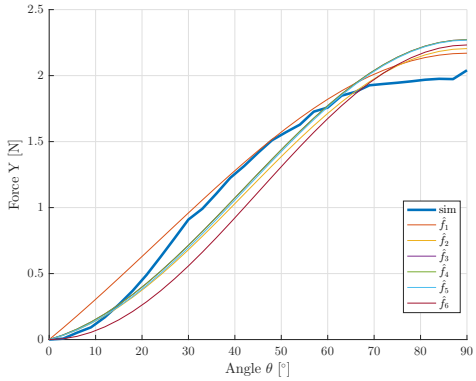

(f) H5LT - Y

Figure 5.7: Simulation results for $v = 0.3m/s$ at different angles θ, with different configurations.

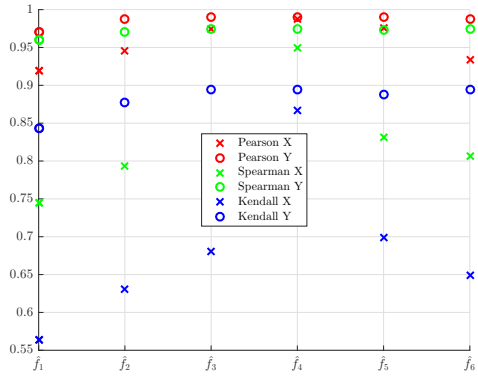

Figure 5.8: Pearson, Kendall and Spearman correlation coefficients for the simulated and estimated data sets.

		Model variations					
		$\hat{\mathbf{f}}_1$	$\hat{\mathbf{f}}_2$	$\hat{\mathbf{f}}_3$	$\hat{\mathbf{f}}_4$	$\hat{\mathbf{f}}_5$	$\hat{\mathbf{f}}_6$
Fluid Coefficients	C_f	0.0046					0.2361
	C_d	0.1206					0.4807
	C_f^I		0	0	0	0.0003	
	C_d^I		0.0374	0.0191	0.0191	0.0374	
	C_f^{II}		0.0112	0.0066	0.0066	0.0062	
	C_d^{II}		0.4063	0.4064	0.4064	0.3484	
	$C_{f_{HT}}^I$			0	0.0063		
	$C_{d_{HT}}^I$			0.1956	0.1956		
	$C_{f_{HT}}^{II}$			0.1106	0.1050	0.1134	
	$C_{d_{HT}}^{II}$			0	0	0.6186	
	C_{XY}^I				0.0055		
	C_{XY}^{II}				0.1957	0.1779	

Table 5.1: Fluid coefficients identified based on simulations.

5.1.2 Passive Towing Rig Experiments

The Towing rig experiment results in data from the 6-axis force/torque sensor as well as velocities. From the six available measurements, only forces in x and y directions are considered as these are the ones of importance. The accuracy of the recorded forces and estimated velocities is deemed sufficient, as stated in Chapter 4.3.7. Due to size limitations, the experiments are only conducted for the H1LT and H2LT snake module configurations.

Case 1: Zero Angle of Attack at Increasing Velocities

Figure 5.9 show the recorded forces from the passive towing rig experiments. Again, forces in y direction have been omitted as they are insignificant. Figure 5.9(a) presents the recorded forces. Each cluster of crosses are the forces for each of

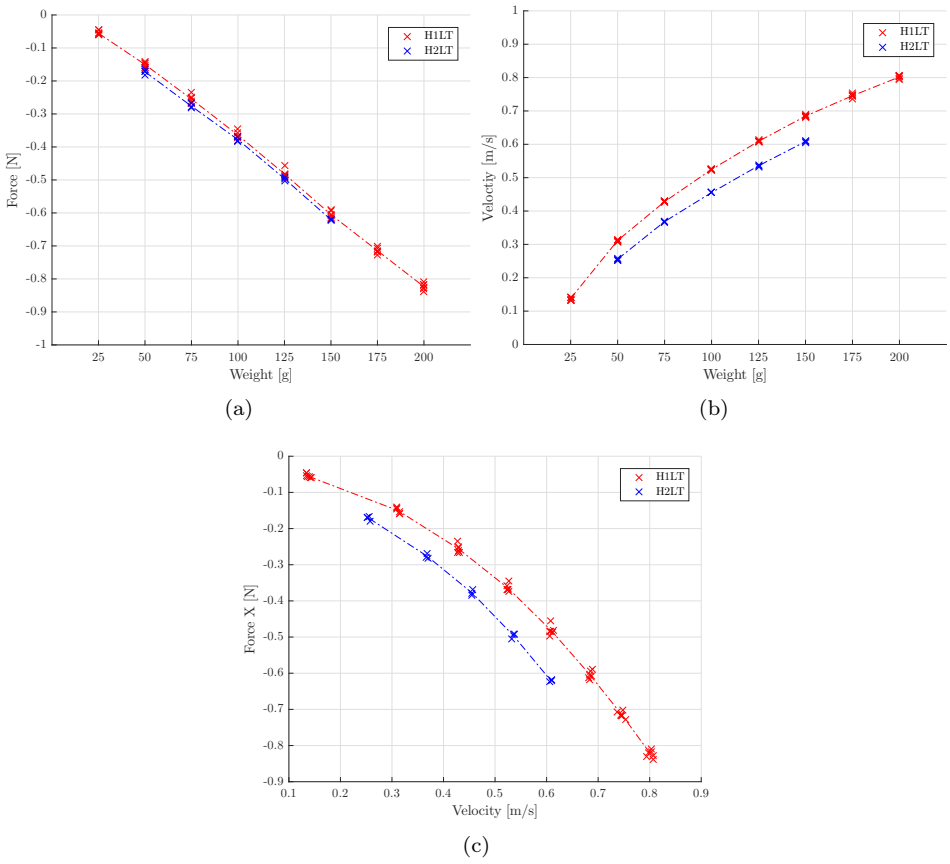

Figure 5.9: Experimental results on H1LT and H2LT for $\theta = 0$ degrees for different weight inputs.

the six performed runs per weight input. The force is increasing linearly with the applied weight input. The results for H2LT show a slightly higher recorded force, which is expected due to the difference in size and mass. Similarly, for a given weight input, the resulting velocity differs from the two snake configuration, as seen in Figure 5.9(b). Finally, the forces as a function of the velocity is plotted in Figure 5.9(c), in a similar fashion as for the simulation results in Chapter 5.1.1.

The recorded forces from this experiment are higher than for the simulations, while still having the same qualitative behaviour. The reason behind the deviation is investigated later in this section.

Case 2: Varying Angle of Attack for Given Weight Inputs

The experiments with varying angles of attack were performed with three different weight inputs for both snake configurations. Chapter 4.3.2 discusses the upper and lower weight limits. Further, the angle of attack is mechanically limited to 0

to 40 degrees. Figures 5.10(e) and 5.11(e) show, for both snake configurations at different weight inputs, the resulting velocities as a function of the angle of attack. The qualitative behaviour is similar, with some minor exceptions. Figures 5.10(a), 5.10(b), 5.11(a) and 5.11(b) portray the body forces for a varying θ. The results resembles the behaviour of the simulations, where y forces are increasing with the angle and the x forces are decreasing. However, as the maximum angle is 40 degrees, no information is available regarding the effects in the x force occurring at larger angles.

In figures 5.10(c), 5.10(d), 5.11(c) and 5.11(d), the global velocity is transformed to body velocity as a function of θ. As the recorded force and velocity is closely related, the expected behaviour would be for all the data points to form a single line. This should be the case regardless of the given input weight. This suggests errors in either one or both of the force measurements and velocity estimations. The latter is the most likely case, as will be discussed later.

Unlike the experimental approach cases for $\theta = 0$ degrees, there is now no direct visual comparison between the simulations and experiments. Except the fact that the recorded forces are higher in this case as well. The simulations were done at four given flow velocities, whereas this experiment returns different velocities dependent on the combination of θ and the weight input.

The results from this experiment show in large degree an expected behaviour, but may be lacking accuracy. A further comparison between simulation and experimental results is presented later.

Sources of Error

As mentioned in the previous paragraphs, the simulation and experimental results differ to some degree. Assuming the simulation results are correct, the following is a summary of possible sources of error in the performed experiments.

- The correctness of the result relies upon the system reaching a steady-state velocity with zero acceleration. The pool size results in a limited travel length for the system. The measured forces will contain added mass components if the wagon is still accelerating while the force measurements are being recorded. This will contribute to a higher measured drag force. The possibility of an ongoing acceleration should be examined by using an accelerometer mounted on the wagon, which was not possible with this setup.
- The system is not completely rigid. The snake module configuration is attached to the wagon by a 0.4 m long rod. As the wagon is released, the rod might bend and cause the snake to oscillate in x direction. The rod has been reinforced which reduces this effect. In addition, the attachment point between the rod and the wagon may also be a source of a wobbling effect. This might lead to the averaging of the recorded forces not being precise.
- Again, due to the small size of the pool, every movement in the water is a cause for waves and turbulent fluid behaviour. An experimental run is not conducted until the water has calmed down. This is confirmed visually and by looking at the current measurement readings. However, there may still be undesired effects in the water that affects the measurements. While

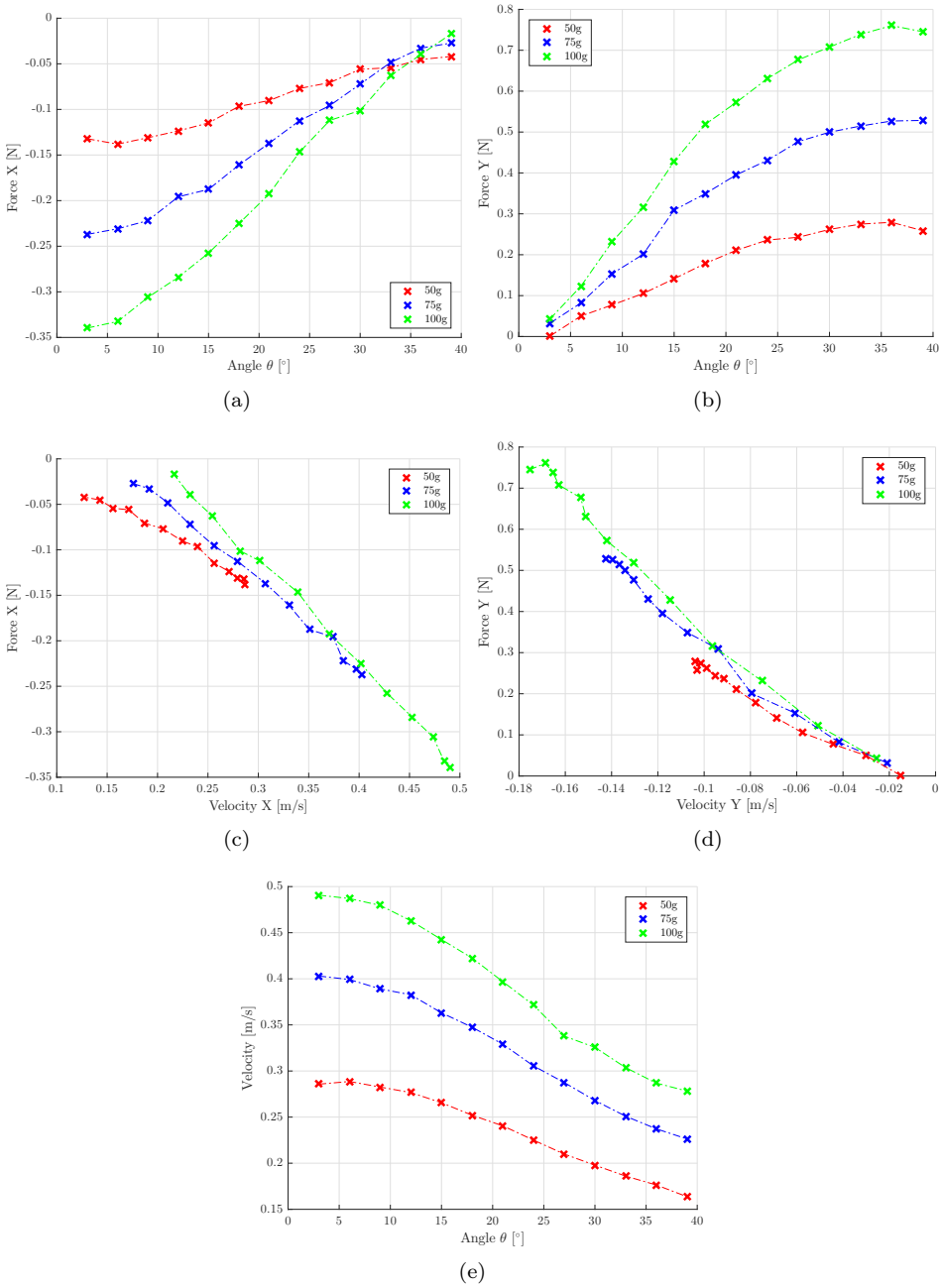

Figure 5.10: Experimental results on H1LT for varying θ for different weight inputs. Velocities in (c) and (d) are the body velocities based on (e).

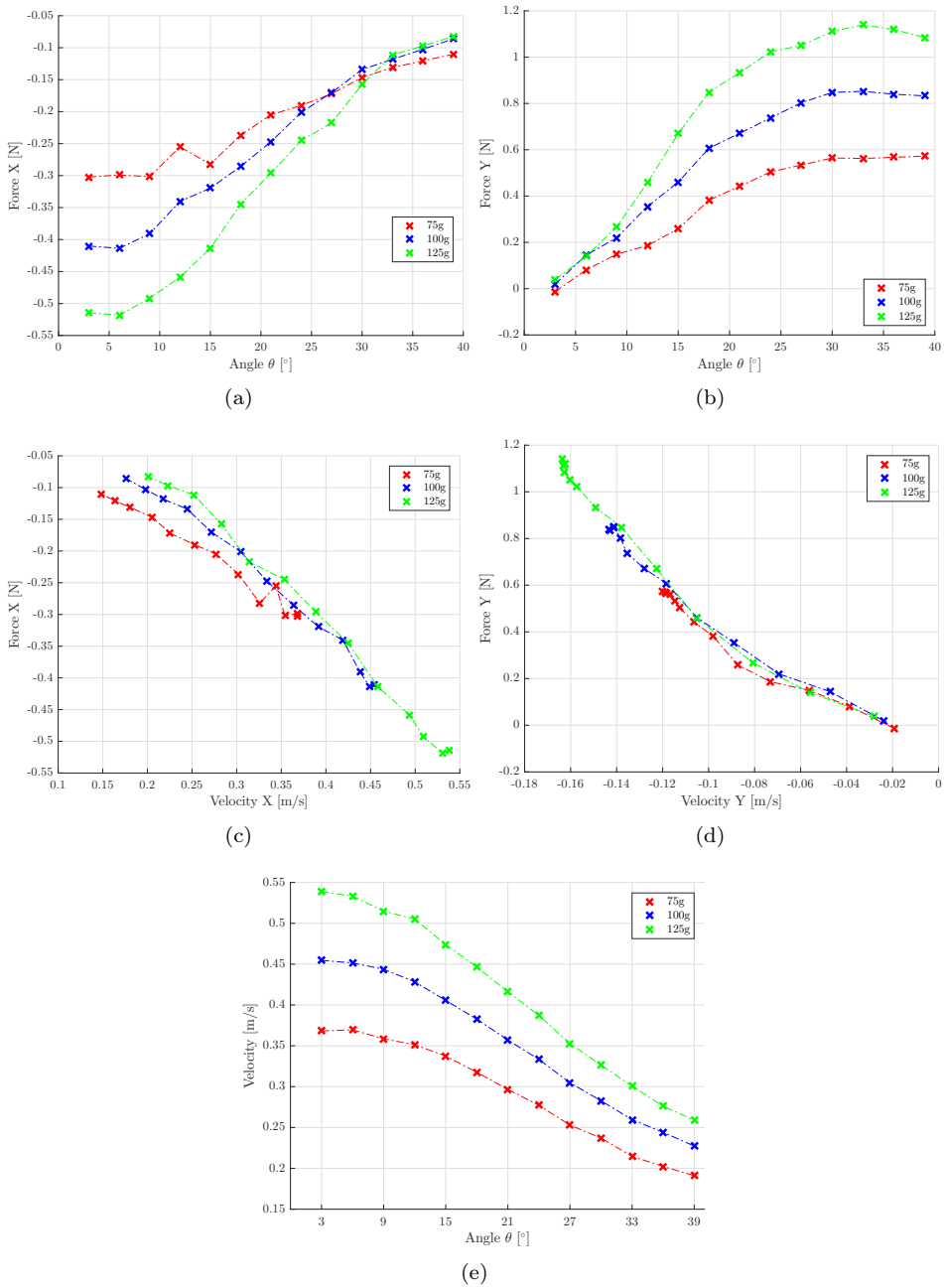

Figure 5.11: Experimental results on H2LT for varying θ for different weight inputs. Velocities in (c) and (d) are the body velocities based on (e).

an experimental run is conducted, water may bounce back from the walls, causing incorrect force measurements.

- Even though the 3D printed snake modules originally are identical to the geometry models used for the simulation, a few modifications have been made. These are described in Chapter 4.2.1. The resulting opening around the rod and cable entrances is a source for turbulent fluid behaviour as sharp edges occur. The same is true for the rod itself. If however, the experiments are conducted for larger snake module configurations, such as H3LT and so forth, the effects caused by the rod and openings will be less, compared to the other measured forces.
- The Dragon Skin coating is applied to obtain a smoother surface, as described in Chapter 4.2.2. The painting process is done manually and carefully. Still, the cured skin will not be completely evenly distributed on the snake module configuration. When curing, the snake module configuration is hanging from the rod. As the skin is initially liquid, gravity will pull some of liquid to the bottom of the configuration. Resulting in droplets being formed. Finally, the applied skin, although very thin, causes the overall size of the configuration to expand.

Although some of the challenges listed above are minuscule, the total combination is a source of error. Note that generally the simulations are conducted considering ideal cases, while during experiments the different factors can affect the obtained results.

System Identification

Similarly to the procedure in the previous section concerning the simulation results, system identifications were performed for several model variations. Figure 5.12 show the results for the H1LT and H2LT snake module configurations together with the estimated models. The results from the experiment and the estimated models seems to fit more accurately, despite the number of data points being significantly less than for the simulations. Comparing Figures 5.12(a) and 5.12(b), a larger configuration of the snake robot, seems to fit better with the different models. This observation is discussed in Chapter 5.1.4 in light of the results from the simulations and circulation tank experiments.

Figures 5.13 and 5.14 show the results for H1LT and H2LT for different values of θ and weights. Figures 5.13(a), 5.13(c) and 5.13(e) show the results in x direction for H1LT at different weights, and Figures 5.13(b), 5.13(d) and 5.13(f) the results in y direction. Most of the estimation models have similar qualitative behaviour as the measured forces. Estimates $\hat{\mathbf{f}}_1$ and $\hat{\mathbf{f}}_2$ seem to be the least fitting in x and y direction, but behaves in the same way for the different weights.

For the H2LT configuration, shown in Figure 5.14, the trend is similar to the H1LT case. Again, the different models fit better then for H1LT, indicating that larger snake module configurations could provide more consistent results.

Overall, the estimates for model variation $\hat{\mathbf{f}}_4$ is the most fitting model. This is further backed up by the statistical analysis in Figure 5.15, where it has the highest correlation for all three statistical analyses.

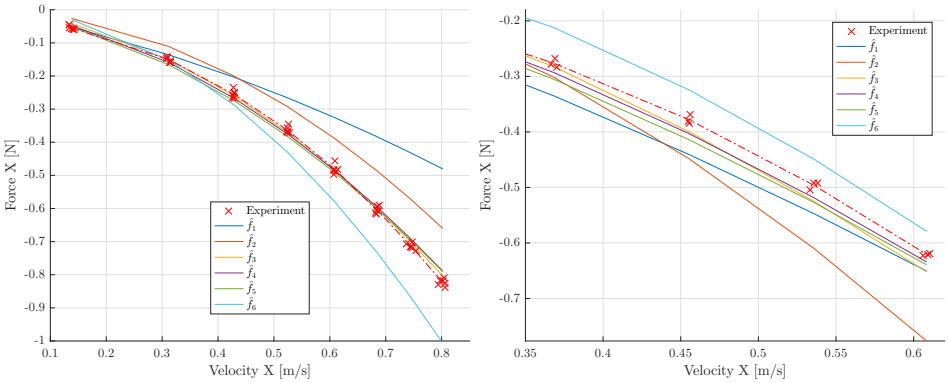

(a) H1LT (b) H2LT

Figure 5.12: Comparison of experimental results to different estimated models, for $\theta = 0$ degrees.

Drag Coefficients from passive towing rig experiment

The resulting fluid coefficients obtained for the different estimated force models based on the passive towing rig data is seen in Table 5.2.

		Model variations					
		$\hat{\mathbf{f}}_1$	$\hat{\mathbf{f}}_2$	$\hat{\mathbf{f}}_3$	$\hat{\mathbf{f}}_4$	$\hat{\mathbf{f}}_5$	$\hat{\mathbf{f}}_6$
Fluid Coefficients	C_f	0.0242					0.4319
	C_d	0.2813					1.7712
	C_f^I		0.0042	0.0109	0.0152	0.0177	
	C_d^I		0.0193	0	0	0.0184	
	C_f^{II}		0.0693	0.0149	0.0045	0	
	C_d^{II}		2.2438	1.5249	1.5249	1.3918	
	$C_{f_{HT}}^I$			0	0		
	$C_{d_{HT}}^I$			0.0795	0.0795		
	$C_{f_{HT}}^{II}$			0.2363	0.2498	0.2556	
	$C_{d_{HT}}^{II}$			1.8852	1.8852	2.4598	
	C_{XY}^I				0.0870		
	C_{XY}^{II}				0.8704	0.3472	

Table 5.2: Fluid coefficients identified based on the passive towing rig experiments.

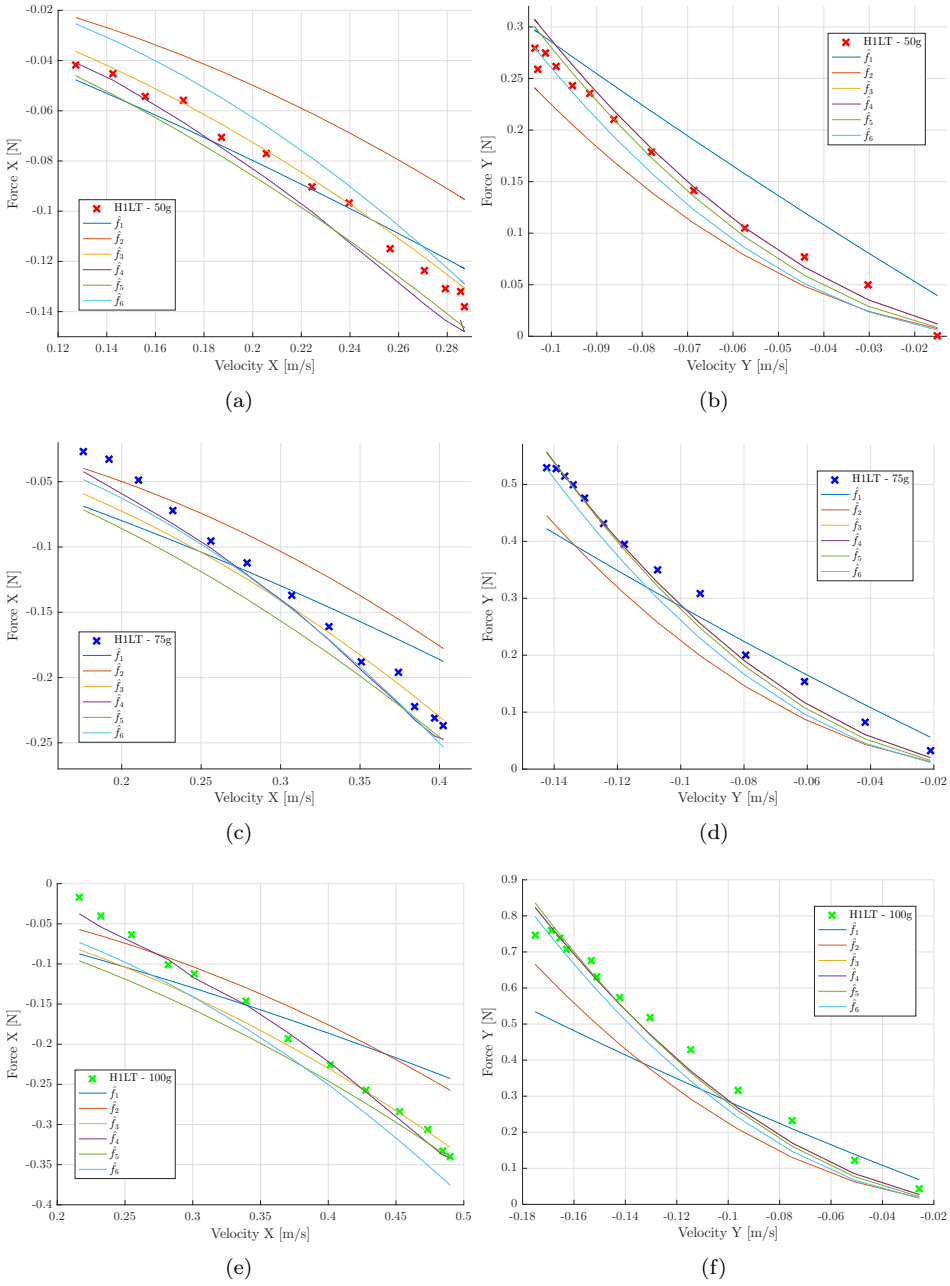

Figure 5.13: Comparison of experimental results to the estimation models. H1LT configuration.

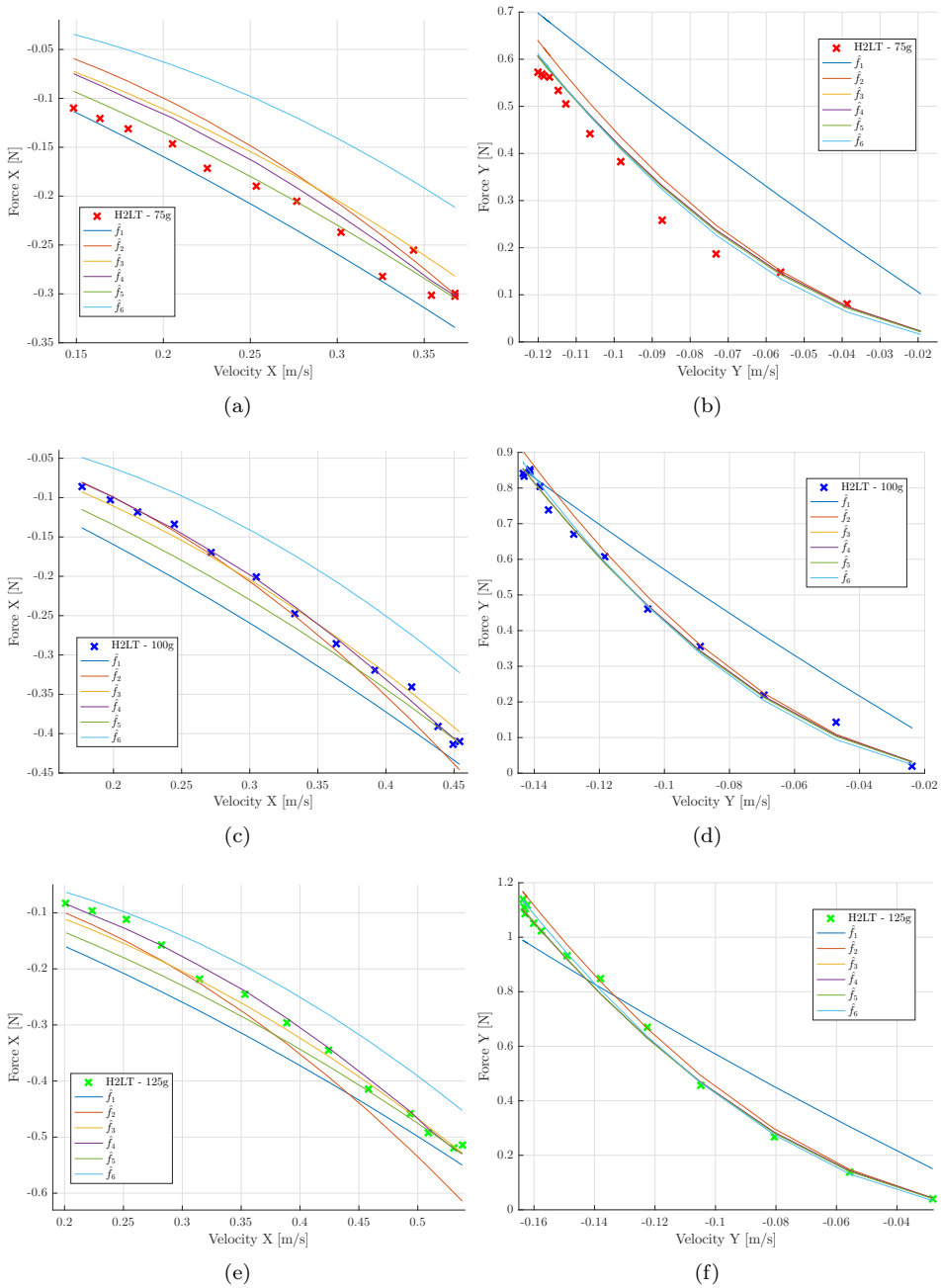

Figure 5.14: Comparison of experimental results to the estimation models. H2LT configuration.

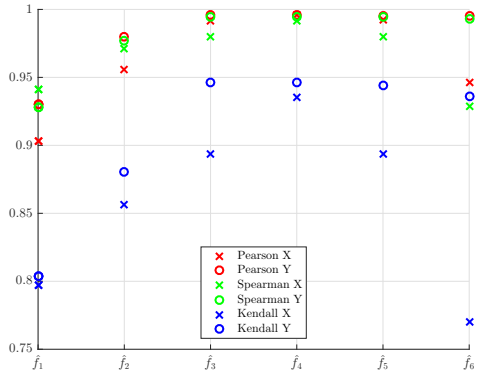

Figure 5.15: Statistical analysis of estimation based on experiments.

5.1.3 Circulation Tank Experiments

Compared to the passive towing rig experimental approach, the circulation tank experiments returns a large set of measurement data. The reason for this is the extended range of possible fluid flow velocities in the circulation tank.

Case 1: Zero Angle of Attack at Increasing Velocities

In Figure 5.16, the obtained force measurements in body x direction are seen for the two configurations H1LT and H2LT with $\theta = 0$ degrees. Again, due to symmetry, the forces in y are omitted as the measurements are very close to their theoretical value of zero. The observed behaviour is as expected, with the magnitude of the forces increasing with the fluid flow velocity and configuration size, while still having a qualitatively similar behaviour for the two configurations.

Flow velocities and water temperature measurements are collected for all experimental trials in the circulation tank. Table 5.3 presents the obtained flow velocities and water temperatures for $\theta = 0$ degrees experiments. Velocities obtained from the magnetic flowmeter are quite similar to the more accurate LDV measurements, suggesting it might be sufficient to obtain flow velocities from the built-in magnetic flowmeter in the circulation tank and still get accurate results.

Each velocity is recorded at four separate trials. For each of the four trials, the recorded velocities for a given reference velocity are very similar. For each velocity, the trials are conducted for different water temperatures and at different days for the two snake module configurations. At the first day of the experiments, the circulation tank was filled with water with a temperature lower than the ambient temperature. As a result of this, the water temperature is slowly converging towards the ambient temperature.

The recorded velocities seems to be independent of water temperatures and which snake module configuration that is submerged, making the experiments highly repeatable.

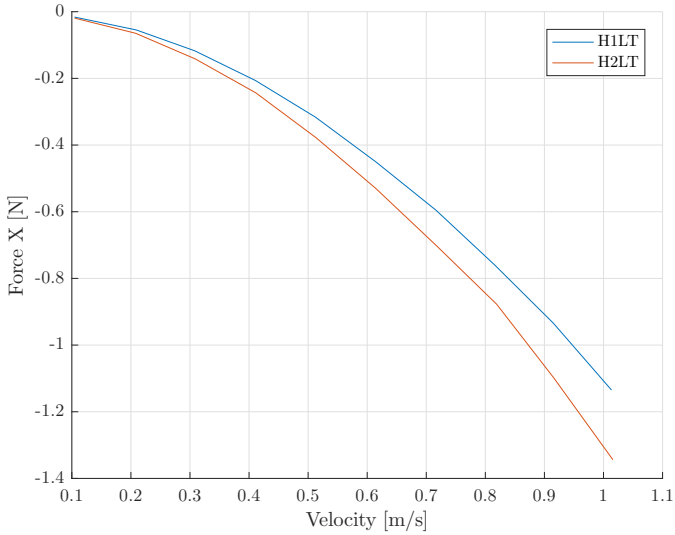

Figure 5.16: Circulation tank force measurements for H1LT and H2LT snake module configurations when exposed to a fluid flow at θ=0 degrees for increasing velocities.

Cases 2-5: Varying Angle of Attack for Given Velocities

Figure 5.17 gives an overview of the obtained forces in body x and y direction for H1LT and H2LT configurations for varying θ at four different fluid flow velocities. For forces in x direction, the fluid forces decreases for $\theta \leq 10$ degrees approximately, after which they increase up until $\theta \approx 85$ degrees before again dropping. The behaviour is a result of the geometry of the snake, leading to body y velocities affecting body x forces. The reader is referred to Chapter 5.1.1 for the discussion regarding similar behaviour for the corresponding simulation cases.

An interesting behaviour is observed in x forces for both snake module configurations, Figures 5.17(a) and 5.17(c). At $\theta \approx 40$ degrees all the recorded forces in body x direction, for both snake configurations and for all velocities, crosses the $y = 0$ axis. The only exception is for the H2LT configuration at $v = 0.3$ m/s, Figure 5.17(c), where the transition occurs at a larger θ. This is interesting input for further investigation of the hydrodynamic modelling.

Force results in y direction, Figures 5.17(b) and 5.17(d), are behaving in a more predictable way, generally increasing as θ increases. However, at $\theta \approx 60 - 70$ degrees, the forces decrease. This is probably due to unwanted effects from the side walls of the test section in the circulation tank. Additionally, this may also affect the measured forces in x direction.

Table 5.4 overviews the measured flow velocities and water temperatures for these experimental trials. The results are in accordance with what was obtained from the experimental cases with $\theta = 0$ degrees.

v_{ref}	Run 1 Flowm. [m/s]	Run 1 LDV [m/s]	Run 1 RMS [%]	Run 1 Temp. [$^\circ C$]	Run 2 Flowm. [m/s]	Run 2 LDV [m/s]	Run 2 RMS [%]	Run 2 Temp. [$^\circ C$]
For body configuration H1LT								
0.1	0.101	0.1048	1.012	17.9	0.100	0.1043	0.545	17.8
0.2	0.205	0.2097	0.899	17.9	0.203	0.2087	0.775	17.8
0.3	0.299	0.3069	0.667	17.9	0.305	0.3091	0.786	17.8
0.4	0.402	0.4085	0.751	17.9	0.409	0.4135	0.864	17.8
0.5	0.502	0.5094	0.717	17.9	0.507	0.5157	0.633	17.7
0.6	0.605	0.6135	0.650	17.9	0.612	0.6170	0.277	17.7
0.7	0.709	0.7159	0.449	17.9	0.711	0.7170	0.326	17.7
0.8	0.808	0.8155	0.463	17.5	0.809	0.8166	0.370	17.6
0.9	0.909	0.9156	0.331	17.5	0.911	0.9141	0.560	17.6
1.0	1.009	1.0110	0.655	17.5	1.018	1.0160	0.356	17.6
For body configuration H2LT								
0.1	0.100	0.1045	0.680	17.0	0.100	0.1047	0.631	17.0
0.2	0.202	0.2095	0.728	17.0	0.201	0.2063	0.979	17.0
0.3	0.302	0.3082	0.739	17.0	0.302	0.3100	0.650	17.4
0.4	0.400	0.4114	0.769	17.0	0.400	0.4115	0.745	17.4
0.5	0.500	0.5134	0.653	17.0	0.500	0.5133	0.677	17.4
0.6	0.605	0.6146	0.568	17.0	0.605	0.6135	0.620	17.4
0.7	0.707	0.7161	0.467	17.0	0.710	0.7220	0.625	17.4
0.8	0.811	0.8170	0.281	17.1	0.809	0.8214	0.725	17.4
0.9	0.912	0.9182	0.154	17.2	0.903	0.9138	0.473	17.4
1.0	1.007	1.0160	0.255	17.3	1.009	1.0160	0.324	17.3

Table 5.3: Velocity and water temperature data for drag coefficient experiment for $\theta = 0$ degrees in the circulation tank.

v_{ref}	Run 1 LDV [m/s]	Run 1 RMS [%]	Run 1 Temp. [$^\circ C$]	Run 2 LDV [m/s]	Run 2 RMS [%]	Run 2 Temp. [$^\circ C$]
For body configuration H1LT						
$v = 0.1$	0.1046	0.689	17.9	0.1042	0.722	17.5
$v = 0.2$	0.2101	0.749	17.6	0.2086	0.966	17.6
$v = 0.3$	0.3113	0.917	17.6	0.3075	0.813	17.7
$v = 0.4$	0.4121	0.738	17.8	0.4159	0.612	17.8
For body configuration H2LT						
$v = 0.1$	0.1050	0.853	16.4	0.1053	0.768	16.4
$v = 0.2$	0.2114	0.718	16.5	0.2097	0.633	16.6
$v = 0.3$	0.3080	0.768	16.8	0.3084	0.673	16.3
$v = 0.4$	0.4177	0.766	17.3	0.4128	0.857	17.4

Table 5.4: Velocity and water temperature data for drag coefficient experiment for varying θ in the circulation tank.

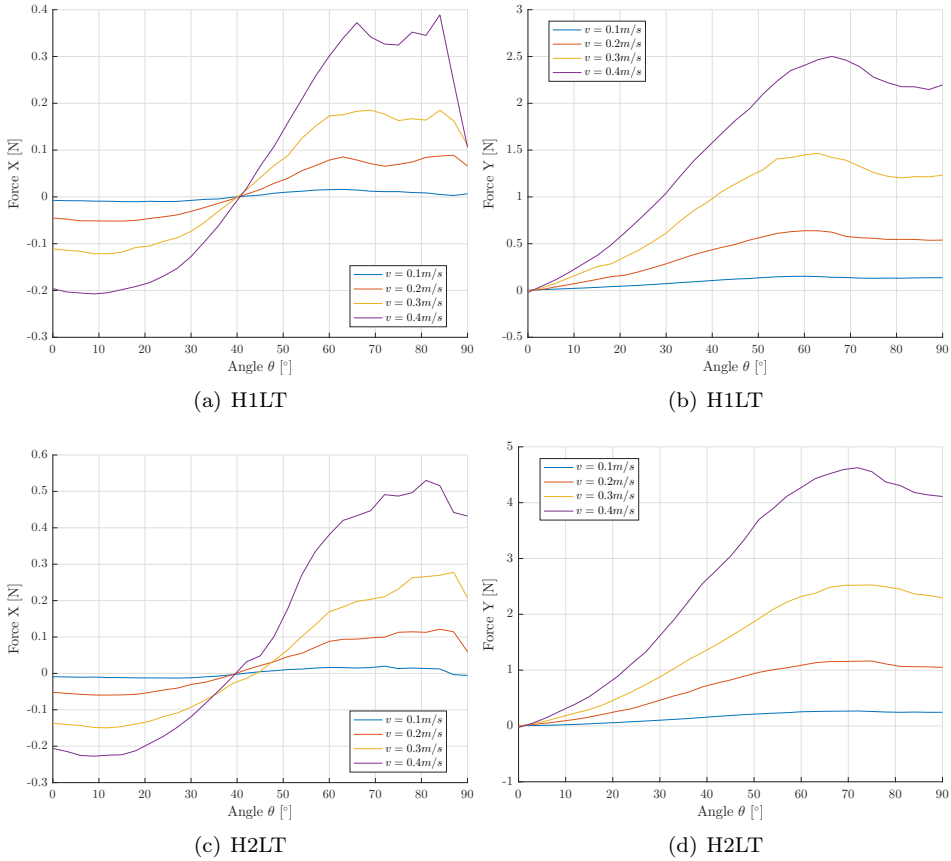

(a) H1LT (b) H1LT

(c) H2LT (d) H2LT

Figure 5.17: Experimental results for snake module configurations H1LT and H2LT for varying θ and different fluid flow velocities.

Sources of Error

The circulation tank experiments have fewer sources of error than what has been discussed for the passive guided rail setup in Chapter 5.1.2. Mainly, the system now has steady-state velocities, a rigid mechanical system and less disturbances in the test section. Still, the possible challenges concerning the snake coating and the opening in the snake configuration around the rod and sensor cable entrance are still present.

Additionally, the width of the test section causes the nose and tail of the snake to be very close to the walls at large θ. The turbulent fluid behaviour around these snake geometries in near proximity to the walls are probable causes of erroneous force measurements. Ideally, a wider test section would eliminate these wall effects, and would additionally accommodate for larger snake module configurations.

System Identification

The system identification schemes for the circulation tank experiments are run with two different data sets as input. The first case includes the entire data set from the experiments, which is in accordance with the system identification schemes for the simulations in Chapter 5.1.1 and the passive towing rig experiment in Chapter 5.1.2. The second estimation scheme limits the input for the angled experiments to a restricted data set including the results for $\theta \leq 39$ degrees. This is done in order to mitigate the unwanted wall effects obtained from the circulation tank experiments for large θ. And additionally, $\theta \leq 40$ degrees is a common maximum amplitude for underwater snake robots gait patterns. As has been noted earlier, the forces in y direction are dropping at large θ due to the wall effects. In order to obtain accurate estimates for the added mass coefficient in y direction, accurate drag coefficients are needed. By limiting the data set to $\theta \leq 39$ degrees, the unexpected behaviour in y forces are eliminated and the estimated models should return results that are more predictable.

In Figure 5.18 the x force result for $\theta = 0$ degrees is compared to the estimated force models when the input data is unrestricted to all values of θ. Figure 5.18(a) and Figure 5.18(b) compares the H1LT and H2LT snake module configurations, respectively, with the estimations based on the restricted data set. Figure 5.18(c) and Figure 5.18(d) show the same comparison, but for the unrestricted data set. The estimated force models seems to fit satisfactory with the measured forces. The exception is $\hat{\mathbf{f}}_1$ and $\hat{\mathbf{f}}_2$ that are no good match for the H1LT configuration, but are closer for H2LT. This phenomena is further discussed in Chapter 5.1.4 when comparing the experimental results to the simulations. Additionally, the restricted data set causes a small improvement in the estimations.

Figure 5.19 show the results of the system identification for the angled case at $v = 0.2m/s$ for H1LT(Figures 5.19(a) and 5.19(b)) and H2LT (Figures 5.19(c) and 5.19(d)). The estimations are based on the restricted data set for $\theta \leq 39$ degrees.

The estimated force models in x direction are the least accurate. This could indicate that the forces in x direction are more complex then initially assumed, and requires a force model of greater polynomial degree than what is presented in this thesis. The measured values are also quite small (< 0.06 N) and are therefore more sensitive to noise and inaccuracies. In addition, none of the models except for $\hat{\mathbf{f}}_4$ accounts for positive forces in x direction.

In y direction, the estimated force models more accurately represent the measured forces, up until $\theta \approx 40$ degrees. As the data set is limited to $\theta \leq 39$ degrees, this should be of no surprise. Again, $\hat{\mathbf{f}}_1$ is the least fitting force estimation, while the $\hat{\mathbf{f}}_2$ estimation has improved compared to the $\theta = 0$ degrees case. As is noted for $\theta = 0$, experiments for H2LT cause less error in the estimations compared to H1LT.

Figure 5.20 is similar to Figure 5.19, but for $v = 0.3$ m/s. For the increased velocity, the estimations in x direction (Figures 5.20(a) and 5.20(c)) improves slightly compared to $v = 0.2$ m/s (Figure 5.19). In y direction (Figures 5.20(b) and 5.20(d)) the estimated models fit the measured forces for $\theta \leq 40$ degrees approximately. However, unlike the results for $v = 0.2$ m/s, the results for H1LT are better than

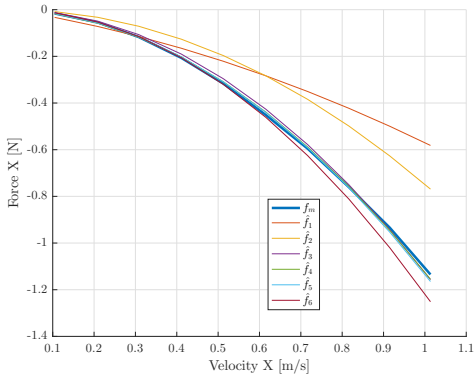

(a) H1LT. Estimations based on $\theta \leq 39$

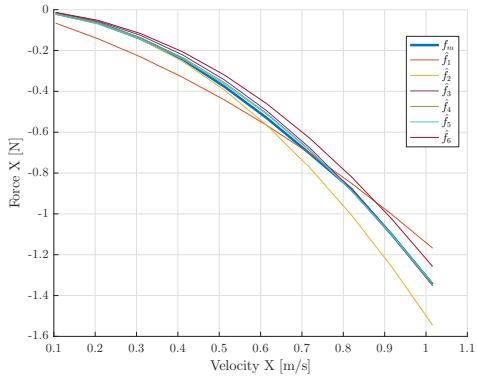

(b) H2LT. Estimations based on $\theta \leq 39$

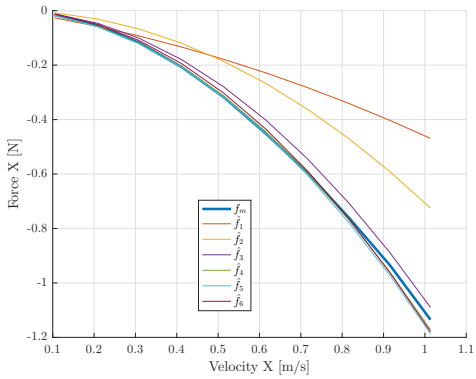

(c) H1LT. Estimations based on $\theta \leq 90$

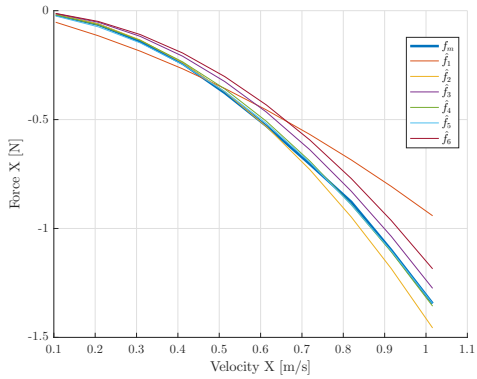

(d) H2LT. Estimations based on $\theta \leq 90$

Figure 5.18: System identification results for circulation tank experiments. For snake module configurations H1LT and H2LT for $\theta = 0$ degrees.

for H2LT in the y direction.

A comparison of estimations based on the full data set and the restircted data set is made in Figure 5.21. The comparison is made for H2LT at a fluid flow velocity of $v = 0.4$ m/s, however, the main trends are common for the other velocities and snake configurations. Generally, for both estimation cases, the estimated forces in x are not satisfactory and the error increases with the flow velocity. However, the opposite is true for forces in y direction, where increasing the velocity improves the estimations. The estimations based on the restricted data set are quite accurate within the same range of θ, and follows a more predictable curve towards the largest values of θ. For the complete data set, the estimates are less accurate, but follows the main trends of measured forces in a larger degree throughout the entire interval of θ.

Figure 5.22 show the statistical analyses of the estimation models, supporting the claim that estimation model $\hat{\mathbf{f}}_4$ is the most fitting candidate.

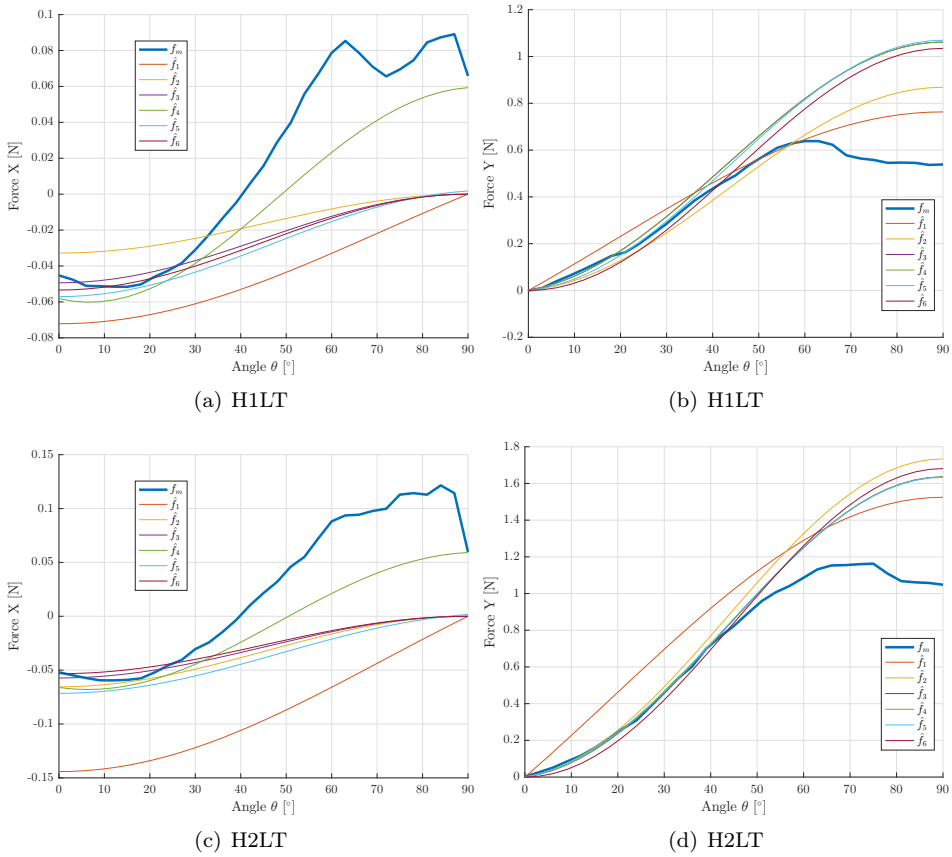

(a) H1LT (b) H1LT

(c) H2LT (d) H2LT

Figure 5.19: System identification results for circulation tank experiments. For snake module configurations H1LT and H2LT for varying θ at $v = 0.2$. Estimations are based on $\theta \leq 39$ degrees.

Drag Coefficients from circulation tank experiments

The drag coefficients obtained from the circulation tank experiments are presented in Table 5.5 and Table 5.6, where the presented results are based on the full data set and the restricted data set, respectively.

		Model variations					
		$\hat{\mathbf{f}}_1$	$\hat{\mathbf{f}}_2$	$\hat{\mathbf{f}}_3$	$\hat{\mathbf{f}}_4$	$\hat{\mathbf{f}}_5$	$\hat{\mathbf{f}}_6$
Fluid Coefficients	C_f	0.0167					0.3169
	C_d	0.3835					1.1945
	C_f^I		0	0	0	0.0040	
	C_d^I		0.1255	0.0569	0.0569	0.1255	
	C_f^{II}		0.0513	0.0126	0.0126	0.0068	
	C_d^{II}		1.2403	1.2402	1.2402	1.0488	
	$C_{f_{HT}}^I$			0	0.0141		
	$C_{d_{HT}}^I$			0.1929	0.1929		
	$C_{f_{HT}}^{II}$			0.2448	0.2531	0.2781	
	$C_{d_{HT}}^{II}$			0	1.4444	0.5383	
	C_{XY}^I				0.0412		
	C_{XY}^{II}				0.6654	0.5466	

Table 5.5: Fluid coefficients identified based on the circulation tank experiments based on unrestricted dataset

		Model variations					
		$\hat{\mathbf{f}}_1$	$\hat{\mathbf{f}}_2$	$\hat{\mathbf{f}}_3$	$\hat{\mathbf{f}}_4$	$\hat{\mathbf{f}}_5$	$\hat{\mathbf{f}}_6$
Fluid Coefficients	C_f	0.0207					0.3363
	C_d	0.3268					1.6066
	C_f^I		0	0	0	0.0032	
	C_d^I		0.0603	0	0	0.0602	
	C_f^{II}		0.0544	0.0133	0.0133	0.0088	
	C_d^{II}		1.8601	1.4272	1.4272	1.1142	
	$C_{f_{HT}}^I$			0	0.0148		
	$C_{d_{HT}}^I$			0.1769	0.1769		
	$C_{f_{HT}}^{II}$			0.2602	0.2451	0.2675	
	$C_{d_{HT}}^{II}$			1.1770	1.1770	2.0963	
	C_{XY}^I				0.0351		
	C_{XY}^{II}				0.4612	0.2963	

Table 5.6: Fluid coefficients identified based on the circulation tank experiments based on restricted dataset

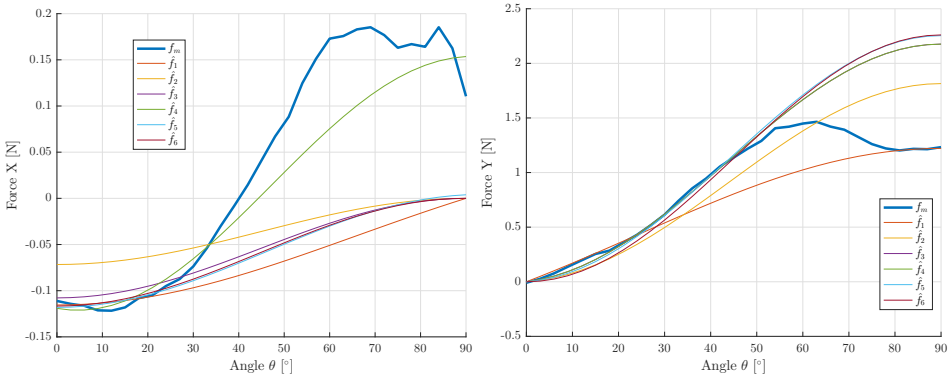

(a) H1LT (b) H1LT

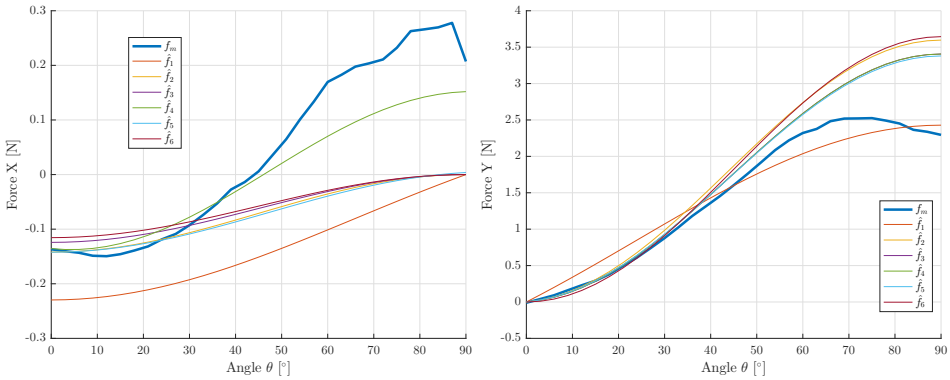

(c) H2LT (d) H2LT

Figure 5.20: System identification results for circulation tank experiments. For snake module configurations H1LT and H2LT for varying θ at $v = 0.3$. Estimations are based on $\theta \leq 39$ degrees.

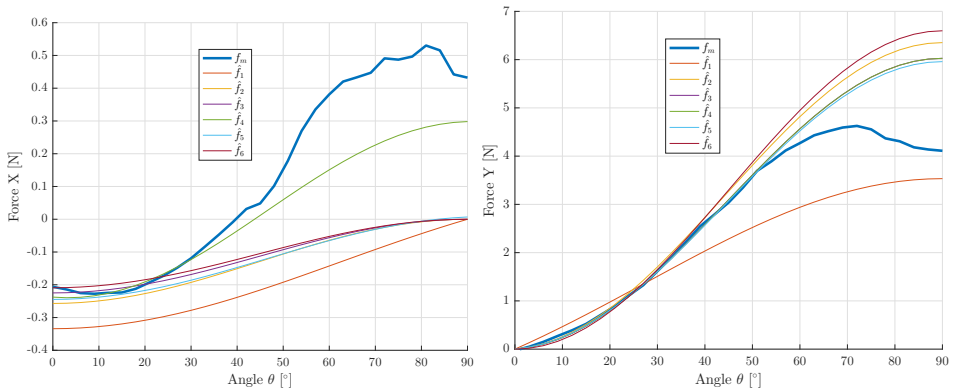

(a) Estimations based on $\theta \leq 39$ (b) Estimations based on $\theta \leq 39$

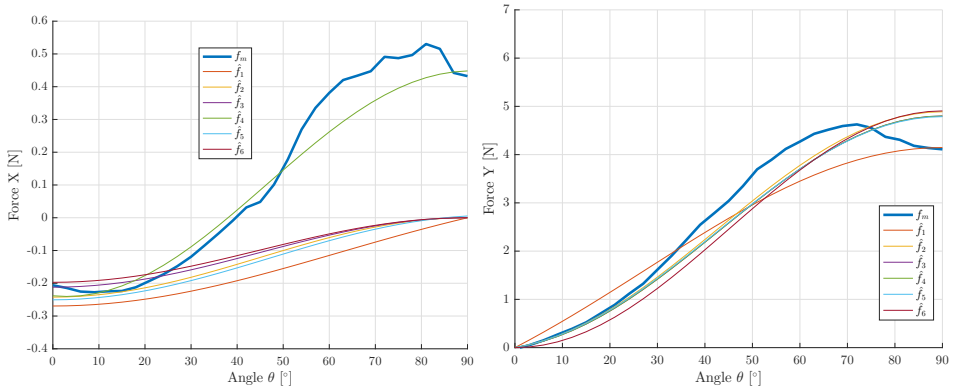

(c) Estimations based on $\theta \leq 90$ (d) Estimations based on $\theta \leq 90$

Figure 5.21: Comparison of system identifications based on the complete data set and data set limited to $\theta \leq 39$ degrees. For H2LT configuration at $v = 0.4$.

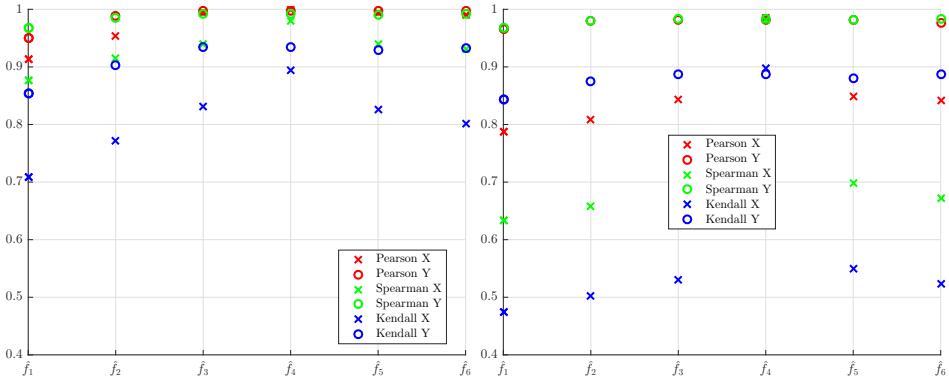

(a) Statistical analysis based on data set for $\theta \leq$ 39 degrees.

(b) Statistical analysis based on full data set.

Figure 5.22: Statistical analysis of estimation from experiment 2 based on limited data set(a) and full data set(b)

5.1.4 Comparison of simulation and experimental results for drag coefficients

The large set of data gathered from the simulations and the two experimental approaches results in different identified drag coefficients. This section compares the results from the two experimental approaches and the simulations for the two snake module configurations H1LT and H2LT.

Zero Angle of Attack at Increasing Velocities

Figure 5.23 compares the forces in x direction for $\theta = 0$ degrees. The results are qualitatively very similar, differing mainly in amplitude. Considering first the two experiments, a substantial higher number of data points are obtained for the circulation tank compared to the passive towing rig experiment. Aside from this, the only difference is that the recorded forces from the circulation tank experiments are not as high as what is obtained from the passive towing rig experiment. This observation supports the claim that the first experiments did not reach a steady-state velocity. As such, added mass fluid forces are most likely the source of the measured forces being higher. Also, as seen in Figure 5.23, the error is small comparing the two experimental results.

The forces returned from the two experiments are approximately twice as large as what is obtained from the simulations. This could be explained in part by the coating and rod exit discussed in Chapter 5.1.2. However, it does not seem plausible that these factors alone results in forces of twice the magnitude as the simulations. Further investigation should be done in the future by adapting other simulation tools.

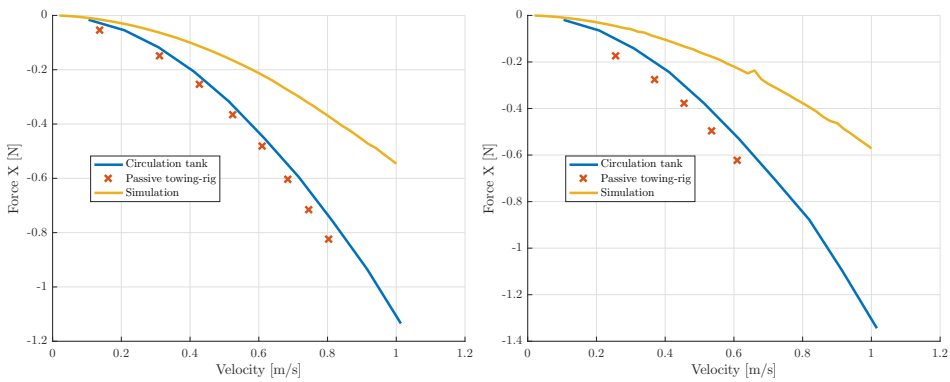

(a) (b)

Figure 5.23: Comparison of results from simulations and experiments. H1LT and H2LT snake module configurations at θ=0 degrees.

Varying Angle of Attack

Due to the inability to sufficiently control the velocity of system in the passive guided rail experiment, a direct comparison can not be made with the simulations and circulation tank experiment. However, it is reasonable to believe that the behaviour of the two experimental approaches are quite similar as this was shown to be the case for $\theta = 0$ degrees.

The comparisons of the obtained forces for both snake configurations, for varying θ at the four velocities are seen in Figures 5.24 and 5.25. The forces obtained from the circulation tank experiment are again larger in magnitude compared to the simulations. While the results are mostly qualitatively similar, the results partly disagree for large values of θ.

In x direction, there seems to be a general agreement on $\theta \approx 40 - 50$ degrees being the angle of attack where the body y velocity contributions to body x forces overcome the drag forces in body x and results in a total force in the opposite direction of the global drag forces. While the x forces from the simulations are increasing from $\theta = 0$ degrees and larger, the experiments show that the drag to be dominant up to $\theta \approx 10 - 30$ degrees, depending on the flow velocity. In the simulations, the x forces decrease at $\theta \approx 70$ degrees, while this does not happen until $\theta \approx 85$ degrees for the experiments. The exception is for H1LT at $v = 0.1$ m/s, where the decrease starts earlier at $\theta \approx 65$ degrees.

For y direction, the behaviour is more similar, differing mainly in the decrease in the forces obtained from the experiment after $\theta \approx 60 - 70$ degrees. As has been noted earlier, this decrease is probably caused by the nose and tail of the snake modules being fairly close to the walls at large θ. This could indicate that the qualitative behaviour of the simulations are correct, but the forces should be of the same magnitude as what was obtained by the experiments.

For both experimental approaches, the rod connecting the snake configuration to the remaining part of the experimental rig, causes a turbulent behaviour that increases the drag forces. This turbulent effect is clearly seen above the snake configuration in Figure 5.26, where a fluorescent liquid is added to the test section of the circulation tank, illuminated by ultra violet light. In the figure, the angle of attack is $\theta = 90$ degrees. In addition to the turbulence caused by the rod, the majority of the turbulence is caused by the fluid passing the main body of the snake configuration.

The relative impact of the rod will decrease for larger snake module configurations. Therefore, experiments on larger snake module configurations should be conducted in the future.

System Identification

In general, for both the simulations and experiments, $\hat{\mathbf{f}}_\mathbf{4}$ is the most fitting candidate. This may come of no surprise as this model variant is the most complex, involving the largest set of individual drag coefficients. Whereas the original model, $\hat{\mathbf{f}}_\mathbf{1}$ does in general not produce satisfying results. Though, this is the simplest model with only two drag coefficients. As $\hat{\mathbf{f}}_\mathbf{2}$ includes individual drag coefficients for linear and quadratic drag, it is generally more accurate compared to $\hat{\mathbf{f}}_\mathbf{1}$.

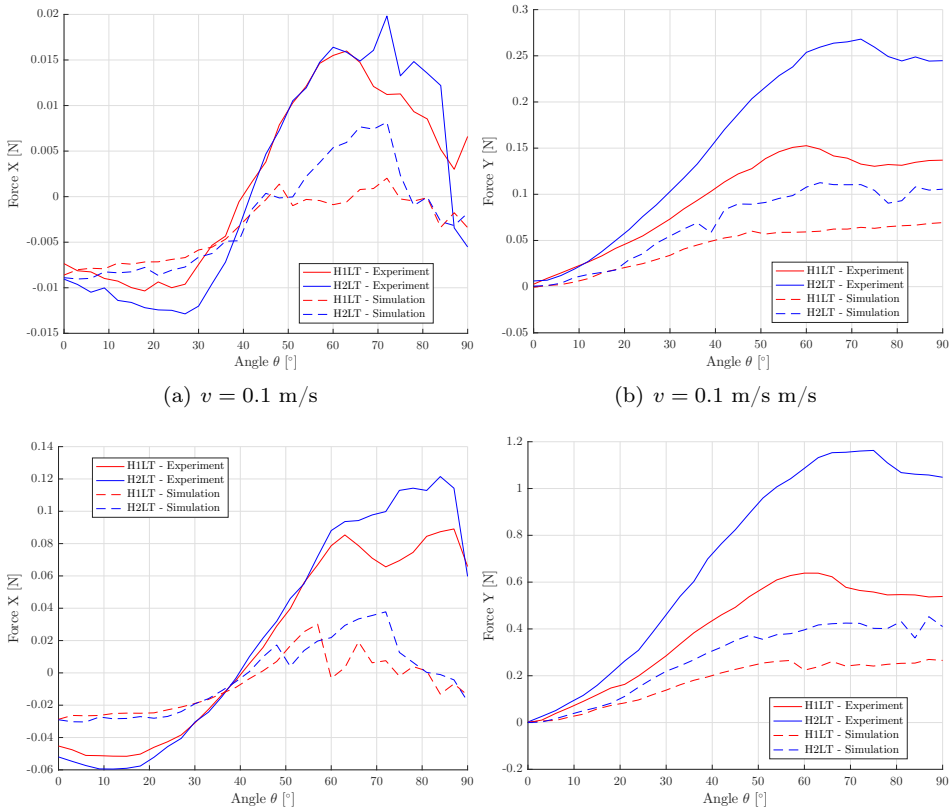

(a) $v = 0.1$ m/s

(b) $v = 0.1$ m/s m/s

(c) $v = 0.2$ m/s

(d) $v = 0.2$ m/s

Figure 5.24: Comparison of results from simulations and experiments. H1LT and H2LT snake module configurations at varying θ.

All estimation models struggle to handle the drop in x forces at a large θ. A possible solution is to have drag force equations of a higher polynomial degree. However, as the drag forces in x direction for a slender body is small compared to that in y direction, a more complex system may not be necessary. The higher accuracy of the model may not be significantly more beneficial than a simpler model of less accuracy. Additionally, from a practical point of view, most common gait patterns does not involve a value of θ larger than 40-50 degrees, suggesting the accuracy for large θ to be of low importance.

An interesting observation is that the accuracy of $\hat{\mathbf{f}}_\mathbf{1}$ and $\hat{\mathbf{f}}_\mathbf{2}$ increases for larger snake module configurations. This is clearly visible for the simulation results in Figure 5.7. The experimental results are also in agreement with this statement, although they are limited in size to H2LT. This implicates that, for large snake module configurations, the original drag force model $\hat{\mathbf{f}}_\mathbf{1}$ may be of similar accuracy as the more complex models. Where the relative drag forces caused by the head and tail gradually decreases with an increasing number of links. An important

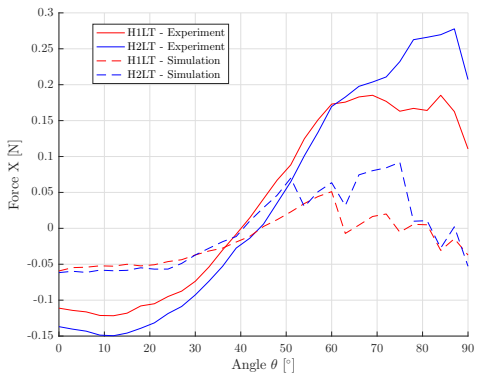

(a) $v = 0.3$ m/s

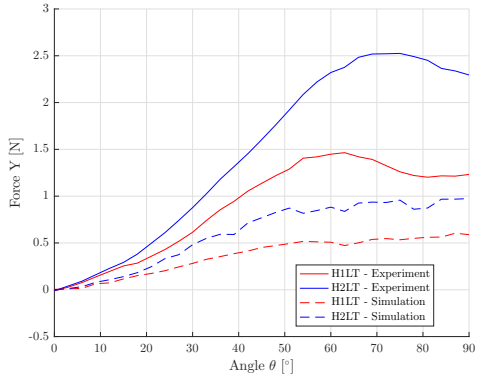

(b) $v = 0.3$ m/s

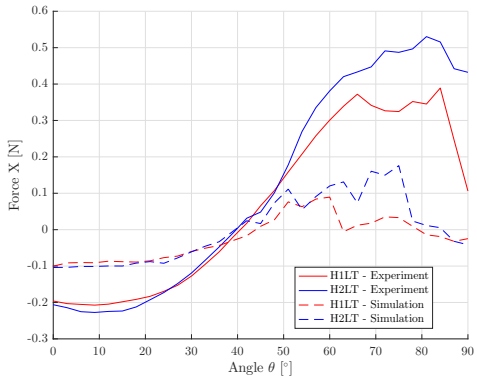

(c) $v = 0.4$ m/s

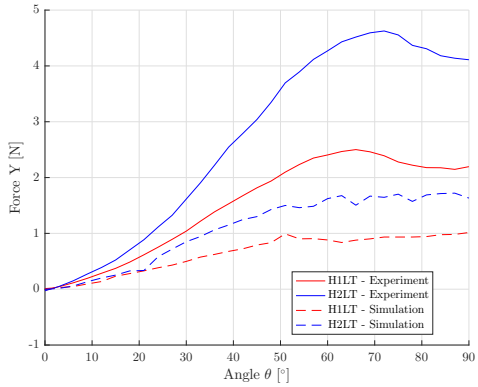

(d) $v = 0.4$ m/s

Figure 5.25: Comparison of results from simulations and experiments. H1LT and H2LT snake module configurations at varying θ.

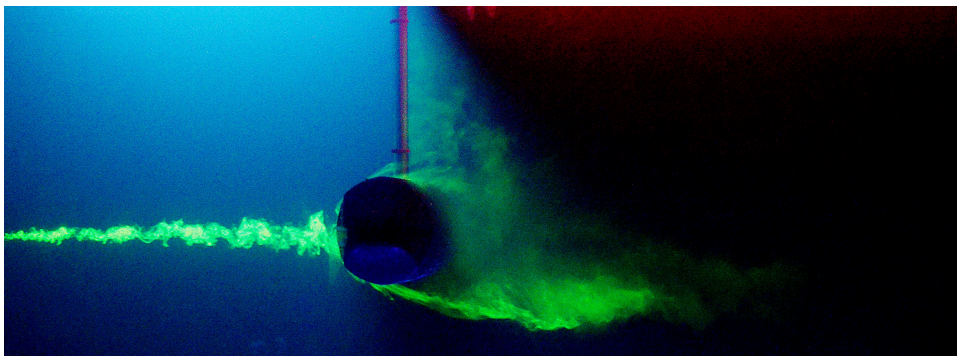

Figure 5.26: Flow patterns for the H2LT configuration at $\theta = 90$ degrees.

practical aspect to consider is the number of links required in order to obtain a thrust-producing gait pattern, which usually is $n \geq 8$. This further underlines the need for experiments conducted on larger snake module configurations.

Drag Coefficients

This section summarizes the obtained drag coefficients for model $\hat{\mathbf{f}}_\mathbf{4}$ based on the data gathered from the simulations and experiments. Additionally, coefficients for $\hat{\mathbf{f}}_\mathbf{1}$ is presented as well as this model may be very well suited for larger snake module configurations for $\theta < 50$ degrees.

Considering first the results for $\hat{\mathbf{f}}_\mathbf{4}$ in Table 5.7, it is clear that the coefficients for quadratic drag dominate the coefficients for linear drag. This might indicate that $\hat{\mathbf{f}}_\mathbf{4}$ could be simplified by removing some of the linear terms.

The resulting drag coefficients for $\hat{\mathbf{f}}_\mathbf{1}$ is presented in Table 5.8. Comparing these results to the analytical estimates in Table 2.2, the experimental results for C_f are closer to the analytical estimates than what was identified based on the simulations. On the other hand, the values for C_d are much smaller for both experiments and simulations compared to Table 2.2.

It should be possible to claim that for small snake module configurations, the effects from the head and tail modules, as well as the x-y cross forces have a significant presence compared to the effects caused by the link modules alone. And as result, it is necessary for a complex drag force model with several drag individual drag coefficients to be incorporated to sufficiently describe the resulting fluid forces. However, for larger snake module configurations, which is necessary

		Passive	**Circulation Tank**	
	Simulated	**Towing Rig**	Unrestricted	Restricted
C_f^I	0	0.0152	0	0
C_f^{II}	0.0191	0	0.0569	0
C_d^I	0.0066	0.0045	0.0126	0.0133
C_d^{II}	0.4064	1.5249	1.2402	1.4272
$C_{f_{HT}}^I$	0.0063	0	0.0141	0.0148
$C_{d_{HT}}^I$	0.1956	0.0795	0.1929	0.1769
$C_{f_{HT}}^{II}$	0.1050	0.2498	0.2531	0.2451
$C_{d_{HT}}^{II}$	0	1.8852	1.4444	1.1770
C_{XY}^I	0.0055	0.0870	0.0412	0.0351
C_{XY}^{II}	0.1957	0.8704	0.6654	0.4612

Table 5.7: Comparison of drag coefficients for force model, $\hat{\mathbf{f}}_\mathbf{4}$.

		Passive	**Circulation Tank**	
	Simulated	**Towing Rig**	Unrestricted	Restricted
C_f	0.0046	0.0242	0.0167	0.0207
C_d	0.1206	0.2813	0.3835	0.3628

Table 5.8: Comparison of drag coefficients for the original force model, $\hat{\mathbf{f}}_\mathbf{1}$.

to create thrust, a more simple model is sufficient as it was indicated from the simulation studies with larger configurations.

5.2 Added Mass

In this section the results for estimating the added mass coefficients are presented. Figure 5.27 overviews the procedures for the simulation and the experimental approach.

5.2.1 WADAM Simulations

The simulation results from WADAM is summarized in Table 5.9 together with the volume of each configuration. The excel file containing the full added mass matrices is found in Appendix A.1.1. In addition, the HydroD/WADAM project files together with the full .LIS output files are found in Appendix A.1.3.

Configuration	**Non-dimensionless**		**Dimensionless**		**Volume**
i	$\mu_{x,i}$	$\mu_{y,i}$	$C_{A_{x,i}}$	$C_{A_{y,i}}$	$V_i\,[m^3] \times 10^{-3}$
Head	0.2943	0.2366	0.7631	0.6134	0.376
Link	0.5421	1.2050	0.4170	0.9269	1.268
Tail	0.2683	0.1567	1.0456	0.6108	0.250
HT	0.1837	0.4911	0.2850	0.7620	0.629
H1LT	0.2318	1.8600	0.1195	0.9588	1.893
H2LT	0.5153	3.6840	0.1880	1.3500	2.670
H3LT	0.6486	5.1539	0.1653	1.3132	3.830
H4LT	0.6967	6.7942	0.1379	1.3448	4.929
H5LT	0.9147	8.3451	0.1480	1.3504	6.029
H6LT	0.8570	9.9436	0.1173	1.3606	7.130
H7LT	0.9210	11.527	0.1092	1.3664	8.230
H8LT	1.0449	13.112	0.1093	1.3711	9.330
H9LT	1.1822	14.689	0.1106	1.3740	10.430

Table 5.9: Simulation results for added mass on the different snake modules and configurations.

The simulations returns the added mass for each of the snake module configurations. The non-dimensionless added mass parameters in x and y direction for

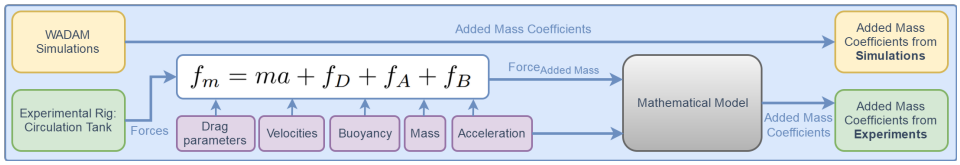

Figure 5.27: Illustration of the work flow for estimation of added mass coefficients.

configuration i, $\mu_{x,i}$ and $\mu_{y,i}$, are the total added mass [kg]. While the dimensionless $C_{A_{y,i}}$ and $C_{A_{x,i}}$ are commonly referred to as the added mass coefficients, and are dependent on the geometry of the object. They are related as shown in Equations 5.1 and 5.2.

$$\mu_{x,i} = V_i \rho C_{A_{x,i}}, \tag{5.1}$$

$$\mu_{y,i} = V_i \rho C_{A_{y,i}}. \tag{5.2}$$

Non-dimensionless added mass, $\mu_{x,i}$ and $\mu_{y,i}$, are shown graphically in Figure 5.28(a). It is seen that $\mu_{y,i}$ grows linearly for each added link, while $\mu_{x,i}$ barely increases compared to $\mu_{y,i}$, and is negligible for larger configurations of HnLT. Figure 5.28(b) show the dimensionless coefficients based on Equation 5.1 and 5.2. In addition, the coefficient for the added mass model presented in Equation 2.8 is shown, based on the calculation of Equation 5.3.

$$\mu_{y,i} = \mu_n \rho n \hat{C}_{A_i}. \tag{5.3}$$

The difference between both dimensionless added mass coefficients, $C_{A_{x,i}}$ and $C_{A_{y,i}}$, are roughly constant for configurations with $n \geq 3$ links. The original mathematical model disregards added mass in x direction, $C_{A_x} = 0$, as the impact is negligible compared to added mass in y direction for configurations with many link modules. The simulation results agrees with this. The coefficient based on the model presented in Equation 2.8, $\hat{C}_{A_i}$ follows the same trend, and settles on a value somewhat lower than the results from the simulations.

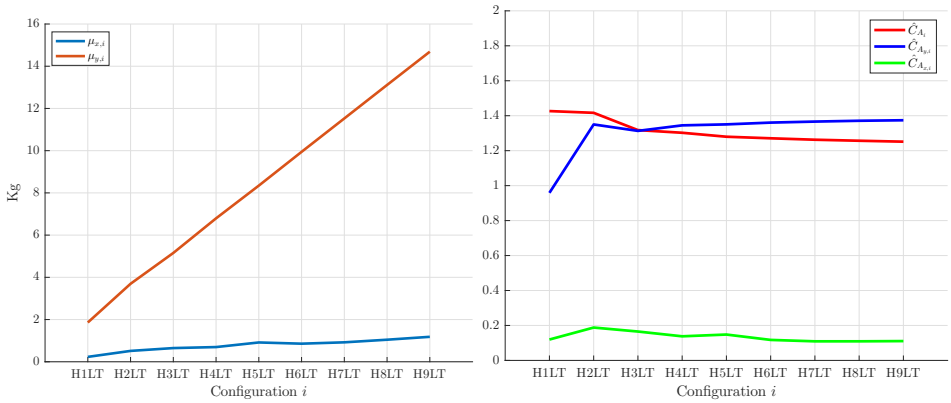

(a) Non-dimensionless added mass for all snake configurations.

(b) Dimensionless added mass coefficient based on the model and directly from simulations

Figure 5.28: Simulation results for added mass.

$\mathbf{C_{A_x}}$	$\mathbf{C_{A_y}}$	$\mathbf{C_A}$
0.1194	1.3601	1.2674

Table 5.10: Added mass coefficients from simulation.

System Identification

To obtain an estimated coefficient valid for every snake module configuration, a least square estimation is used on Equation 5.4 and 5.5

$$\mu_{x,i} = V_i \rho \hat{C}_{A_x}, \tag{5.4}$$

$$\mu_{y,i} = V_i \rho \hat{C}_{A_y}, \tag{5.5}$$

where $\hat{C}_{A_x}$ and $\hat{C}_{A_y}$ are the unknown coefficients. Similarly, an estimate of the coefficient using the model in Equation 2.8 is found from

$$\mu_{y,i} = \mu_n \rho n \hat{C}_A. \tag{5.6}$$

The resulting least square estimations returns the results shown in Table 5.10. The coefficient C_A is somewhat lower than C_{A_y}, where the same trend is seen in Figure 5.28(b). The difference is small, < 0.1, and smaller than the coefficient in x direction, which is already neglected in the model presented in Chapter 2.2.

5.2.2 Circulation Tank Experiment

The conducted experiments have considered added mass in y direction only. As both theory and the simulation results in Figure 5.28(a) agree on the added mass in x direction being insignificant [18], [38], this should be a reasonable choice. The results from the experiment relies on the experimentally obtained fluid drag coefficients. Figure 5.29 show the results of the experiment for different amplitudes, α, for a frequency, $\omega = 70$ deg/s. The behaviour is similar regardless of amplitude, and the magnitude of the measurement is larger for higher α, which is to be expected. Comparing H1LT in Figure 5.29(a) and H2LT in Figure 5.29(b), they both exhibit similar behaviour. For H2LT, the added mass is larger, due to H2LT being larger in both volume and mass.

System Identification

For the estimation, two different drag models estimates based on the drag experiments are used. This is done as a means to investigate how different drag force estimates influence the added mass estimations. The drag force models in question are $\hat{\mathbf{f}}_1$ and $\hat{\mathbf{f}}_4$. The least square estimation uses the following equation

$$f_A = \mu_n \rho n \hat{C}_A, \tag{5.7}$$

where f_A is the added mass force, and $\hat{C}_A$ is the unknown added mass coefficient. The result of the estimations is presented in Table 5.11, where it is clear that the resulting coefficients varies insignificantly based on which drag force model is

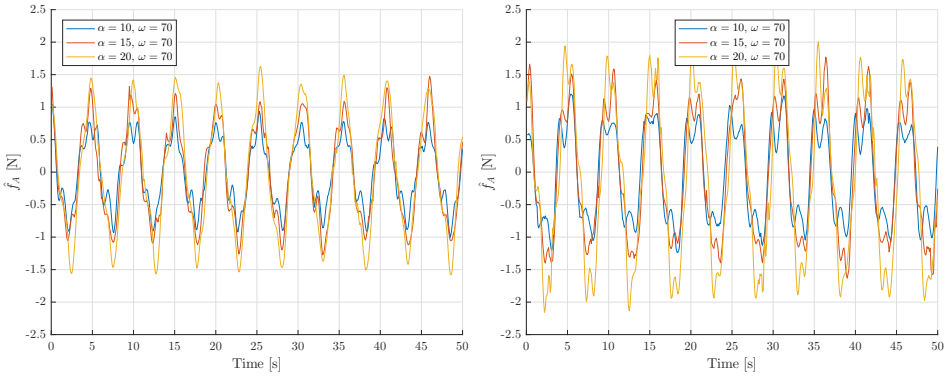

(a) H1LT (b) H2LT

Figure 5.29: Comparison of experimental results for added mass with varying α and $\omega = 70$.

Drag model	C_A
$\hat{\mathbf{f}}_1$	1.2754
$\hat{\mathbf{f}}_4$	1.2770

Table 5.11: Added mass coefficients from circulation tank experiments, based on different drag force models.

used. The obtained values are close to the theoretical value which is assumed to be $C_A \approx$ 1-1.5. As $\hat{\mathbf{f}}_4$ was shown to be the most precise drag force model, this is used as a basis for the added mass estimations.

In Figures 5.30, 5.31, and 5.32, the estimated added mass forces is compared to the measured for different configurations and values of α and ω. Similar to the estimations of drag forces, the added mass force estimations are more precise for H2LT snake configuration. Again, this might indicate the modelling to be more suited for larger snake module configurations. The estimated model does not account for the head and tail. For the H1LT configuration, the head and tail accounts for 33% of the total volume, while only 19% and 5% for H2LT and H9LT, respectively. As the head-tail contribution decreases rapidly with each addition link, the reduced correlation of experimental and estimated added mass for H1LT compared to H2LT can be attributed to this .

Sources of Error

To the best of our knowledge, the simulation results are fairly accurate. However, the obtained experimental results may be influenced by several factors.

- The snake configuration is not neutrally buoyant, as is assumed for the mathematical model. Though this has been accounted for in the performed calculations, the buoyancy may not be constant as air bubbles escape from the

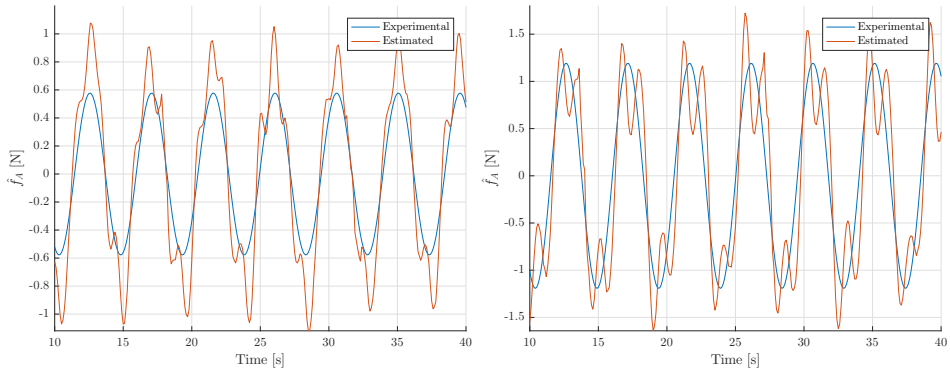

(a) H1LT (b) H2LT

Figure 5.30: Comparison of experimental results and estimation for added mass with $\alpha = 10$ and $\omega = 80$.

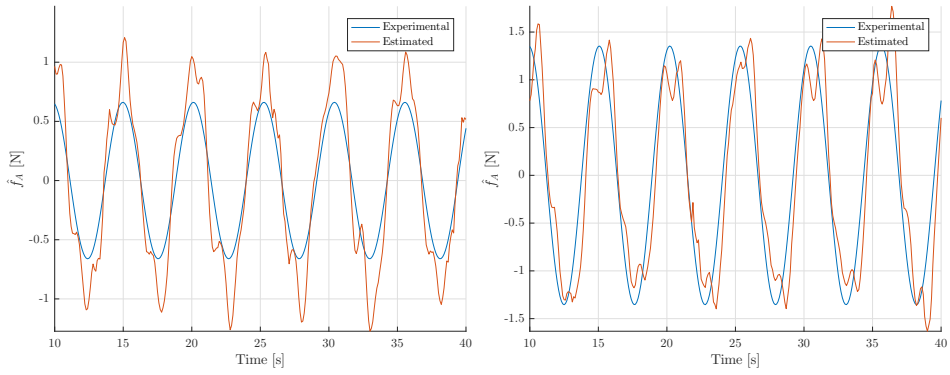

(a) H1LT (b) H2LT

Figure 5.31: Comparison of experimental results and estimation for added mass with $\alpha = 15$ and $\omega = 70$.

configuration and is replaced by water. This also affects the mass of the snake module configuration.

- The sinusoidal motion may not be perfectly smooth at all times, although this effect is not visible by visual inspection. As the estimated acceleration from Chapter 4.4.5 is sinusoidal, any discrepancy between the estimated and real acceleration will produce an error in from of inaccurate force measurements. The acceleration estimation method proposed in Chapter 4.4.5 should ideally be validated by measurements from an accelerometer.
- The fluid flow in the circulation tank that removes the water between the snake configuration and the walls might be too slow, possibly causing some torque around the body z axis and incorrect forces in body y direction.

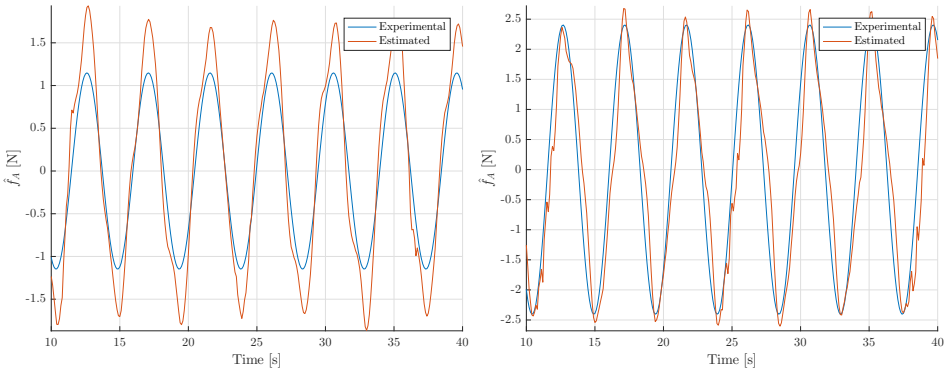

(a) H1LT (b) H2LT

Figure 5.32: Comparison of experimental results and estimation for added mass with $\alpha = 20$ and $\omega = 80$.

- The results are directly dependent on the identified drag coefficients. Any error in the drag coefficient for $\theta = 90$ degrees will propagate to the added mass results.
- Ideally, the experiment should be conducted for even more snake module configurations to eliminate possible effects from the rod connecting the snake to the servo motor.

As for the drag experiments, each of the above factors may not significantly alter the results alone, but the combination of several of these might cause an error.

5.2.3 Comparison of simulation and experimental results for added mass coefficients

Table 5.12 overviews the added mass coefficients identified based on the performed simulations and experiments. From the simulation, the added mass coefficient in x direction has an expected low value and a theoretical value of the added mass parameter $\mu_t = 0$ is reasonable for modelling purposes, especially for large snake module configurations. Comparing the simulation and experimental results, the resulting added mass coefficients are of similar values. This indicates the simulation results can be used to properly identify the added mass coefficients. Further, Figure 5.33 compares the measured added mass force from the circulation tank experiments to the different obtained coefficients. As have been mentioned, the estimates for H2LT performs better, but as the variation between the added mass coefficient estimates are low, the resulting added mass forces are similar.

The obtained fluid parameters in Table 5.12 are within the range of the analytical estimates in Table 2.2

	Simulations	Circulation Tank
C_{A_x}	0.1194	-
C_{A_y}	1.3601	-
C_A	1.2674	1.2770

Table 5.12: Comparison of added mass coefficients obtained from simulations and experiments.

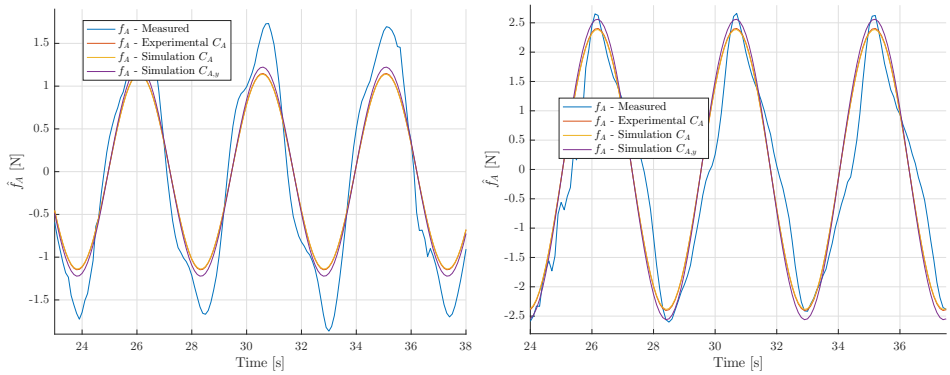

(a) H1LT (b) H2LT

Figure 5.33: Comparison of estimated added mass, based on the different approaches, for H1LT and H2LT with $\alpha = 20$ and $\omega = 80$.

Chapter 6

Conclusions and Future Work

6.1 Conclusions

This thesis has presented methods for identifying fluid coefficients for a general underwater snake robot by experiments and CFD simulations. With these methods, the fluid force model presented in [23] have used to identify the parameters for the hydrodynamic model. Additionally, different variations and extensions to the model have been presented to account for hydrodynamic behaviour observed in the experiments.

The drag force simulations has given a qualitative insight into the fluid forces, but do not compare in magnitude to the experimental results. The two experiments related to the drag coefficients have correlating results, and when the angle of attack is limited to $\theta \leq 40°$, the proposed drag force model variations show promising results. It has been observed that the original drag force model in [23] correlates to the results obtained in this thesis for large snake module configurations, indicating that the closed-form analytical model of underwater snake robots is suitable for snake module configurations with many links. It was found that for large angles of attack, the resulting hydrodynamic behaviour requires a more complex drag force model capable of capturing these effects. Based on the different experimental results, the drag force coefficients for the model presented in [23] have been identified as $C_f \in [0.02, 0.03]$ which is in accordance with the theoretical estimates, and $C_d \in [0.2, 0.4]$ which is smaller than the expected theoretical values.

This thesis has shown that the added mass coefficient for the underwater snake robot Mamba is $C_A \approx 1.27$, which is in agreement with the existing analytical estimates for a general underwater snake robot. Additionally, the added mass effects caused by the head and tail modules can be disregarded for larger snake module configurations.

6.2 Recommendations for Future Work

The experiments and simulation schemes presented in this thesis can be adapted for fluid coefficient identification for a 3D model of underwater snake robots. The proposed results in this thesis should be verified by adapting the described experi-

mental procedures to larger snake module configurations, with respect to the drag coefficients. The use of an accelerometer in the experiment related to added mass coefficients is recommended in order to obtain more accurate estimates of the added mass coefficients. Additional simulations could be conducted using alternate software platforms such as ANSYS Fluent or COMSOL to verify the fluid coefficients obtained in this thesis. Finally, it would be of interest to employ the identified coefficients in experiments on the underwater snake robot Mamba to investigate possible improvements in performance.

Appendices

Appendix A

Simulations

A.1 Added Mass Coefficients

A.1.1 Results

The excel sheet containing the added mass results is found in the folder:
`Appendices/Appendix A-Sim/A.1-Added Mass/A.1.1-Results`

A.1.2 WADAM Guide

A brief tutorial for calculating the added mass using HydroD (WADAM) is found in the folder:
`Appendices/Appendix A-Sim/A.1-Added Mass/A.1.2-WADAMGuide`

A.1.3 Input Geometry

The following geometry files and relevant software projects are found in the folder:
`Appendices/Appendix A-Sim/A.1-Added Mass/A.1.3-Geometry`

- Solidworks geometry files
- Solidworks geometry files exported to .step-files for Rhinoceros
- Rhinoceros projects
- Rhinoceros geometry files exported to .gdf-files for HydroD (WADAM)
- HydroD (WADAM) project files

A.2 Drag Coefficients

A.2.1 Results

The excel sheets containing the Solidworks simulation results is found in the folder:
`Appendices/Appendix A-Sim/A.2-Drag Coefficients/A.2.1-Results`

A.2.2 Solidworks Guide

A brief tutorial for setting up a Solidworks Flow Simulation is found in the folder:
`Appendices/Appendix A-Sim/A.2.2-Drag Coefficients/A.2.2-SWGuide`

A.2.3 Geometry

The following geometry files are found in the folder:
`Appendices/Appendix A-Sim/A.2-Drag Coefficients/A.2.3-Geometry`

- Geometry files for simulations
- Solidworks geometry assemblies for the different configurations

Appendix B

Experiments

B.1 Added Mass Coefficients

B.1.1 Added Mass Coefficients Results

The experimental added mass results are found in the folder:
`Appendices/Appendix B-Exp/B.1-Added Mass/B.1.1-AddedMassResults`

B.1.2 LabView Program

The LabView program used for the added mass experiments is found in the folder:
`Appendices/Appendix B-Exp/B.1-Added Mass/B.1.2-LabView`

B.1.3 LabView Program Guide

A brief guide to the LabView program is found in the folder:
`Appendices/Appendix B-Exp/B.1-Added Mass/B.1.3-LabViewGuide`

B.2 Drag Coefficients

B.2.1 Passive Guided Rail Towing Rig Results

The excel sheets containing the experimental results are found in the folder:
`Appendices/Appendix B-Exp/B.2-Drag/B.2.1-GuidedRailResults`

B.2.2 Circulation Tank Results

The excel sheets containing the experimental results is found in the folder:
`Appendices/Appendix B-Exp/B.2-Drag/B.2.2-CircTankResults`

Appendix C

Sensor

The email to the suppliers and the received quotes are found in the folder:
`Appendices/Appendix C-Sensor`

Appendix D

MATLAB

The MATLAB codes used for extracting, processing and plotting the data are found in the folder:
`Appendices/Appendix D-MATLAB`

References

[1] ANSYSfluent. Ansys fluent webpage, 2016. URL http://www.ansys.com/Products/Fluids/ANSYS-Fluent.

[2] A. I. Automation. *Six-Axis Force/Torque Sensor System - Installation and Operation Manual*, Sept. 2015. URL http://www.ati-ia.com/app_content/documents/9620-05-DAQ.pdf.

[3] A. I. Automation. F/t sensor: Mini40 ip65/ip68, Mar. 2017. URL http://www.ati-ia.com/products/ft/ft_models.aspx?id=Mini40+IP65%2fIP68.

[4] A. Crespi, A. Badertscher, A. Guignard, and A. J. Ijspeert. Amphibot i: an amphibious snake-like robot. *Robotics and Autonomous Systems*, 50(4):163–175, 2005. ISSN 0921-8890.

[5] DNV. Sesam user manual - wadam, 2010. URL https://projects.dnvgl.com/sesam/manuals/Wadam_UM.pdf.

[6] DNV. *Modelling and Analysis of Marine Operations*. Det Norske Veritas AS, 2014. URL http://rules.dnvgl.com/docs/pdf/DNV/codes/docs/2014-02/RP-H103.pdf. Recommended practice DNV-RP-H103.

[7] DNV. Wadam webpage, 2016. URL https://www.dnvgl.com/services/frequency-domain-hydrodynamic-analysis-of-stationary-vessels-wadam-2412.

[8] R. Doraiswami, C. Diduch, and M. Stevenson. *Linear Least Squares Estimation*. Chichester, UK: John Wiley & Sons, Ltd, Chichester, UK, 2014.

[9] O. A. Eidsvik and I. Schjølberg. Identification of hydrodynamic parameters for remotely operated vehicles. Master's thesis, NTNU, 2015.

[10] Y. Eng, W. Lau, E. Low, G. Seet, and C. Chin. Estimation of the hydrodynamics coefficients of an rov using free decay pendulum motion. *Engineering Letters*, 16(3):326–331, 2008. ISSN 1816-093X.

[11] O. M. Faltinsen. *Sea loads on ships and offshore structures*. Cambridge ocean technology series. Cambridge University Press, Cambridge, 1990.

[12] T. I. Fossen. *Handbook of Marine Craft Hydrodynamics and Motion Control*. Wiley, New York, 2011.

[13] Z. Guan, N. Gu, W. Gao, and S. Nahavandi. 3D hydrodynamic analysis of a biomimetic robot fish. In *Proc. 11th Int Control Automation Robotics Vision (ICARCV) Conf*, pages 793–798, Dec. 2010. doi: 10.1109/ICARCV.2010.5707359.

[14] J. Hauke and T. Kossowski. Comparison of values of pearson's and spearman's correlation coefficients on the same sets of data. *Quaestiones Geographicae*, 30(2):87–93, 2011. ISSN 0137477X.

[15] S. Hirose. *Biologically Inspired Robots: Snake-Like Locomotors and Manipulators*. Oxford University Press, 1993.

[16] E. Huse and N. tekniske høgskole Institutt for marin hydrodynamikk. *Experimental methods in marine hydrodynamics*, volume UK-94-48 of *Kompendium (Norges tekniske høgskole. Fakultet for marin teknikk)*. Marinteknisk senter, Institutt for marin hydrodynamikk, Trondheim, 1994.

[17] C. E. Jordan. Coupling internal and external mechanics to predict swimming behavior: a general approach. *American Zoologist*, 36(6):710–722, 1996. ISSN 00031569.

[18] E. Kelasidi, K. Y. Pettersen, J. T. Gravdahl, and P. Liljeback. Modeling of underwater snake robots. In *Proc. IEEE Int. Conf. Robotics and Automation (ICRA)*, pages 4540–4547, May 2014. doi: 10.1109/ICRA.2014.6907522.

[19] E. Kelasidi, P. l. Liljeback, K. Pettersen, J. Gravdahl, and E. Kelasidi. Experimental investigation of efficient locomotion of underwater snake robots for lateral undulation and eel-like motion patterns. *Robotics and Biomimetics*, 2 (1):1–27, 2015.

[20] E. Kelasidi, K. Y. Pettersen, and J. T. Gravdahl. Energy efficiency of underwater snake robot locomotion. 2015. ISSN 1934-1776.

[21] E. Kelasidi, N. teknisk-naturvitenskapelige universitet, and N. teknisk-naturvitenskapelige universitet Institutt for teknisk kybernetikk. *Modeling, control and energy efficiency of underwater snake robots*. PhD thesis, Norwegian University of Science and Technology, Faculty of Information Technology, Mathematics and Electrical Engineering, Department of Engineering Cybernetics, Trondheim, 2015.

[22] E. Kelasidi, P. Liljeback, K. Y. Pettersen, and J. T. Gravdahl. Innovation in underwater robots: Biologically inspired swimming snake robots. *IEEE Robotics Automation Magazine*, 23(1):44–62, Mar. 2016. ISSN 1070-9932. doi: 10.1109/MRA.2015.2506121.

[23] E. Kelasidi, K. Y. Pettersen, J. T. Gravdahl, S. Strømsøyen, and A. Sørensen. Modeling and propulsion methods of underwater snake robots. *Proc. 1st IEEE Conference on Control Techonology and Applications, Kohala Coast, Hawaii 2017*, 2017 (Accepted).

[24] M. G. Kendall and J. D. Gibbons. *Rank correlation methods*. Edward Arnold, London, 1990.

[25] S. Kern and P. Koumoutsakos. Simulations of optimized anguilliform swimming.(author abstract). *Journal of Experimental Biology*, 209(24):4841, 2006. ISSN 0022-0949.

[26] W. Khalil, G. Gallot, and F. Boyer. Dynamic modeling and simulation of a 3-d serial eel-like robot. *Systems, Man, and Cybernetics, Part C: Applications and Reviews, IEEE Transactions on*, 37(6):1259–1268, 2007. ISSN 1094-6977.

[27] S. Kjemperud and I. F. M. T. Norges Teknisk-Naturvitenskapelige Universitet, Fakultet For Ingeniørvitenskap Og Teknologi. Hydrodynamic coefficients for wellhead structures, 2012.

[28] S. Lee, J. Park, and C. Han. Optimal control of a mackerel-mimicking robot for energy efficient trajectory tracking. *Journal of Bionic Engineering*, 4(4): 209–215, 2007. ISSN 1672-6529.

[29] P. F. Liagre and J. M. Niedzwecki. Estimating nonlinear coupled frequency-dependent parameters in offshore engineering. *Applied Ocean Research*, 25(1): 1–19, 2003. ISSN 0141-1187.

[30] M. J. Lighthill. Large-amplitude elongated-body theory of fish locomotion. *Proc Roy Soc London Ser B*, 1971.

[31] P. l. Liljeback, K. Y. Pettersen, O. y. Stavdahl, and J. T. Gravdahl. *Snake Robots: Modelling, Mechatronics, and Control*. Advances in Industrial Control. Springer London, London, London, 2013.

[32] P. l. Liljeback, O. y. Stavdahl, K. Y. Pettersen, and J. T. Gravdahl. *Mamba - A waterproof snake robot with tactile sensing*. IEEE, 2014.

[33] C. Lopez-Pavon and A. Souto-Iglesias. Hydrodynamic coefficients and pressure loads on heave plates for semi-submersible floating offshore wind turbines: A comparative analysis using large scale models. *Renewable Energy*, 81:864–881, 2015. ISSN 0960-1481.

[34] K. A. Melsaac and J. P. Ostrowski. A geometric approach to anguilliform locomotion: modelling of an underwater eel robot. *Robotics and Automation, 1999. Proceedings. 1999 IEEE International Conference on*, 4:2843–2848, 1999. ISSN 0-7803-5180-0.

[35] P. Millan, David; Thornburn. A planar motion mechanism (pmm) for ocean engineering studies. In *18th Newfoundland Electrical and Computer Engineering Conference, Canada*, 2010.

[36] J. R. Morison and L. A. B. California Univ Berkeley Wave Research. The force distribution exerted by surface waves on piles, 1953.

[37] A. T. Morrison and D. R. Yoerger. Determination of the hydrodynamic parameters of an underwater vehicle during small scale, nonuniform, 1-dimensional translation. *OCEANS '93. Engineering in Harmony with Ocean. Proceedings*, pages II277–II282, 1993. ISSN 0-7803-1385-2.

[38] J. N. Newman. *Marine hydrodynamics*. MIT Press, Cambridge, Mass, 1977.

[39] Q. S. Nguyen, S. Heo, H. C. Park, and D. Byun. Thrust improvement of an fish robot actuated by compressed unimorph piezoelectric composite actuator. In *Proc. IEEE Int Robotics and Biomimetics (ROBIO) Conf*, pages 1603–1608, Dec. 2009. doi: 10.1109/ROBIO.2009.5420392.

[40] OpenFOAM. Openfoam webpage, 2016. URL http://www.openfoam.com/.

[41] M. Porez, F. Boyer, and A. J. Ijspeert. Improved lighthill fish swimming model for bio-inspired robots: Modeling, computational aspects and experimental comparisons. *The International Journal of Robotics Research*, 33(10):1322–1341, 2014. ISSN 0278-3649.

[42] Rhinoceros. Rhinoceros webpage, 2017. URL https://www.rhino3d.com/.

[43] Sintef. Circulating water tunnel (cwt), 2016. URL http://www.sintef.no/en/all-laboratories/circulating-water-tunnel/.

[44] Smooth-On. Dragon skin 10 medium, Mar. 2017. URL https://www.smooth-on.com/products/dragon-skin-10-medium/.

[45] SolidWorks. Soildworks flow simulation, 2016. URL http://www.solidworks.com/sw/products/simulation/flow-simulation.htm.

[46] Solidworks. *Technical Reference Solidworks Flow Simulation 2016*, 2016.

[47] G. Taylor. Analysis of the swimming of long and narrow animals. *Proceedings of the Royal Society of London. Series A, Mathematical and Physical Sciences (1934-1990)*, 214(1117):158–183, 1952. ISSN 0080-4630.

[48] WAMIT. Wamit webpage, 2016. URL http://www.wamit.com/.

[49] A. J. Wiens and M. Nahon. Optimally efficient swimming in hyper-redundant mechanisms: control, design, and energy recovery. *Optimally efficient swimming in hyper-redundant mechanisms: control, design, and energy recovery*, 7 (4):046016, 2012. ISSN 1748-3182.

[50] A. Zhang, S. Ma, B. Li, M. Wang, X. Guo, and Y. Wang. Adaptive controller design for underwater snake robot with unmatched uncertainties. *Sci. China Inf. Sci.*, 59(5):1–15, 2016. ISSN 1674-733X.